Structure and dynamics in small biomolecular systems

Ivo Kalkman

Structure and dynamics in small biomolecular systems

Een wetenschappelijke proeve op het gebied van de
Natuurwetenschappen, Wiskunde en Informatica

Proefschrift

ter verkrijging van de graad van doctor
aan de Radboud Universiteit Nijmegen
op gezag van de rector magnificus prof. mr. S.C.J.J. Kortmann,
volgens besluit van het College van Decanen
in het openbaar te verdedigen op `vrijdag 20 februari 2009`
om `13.30` uur precies

door

Ivo Michel Kalkman

geboren op 3 september 1979
te Tiel

Aan mijn ouders

Contents

CHAPTER 1

Introduction

Until the beginning of the 19th century it was generally believed that biomolecules, the molecules that naturally occur in living organisms, could only be produced by nature. The synthesis of urea by Friedrich Wöhler in 1828 radically changed that idea, and his discovery can be seen as the birth of the field of biochemistry.[1] Biochemistry concerns itself with the study of all chemical processes in living organisms. Over time, more and more physical techniques were introduced to obtain accurate quantitative information, which eventually gave rise to the field of biophysics. Given the complexity of life the field is very large and diverse, and its impact on society has been enormous.

It has become clear that, although nature itself is widely varied, the set of building blocks it employs is in many cases surprisingly limited. For example, proteins perform essential functions in every organism and fulfill roles ranging from enzymatic activity and immune responses to providing structural rigidity and cell adhesion. At the moment, the protein data bank contains more than 50,000 different proteins and the number is still growing fast.[2] Despite this, almost all proteins are built using only 20 different amino acids.[3] Perhaps even more amazingly DNA, in which all genetic information for organisms is stored, is coded using only four different base pairs. Given this small number of elementary motifs it may be hoped that knowledge of their exact structure and relevant dynamical processes leads to a better understanding of the larger biologically interesting systems.

The research described in this thesis focusses on exactly this topic: the fundamental study of small molecules or molecular complexes that are either of biological relevance themselves or, more often, can be seen as model systems for some structural arrangement or molecular interaction. This is done by determining the structure of these systems as accurately as possible by means of rotationally resolved electronic spectroscopy.[4] From the exact structure a large amount of information can be extracted regarding the forces inside these systems, and dynamical processes can even show up directly in the measured spectra (see section 1.3.2). Detailed knowledge of the electronically excited state is especially useful since this information is hard to obtain with other experimental methods and, as a result, comparatively little is known about it. Since the measurements are done on isolated molecules in the gas phase, where

interactions with environmental factors are absent, this also means that these measurements can be used as benchmarks for *ab initio* calculations on the electronically excited state, which still poses a serious problem.

When compared with most other spectroscopic techniques, a great asset of rotationally resolved electronic spectroscopy is its extremely high resolution. Rotational constants can generally be determined to an accuracy of about 100 kHz, which for a typical electronic transition with a frequency of around 10^{15} Hz means a relative accuracy of $1 : 10^{10}$. Since electronic transitions are studied, not only the rotational constants of the ground state but also those of the electronically excited state result from the experiments. Additionally, it is possible to extract information on the direction of the transition dipole moment in the molecule (section 1.3.3), the excited state lifetime (provided it is in the range of roughly one to several tens of ns and the spectra are not too congested) and, obviously, the exact frequency of the electronic origin transition.

1.1   Motivation

The goal of fundamental research in general is to elucidate processes and properties that are not (well) known. With advances in quantum chemical methods and the ongoing increase in available computational power, *ab initio* calculations are nowadays able to describe the structures and properties of the electronic ground state of many molecules to an accuracy comparable to that of our experiments. In the size range of systems discussed in this thesis (15-30 atoms) the molecules that are harder to describe are those with flexible sidechains, where many different conformations are possible. An even greater problem is posed by weakly bonded molecular complexes, such as dimers, hydrogen bound water clusters and van der Waals bonded rare gas clusters. Furthermore, for practically all systems a description of the electronically excited state is troublesome: prediction of the transition dipole moment direction in a molecule or complex is very hard, and structures are generally less reliable.

Even if structures and properties of certain systems are well understood its dynamics may be hard to describe. The reason for this is that many dynamical processes are highly sensitive to the detailed electronic and geometric structure. Conversely, if dynamical processes are observable this means that very accurate information on the potential energy surface(s) of the state(s) involved in the process can be obtained.

If the experiments described here are to further the understanding of biologically relevant molecules then the systems that combine several of the areas described above are ideally suited for these experiments, and together with biological relevance this serves as a guideline for the selection of systems to be studied. Since the systems that will be described in this thesis were chosen with the above criteria in mind it should not come as a surprise that *ab initio* calculations in many cases have difficulties in providing an accurate description.

Chapter 2 describes the benzoic acid dimer, a highly symmetric doubly hydrogen bonded system. Multiply hydrogen bonded structures form the backbone of some of the most important biological molecules, like α-helices and β-sheets in proteins and base pairs in DNA, and because of its high symmetry the benzoic acid dimer is ideally suited for their investigation. A concerted tunneling motion of both hydrogen

atoms involved in hydrogen bonding will be observed and analysed, and from this the change of tunneling barrier height on electronic excitation will be determined. Chapter 3 details the clusters of phenol with one and two argon atoms. Phenol offers rare gas atoms two ways to bind to it: through a hydrogen bond with its hydroxy group or through a van der Waals bond with its π electron system, above the benzene ring. It will be shown that for both clusters the van der Waals bonded structure is favoured; in the case of the two argon cluster it chooses a symmetric arrangement with one argon atom on each side of the ring.

Chapter 4 will tackle *o*-toluidine, also known as *o*-methylaniline. It consists of a benzene ring with an aminogroup and a methyl group attached to it in neighbouring positions. The methyl group can rotate around its symmetry axis in both the ground and electronically excited state but the barrier to rotation is much lower in the excited state than in the ground state. Simultaneously, steric hindrance deforms the methyl rotor during its rotation, destroying its C_3 symmetry, and the amino group moves from an out-of-plane configuration into the plane of the benzene ring when the molecule is electronically excited. Evidence for a precessional motion of the methyl rotor axis resulting from these complex dynamics will be presented. In chapter 5 the one and two water clusters of 7-azaindole will be discussed. The 7-Azaindole dimer is a model system for tautomeric processes in DNA, and in order to gain more insight into its hydrogen bonding characteristics the monomer and its water clusters have also been investigated extensively. In the water clusters studied here a cyclic structure will be derived where the water molecule(s) bind to both the pyrrolo NH group and the pyridino N atom. Furthermore, a reversal of the L_a and L_b energy level ordering on cluster formation has been found and in the two water cluster a large amplitude motion involving the two out-of-plane hydrogen atoms will be derived.

Experiments on the phenol dimer are presented in chapter 6. The attractive force due to a hydrogen bond between both phenol moieties is countered by the dispersion interaction between the π electron clouds of both rings. The resulting structure is one where both moieties form an angle with respect to each other and the size of this angle serves as a sensitive probe of the delicate balance between both forces. It will be shown that the hydrogen bond becomes stronger on electronic excitation leading to a larger angle between both monomers. In chapter 7 the indole analogue benzimidazole will be discussed. Since indole is the chromophore of the amino acid tryptophan, which in turn accounts for most of the fluorescence in proteins, an exact knowledge of the excited state properties of its analogues is very important for the interpretation of protein fluorescence data. In the case of benzimidazole the angle of the transition dipole moment with the main inertial axis was determined to be -30°. Furthermore the excited state lifetime was found to vary with isotopic substitution.

1.2 The Experiment

The experimental setup that is used for the measurements described in this thesis basically consists of two parts: the molecular beam machine and the laser system.

1.2.1 Molecular Beam Machine

In order to measure spectra with rotational resolution they need to be relatively sparse. In our case, this is achieved by producing rotationally cold molecules in the molecular beam machine shown in figure 1.1, which consists of four differentially pumped vacuum chambers. The first chamber contains the source, which is a metal housing that can be heated up to 300 °C. Inside the housing is a removable quartz container which holds the molecule to be investigated in purified form and can be filled from the outside without breaking the vacuum. A buffer gas (usually argon) carries the gaseous sample molecules to the nozzle, where the two are supersonically co-expanded into the vacuum. Multiple many-body collisions take place in the nozzle which rotationally cool the sample molecules, resulting in an effective rotational temperature in the molecular beam of around 1-5 K. For the measurement of water clusters, the buffer gas is led through a cooled water reservoir before going to the sample chamber.
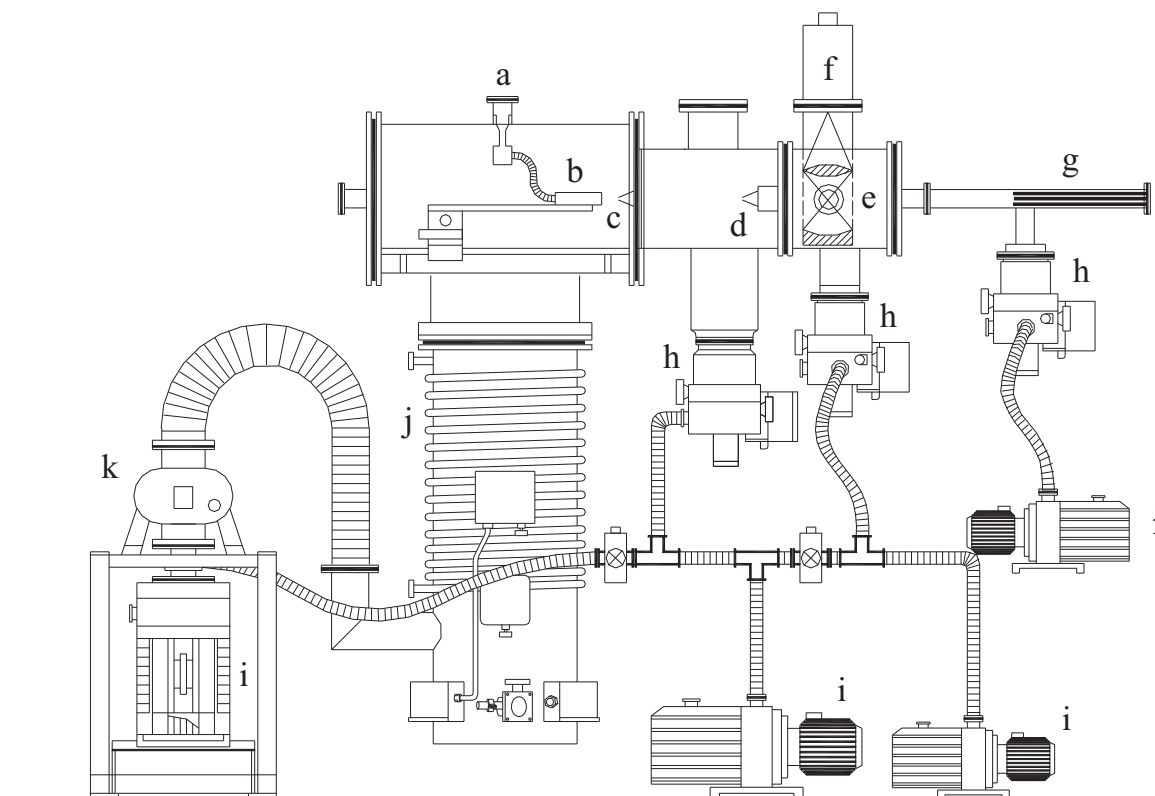
Figure 1.1: The molecular beam machine, consisting of (a) sample housing, (b) nozzle, (c) first skimmer, (d) second skimmer, (e) detection zone, (f) photomultiplier tube, (g) quadrupole spectrometer, (h) turbo pumps, (i) rotary pumps, (j) diffusion pump and (k) roots pump.

The pressure in the first vacuum chamber is always kept below 10^{-3} mbar. This is necessary in order to avoid a breakdown of the molecular beam due to collisions with background gas and is achieved by using a large diffusion pump with an 8000 l/s pump speed backed up by a roots pump and a rotary pump. Still, even at these pressures background gas collisions will occur relatively often and it is therefore necessary to minimize the distance the sample molecules travel through this chamber. For this reason a skimmer leading into the second vacuum chamber, the buffer chamber, is

located a few mm behind the nozzle exit. This skimmer is 1 mm in diameter and also serves to limit the transverse velocity components of the molecules, which will reduce the Doppler broadening in the spectra (see section 1.3.3). The pressure in the buffer chamber is about 10^{-6} mbar, which means that the environment can be considered collision-free. However, the transverse velocity component of the beam needs to be reduced further before a measurement can be performed. To this end a second skimmer is used, 3 mm in diameter, to separate the buffer chamber from the third chamber, the measurement chamber. Because the distance between the two skimmers also influences the number of molecules reaching the measurement chamber it can be changed. When argon is used as a buffer gas the resulting Doppler width in the spectra, depending on the position of the second skimmer, is between 15 and 25 MHz at a typical transition frequency of 30000 cm^{-1}. Behind the measurement chamber is a fourth vacuum chamber which is separated by a valve. It contains a quadrupole spectrometer and is used to align the molecular beam through the skimmers. The actual measurement takes place in the third chamber, where the UV laser beam (see next section) crosses the molecular beam perpendicularly. The total undispersed fluorescence emitted by the molecules is collected at right angles to these beams with the help of collection optics and imaged onto a UV-sensitized photomultiplier tube.

Apart from the excitation wavelength all important experimental parameters are determined in the first section of the setup. First a nozzle size has to be chosen. Smaller nozzles induce more collisions in the expansion region and clusters are therefore more easily formed. Obviously, whether this is an advantage or not depends on the experiment. On the other hand, a larger nozzle leads to a larger amount of molecules in the molecular beam and a corresponding increase in signal, but when too many molecules enter the first vacuum chamber the resulting rise in chamber pressure may lead to a breakdown of the molecular beam. Typical nozzle sizes are between 90 and 230 μm. Second, a buffer gas has to be chosen. Since it is generally undesirable for it to interact with the molecules and build clusters a noble gas is used. In this thesis argon will be used exclusively, but neon or helium can also be chosen if a further decrease of the amount of clusters in the beam is needed. Third, a sample temperature has to be set. A high vapor pressure is not desirable since it will deteriorate the optimal balance between sample molecules and buffer gas, so the temperature should only be high enough to reach a suitable vapor pressure. Fourth, a backing pressure has to be set. This is tricky as the optimal pressure depends on many different variables, including the three mentioned above. In general though, high pressures favor cluster building whereas lower pressures are more suitable when monomers are to be studied. The usable pressure range is 150-800 mbar, and depending on the experiment the optimal value may be anywhere between these two extremes. Pressures below 150 mbar cannot be used as the rotational cooling will be insufficient; high pressures can only be used in combination with a small nozzle since a breakdown of the molecular beam will otherwise occur. Last, for measurements on water clusters the temperature of the water reservoir has to be set. Just as for the sample molecules high vapor pressures are to be avoided, which in the case of water means that a temperature between -20 and -5 °C should be used.

1.2.2   Laser System

The laser system that produces the narrow-band, tunable UV light consists of several stages. The first is a pump laser, and several different ones have been used to perform the experiments described in this thesis. These were an Ar^+ ion laser (Coherent Innova 100) at a wavelength of 514.5 nm and two different frequency doubled continuous wave YAG lasers (an ELS Versadisk Yb:YAG running at 515 nm and a Nd:YAG (Spectra Physics Milennia X) operating at 532 nm), all with a maximum output power of 10 Watts. Between 6 and 7 Watts of pump laser light is coupled into a ring dye laser (Coherent 899-21) which produces between 600 mW and 1.20 W of narrowband tunable radiation. Its output wavelength can be scanned continuously over a range of 30 GHz (1 cm^{-1}). The total wavelength range that is accessible spans several tens of nm per dye. This beam is then coupled into an external folded ring cavity which contains a BBO crystal for frequency doubling (Spectra Physics Wavetrain). The cavity is locked to the incoming beam so that resonance is always maintained. Its output (between 5 and 50 mW with a bandwidth of about 1 MHz) is finally guided into the molecular beam machine and focussed at the crossing with the molecular beam.

To get a coarse estimate of the laser wavelength exiting the dye laser a monochromator is used. An exact frequency reference is obtained by measuring an iodine absoption spectrum and comparing this with tabulated lines.[5] Since it cannot be assumed that the scan speed of the dye laser is constant the spectra have to be linearised. This is done by recording the transmission peaks of a quasi confocal Fabry-Perot interferometer with a free spectral range of 149.9434(56) MHz and using these to fix relative frequencies. Finally, also the UV laser power exiting the molecular beam machine is measured.

The output from the photomultiplier tube is fed into a personal computer equipped with a multichannel analyzer card (FAST ComTec MCA-3/P7882). The same computer also houses a DAC card (ComputerBoards PCI-DAS1602/16) for the recording of iodine, etalon and power channels. The operating system used is a real-time Linux version (Fedora Core 5 with RTAI 3.4) whose kernel (2.6.15 vanilla) was patched (ADEOS nano-kernel). Spectra were taken using a measurement program written specifically for this purpose.

1.2.3   Applicability

Apart from the experimental method employed in this thesis many other tecnhiques are commonly used for molecular structure determination. Some well-known examples are NMR[6] and spectroscopic methods such as microwave, Fourier transform, IR vibrational and rotational coherence spectroscopy.[7] The main area where the technique described above distinguishes itself from all these is the fact that electronic spectroscopy is performed. This means that not only information on a molecule's structure in its ground state is obtained but also in its electronically excited state, while the type of transition gives the direction of the transition dipole moment in the molecule. Combined with the high accuracy that can be achieved this makes the method very powerful. However, every technique has its difficulties and drawbacks, and it is therefore a good idea to review the applicability of this method.

First of all, a molecule has to be chosen that fluoresces. Additionally, the excited state lifetime should not be too short, as the lifetime broadening (section 1.3.3) will otherwise wash out the rotational structure in the spectrum. These problems can be solved experimentally if a different detection technique is used. A wide range of options is available but a detailed account of these is beyond the scope of this thesis. Two of the alternatives are currently being constructed in the lab: an ionization zone for the detection of molecular ions and a detection zone which employs sensitized phosphorescence.[8]

Second, the molecule shouldn't dissociate before it reaches a vapor pressure that's suitable for the experiments. Since this condition doesn't hold for many biological molecules this is a more serious limitation. It can be overcome by protecting functional groups prone to dissociation, but this has the disadvantage that in essence a derivative is measured rather than the actual molecule. Another solution is the use of a laser ablation source,[9,10] where molecules are evaporated by intense laser pulses, but since this is a pulsed technique a pulsed laser source will also have to be used which will negatively affect the accuracy of the measurements.

Third, as the molecules grow larger the separation between rotational energy levels decreases.[11] At some point they will start to overlap and it will no longer be possible to recognize any rotational structure in the spectra. As long as the spectral congestion is not too severe this problem can be overcome by employing an automated fitting procedure for the assignment of the spectra, such as the evolutionary algorithms discussed in section 1.4. Even when no transitions can be found that do not overlap with others, and manual evaluation has therefore become impossible, such an automated routine can still find the optimal solution. If, however, spectral congestion is too severe and no rotational information is present then the only solution would be to decrease the rotational temperature, which in practice is very hard.

Last, the setup uses continuous wave lasers and continuous detection. Although the fluence of a pulsed laser may be similar, the fact that the detection is also pulsed means that the background signal is lower. Therefore, the signal-to-noise ratio in pulsed experiments is generally better. Although this is not a fundamental drawback of the setup and the usable UV power output for systems such as the one described here is still on the increase, it does mean that not all interesting features that can be observed in pulsed experiments are accessible with this system. A compromise between both worlds, where some of the resolution is sacrificed for an increased signal-to-noise ratio, can be found in a pulsed dye amplifier (PDA).[12,13]

1.3   Molecular Rotation

1.3.1   Rigid Rotor Energy Levels

Since the experiments that will be described in this thesis produce spectra with rotational resolution, and this rotational resolution will be of key importance for understanding molecular structure, we will mainly be concerned with the rotational part of the molecules' wavefunction. If a rigid molecule is considered and it is assumed that the rotational part of the wavefunction can be separated from the rest, then an analysis of molecular rotation can be made by starting from its classical angular

momentum $\vec{P}$ which is given by[11]

$$\vec{P} = \vec{I} \cdot \vec{\omega}, \tag{1.1}$$

with $\vec{\omega}$ its angular velocity and $\vec{I}$ a 3x3 matrix, the components of which are:

$$
\begin{aligned}
I_{xx} &= \sum_i m_i(y_i^2 + z_i^2) \\
I_{yy} &= \sum_i m_i(z_i^2 + x_i^2) \\
I_{zz} &= \sum_i m_i(x_i^2 + y_i^2) \\
I_{xy} &= I_{yx} = -\sum_i m_i x_i y_i \\
I_{zx} &= I_{xz} = -\sum_i m_i x_i z_i \\
I_{yz} &= I_{zy} = -\sum_i m_i y_i z_i.
\end{aligned}
\tag{1.2}
$$

Here, the sum is taken over all atoms (with weight m_i) and (x_i, y_i, z_i) refer to the coordinates of each atom in the chosen axis system. It's always possible to choose the axes in such a way that this matrix is diagonal. This is the principal axis system and is usually designated by (a, b, c), with a the axis around which the moment of inertia is smallest and c that around which it is largest.

For a symmetric top molecule one of the principal axes coincides with the axis of symmetry (commonly taken to be the z-axis). If it corresponds to the a-axis, the molecule is a prolate symmetric top; if it corresponds to the c-axis it is an oblate symmetric top. For a description of the symmetric top wavefunctions, the fact that z coincides with either a or c means that J_z, the operator which projects the total angular momentum $\vec{J}$ onto the molecule-fixed axis z, now commutes with J_Z (the projection of $\vec{J}$ on the space-fixed axis Z) and J^2 so that a common set of eigenfunctions can be derived. These eigenfunctions are usually designated as $|J, K, M>$ according to the eigenvalues corresponding to the J^2, J_z and J_Z operators, respectively:

$$
\begin{aligned}
< J, K, M | J^2 | J, K, M > &= \hbar J(J+1) \\
< J, K, M | J_z | J, K, M > &= \hbar K \\
< J, K, M | J_Z | J, K, M > &= \hbar M,
\end{aligned}
\tag{1.3}
$$

with

$$
\begin{aligned}
J &= 0, 1, 2, \ldots \\
K &= J, J-1, \ldots, -J \\
M &= J, J-1, \ldots, -J.
\end{aligned}
\tag{1.4}
$$

The eigenfunctions can be given analytically, and the problem of finding the rigid rotor energy levels is in principle solved.

For the asymmetric rotor things are more complicated. Because it does not possess an axis of symmetry that corresponds to the a or c axis, K is no longer a good quantum number and the eigenfunctions can no longer be given analytically. They therefore have to be expanded in some complete orthogonal basis set; a natural choice are the symmetric top wavefunctions. For a slightly asymmetric rotor the K value of the limiting symmetric top is indicated by K_{-1} in case it is almost prolate and K_1 for a near-oblate symmetric top. Although these are only pseudo-quantumnumbers they are very useful in a description of the general asymmetric top when all near-oblate asymmetric top levels are connected with a near-prolate energy level as indicated in figure 1.2. The asymmetric rotor functions are usually given in terms of these identifications and indicated by $J_{K_{-1}K_1}$.[a]
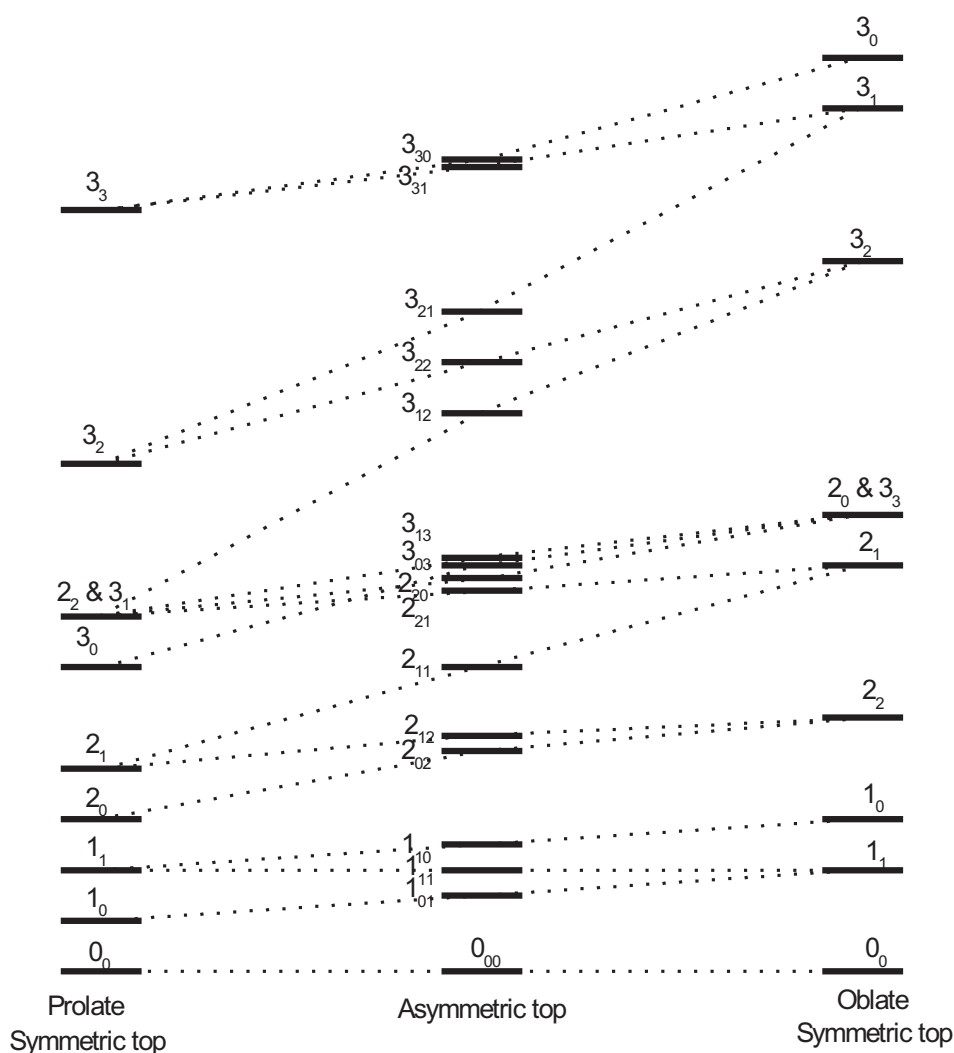
Figure 1.2: Correlation between asymmetric and symmetric top energy levels.

To determine the actual rotational energies of the general asymmetric rotor we

---

[a]It is assumed here that a field-free rotor is considered, and the energy levels therefore do not depend on M

now have to find the eigenvalues of the Hamiltonian H:

$$H = AJ_a^2 + BJ_b^2 + CJ_c^2, \tag{1.5}$$

where $A, B, C = h/(8\pi^2 I_{a,b,c})$ are the molecule's rotational constants in Hz. This requires diagonalisation of $H - \lambda I$ (with λ the energies we are looking for and I the identity matrix), which for a given J is a square matrix of size $2J + 1$. For the asymmetric rotor this has to be done numerically and for direct diagonalization this operation scales as J^3. Even though the matrix is sparse, so that some more efficient diagonalisation routines can be used, the calculation of energy levels for high J values ($J \gtrsim 50$) quickly becomes very expensive.

1.3.2   The Nonrigid Rotor

One type of nonrigidity will be very important for the molecules discussed in this thesis: tunneling. To account for tunneling a potential energy term has to be added to the free rotor Hamiltonian. A convenient choice is to expand the potential energy surface separating the potential minima between which the tunneling motion takes place using periodic functions with a period equal to $2\pi/n, n \in \mathbb{N}^*$:

$$V(\alpha) = \sum_i \frac{V_{in}}{2}(1 - \cos in\alpha), \quad i \in \mathbb{N}^*, \tag{1.6}$$

where α is the tunneling coordinate.[11] One possible way of solving the eigenvalue problem for this Hamiltonian is to assume that the tunneling occurs with respect to a rigid molecular frame, which means that it is not coupled to any modes of internal vibration. The principal axis method will be used to describe the internal motion, where the axis around which the internal motion can be described is related to the inertial axis system of the entire molecule and all eigenstates are deduced as a function of the relative orientation of the two. The torsion-rotation Hamiltonian is then given by:

$$H = H_r + H_t + H_{rt}, \tag{1.7}$$

where

$$\begin{aligned}
H_r &= AJ_a^2 + BJ_b^2 + CJ_c^2 + F(\vec{\rho} \cdot \vec{J})^2, \\
H_t &= FJ_\alpha^2 + \frac{1}{2}\sum_i V_{in}(1 - \cos in\alpha), \\
H_{rt} &= -2F\vec{\rho} \cdot \vec{J}J_\alpha.
\end{aligned} \tag{1.8}$$

In this equation, the relationship between the axis of internal motion and the inertial axes is given by:

$$\rho_g = \frac{\cos(\eta_g)I_\alpha}{I_g}, \tag{1.9}$$

with η_g the angle between the internal motion axis and main inertial axis I_g (g=a,b,c), I_α the moment of inertia of the internal motion with its corresponding reduced rotational constant F_α and $J_\alpha = -i\hbar\frac{\partial}{\partial\alpha}$. The relationship between F_α and the F from Equation 1.8 is:

$$F = \frac{F_\alpha}{1 - I_\alpha \sum_g \cos^2 \eta_g / I_g}. \tag{1.10}$$

H_r and H_t are the effective rotational and torsional Hamiltonians, respectively. Although these contain terms foreign to the pure rotational and torsional Hamiltonians, they do not couple the rotational and torsional parts and therefore merely constitute a redefinition of the respective rotational constants. H_{tr}, however, mixes the rotational and torsional eigenfunctions. If the barrier to internal motion is assumed to be high, this term can be treated most conveniently as a perturbation on the eigenfunctions of $H_r + H_t$.

In this thesis, two cases will be encountered: proton transfer from one site to another ($n = 2$), and threefold internal rotation ($n = 3$). In the first case, the barrier will be high for the molecules that will be studied. This means the sum in equation 1.6 can be truncated after the first term (V_2). The tunneling barrier will be high enough to consider the potential minima on both sides of the barrier as essentially non-interacting, which makes analysis straightforward.

Analysis of threefold internal rotor spectra will be more complicated. Here, both the V_3 and V_6 terms of equation 1.6 will need to be retained. Since the rotor itself, when attached to a nonlinear molecular frame, has C$_3$ symmetry (or $D_3(M)$ symmetry when the molecular frame has a mirrorplane which contains the axis of internal rotation), the rigid rotor wavefunctions can be classified under the irreducible representations of these groups. They consist of one or two nondegenerate A species and a doubly degenerate E species. Since these species only differ in their character under symmetry operations affecting the internal rotation angle α and the dipole moment is independent of this angle, these species do not couple and no transitions between them are allowed. This means that they give rise to two distinct, separate spectra. For most purposes it will suffice to limit the perturbation treatment to fourth order, in which case the A rotational lines will exhibit a normal pseudorigid rotor spectrum, possibly with pseudocentrifugal distortion effects. Only the E type transitions will therefore contain lines that cannot be fit to such a pseudorigid rotor Hamiltonian and are normally forbidden. The separation between the A and E spectra sensitively depends on the height and width of the tunneling potential. For this reason the A-E separation, if resolvable, serves as a sensitive probe of the potential barrier hindering internal rotation.

1.3.3 Intensities and line shapes

Since we are not interested in a measurement of transition strengths the absolute intensities of rotational transitions will not be of importance for the experiments. In

general, the relative strength of dipole allowed transitions between the ground state ψ' and the excited state ψ'' is given by the probability amplitude:[7]

$$P = \langle \psi' | \tilde{\mu} | \psi'' \rangle = \int \psi'^* \tilde{\mu} \psi'' d\tau, \tag{1.11}$$

where $\tilde{\mu}$ is the electric dipole moment operator; the integral is often referred to as the transition dipole moment. Like in section 1.3.1 the overall wavefunction is now assumed to be separable into electronic, vibrational, rotational and nuclear parts, and only the rotational part will be considered. It is then possible to use the eigenfunctions of the effective rotational Hamiltonian as wavefunctions in equation 1.11. The linestrength, which is proportional to the absolute square of the probability amplitude, can in this case be written as:

$$A_{r'r''} \propto |P|^2 = |\mu_a \langle \psi'_r | \Phi_{Za} | \psi''_r \rangle|^2 + |\mu_b \langle \psi'_r | \Phi_{Zb} | \psi''_r \rangle|^2 + |\mu_c \langle \psi'_r | \Phi_{Zc} | \psi''_r \rangle|^2. \tag{1.12}$$

In this equation the dipole moment operator μ has been resolved along the space-fixed axis Z using the angles ϕ and θ so that:

$$\begin{aligned}
\mu_a &= \mu \sin\phi \cos\theta \\
\mu_b &= \mu \sin\phi \sin\theta \\
\mu_c &= \mu \cos\phi,
\end{aligned} \tag{1.13}$$

and $\Phi_{Z(a,b,c)}$ are the direction cosines between the molecule-fixed (a, b, c) axes and the space-fixed Z axis (the polarization axis of the laser beam).

The probability of a vibronic transition and thus the relative intensity of a vibronic band depends on the square of the overlap integral of the vibrational wave functions of both electronic states and is called the Franck-Condon factor. The overlap integral is determined by the relative shift of the two potential energy curves connected by the vibronic transition along the normal coordinates Q of both states and the vibrations involved:

$$FC = \left| \int \Psi'_v(Q')^* \Psi''_v(Q'') dQ' \right|^2 = \langle v' \dots v'_N | v'' \dots v''_N \rangle^2, \tag{1.14}$$

where $\Psi_v(Q)$ are the N-dimensional vibrational wavefunctions. The normal coordinates Q' of the excited state and Q'' of the ground state are related by the linear orthogonal transformation given by Duschinsky.[14]

The relative strength of transitions in the spectra equals the linestrength multiplied by the relative population in the initial state. Since the supersonic expansion of molecules in the setup does not produce an exact Boltzmann equilibrium we may use a two-temperature model to describe the initial population distribution. In this model the variation with the energy of the initial state E is given by

$$n(T_1, T_2, w_T) = n_0 \left(\exp^{-E/kT_1} + w_T \exp^{-E/kT_2} \right), \tag{1.15}$$

where T_1 and T_2 are the two temperatures, w_T their relative weight and k the Boltzmann constant.

To accurately describe the transitions in the spectra line broadening effects should also be considered. In the experiments there are two main causes of broadening: Doppler broadening and lifetime broadening.

Doppler broadening occurs because the molecules under investigation have a small velocity component along the laser beam. The lineshape that corresponds to this effect is a Gaussian function which takes the form:

$$S_D(\nu - \nu_0) = \exp\left[-4\ln 2\left(\frac{\nu - \nu_0}{\Delta\nu_D}\right)^2\right]. \tag{1.16}$$

The distance between half-intensity points (FWHM) that results is here designated as $\Delta\nu_D$ and depends on the transverse velocity distribution of the molecules; ν_0 is the center frequency of the transition. In the apparatus this can only be changed by altering the distance between the skimmers (see section 1.2), which varies the angular distribution of the molecules passing into the measurement chamber to some extent. Depending on this distance, the Doppler broadening is between 15 and 25 MHz.

Lifetime broadening, as the name suggests, occurs as a result of the limited lifetime of the electronically excited state. Through the Heisenberg uncertainty relationship, this leads to a Lorentz function which has the following form:

$$S_L(\nu - \nu_0) = \frac{(\Delta\nu_L)^2}{4(\nu - \nu_0)^2 + (\Delta\nu_L)^2}. \tag{1.17}$$

The width of this distribution, $\Delta\nu_L$, is related to the excited state lifetime τ through:

$$\Delta\nu_L = \frac{1}{2\pi\tau}. \tag{1.18}$$

Although most formulas that are needed for data analysis have now been derived, one last important point has so far been neglected: selection rules. Aside from the usual dipole selection rules, $\Delta J = 0, \pm 1$, $\Delta M = 0, \pm 1$ (and in the rigid rotor also $\Delta K = 0, \pm 1$), which arise from conservation of angular momentum in a transition, other rules may also apply if the molecule possesses some symmetry. This is exemplified by the case of threefold internal rotation discussed in section 1.3.2, where the symmetry of the rotor forbids A↔E transitions. Apart from disallowing certain transitions completely, molecular symmetry can also alter their relative intensities. Therefore molecular symmetry now has to be discussed.

1.3.4 Molecular Symmetry

In 1963 Longuet-Higgins defined the molecular symmetry group and showed that it is the preferred way of describing the symmetry of molecules since it also applies to nonrigid systems.[15] Rather than using rotations and reflections as its basic symmetry

operations, as is done in point groups, it employs nuclear permutations and inversion of the coordinate system.[16]

If the molecular symmetry group for a molecule is set up, the first task is to determine all nuclear permutations and all nuclear permutations combined with inversion that leave the molecule unchanged; if the inversion and identity operations are also added the resulting group is called the complete nuclear permutation inversion (CNPI) group. The molecular symmetry group is obtained from this by deleting all elements that interconvert two forms which are connected by an insuperable energy barrier, called unfeasible elements. For example, an operation interchanging both hydrogen atoms in a water molecule is feasible (since it doesn't alter the molecule), but one interchanging both carbon atoms in an ethane molecule (while leaving the hydrogens in place) is not. Here the strength of the molecular symmetry group can already be seen, in that we are able to choose which elements are allowed in the molecular symmetry group. This means that, depending on the resolution of the experiment, we can for example choose whether or not a cyclic permutation of the hydrogen atoms in a methyl rotor attached to a nonsymmetric molecular frame is a feasible operation. For rigid molecules, the molecular symmetry group is isomorphic with its point group; for nonrigid molecules its order is higher.

Once it has been determined to which symmetry group the molecule belongs its character table is needed. We have to find out what effect each of the group's generators has on the molecule's wavefunction. For a separable wavefunction ($\psi = \psi_e \psi_v \psi_r \psi_n$) the symmetry of each part can be determined separately, after which the symmetry of a particular energy level simply follows by multiplication of the individual characters.

For an $S_1 \leftarrow S_0$ transition the character of the electronic wavefunction equals that of the transition dipole moment, which can therefore easily be derived from an origin spectrum. Determining the character of any particular vibration is also straightforward and is done through direct analysis of its behavior under the operations of the group's generators. Analysis of the rotational part is more involved, and its character has to be determined by studying the transformation properties of the Euler angles (θ, ϕ, χ), which describe the orientation of the molecule-fixed (a, b, c) axis system to the space-fixed (X, Y, Z) axes, as well as those of internal coordinates (like internal rotation angles). The resulting character of asymmetric rotor energy levels is found to depend only on the evenness or oddness of K_a and K_c.

In the absence of a resolvable hyperfine structure and neglecting any coupling between the different parts of the wavefunction (such as rotation-vibration interaction) a symmetry label can now be attached to each energy level. The dipole allowed transitions between levels are those that are connected by the species of the dipole moment operator. This operator belongs to the antisymmetric representation Γ^*, which is even for all permutations and odd for all permutations with inversion. The nuclear part of the molecular wavefunction determines the relative intensities of the transitions. It is possible that no nuclear spin species combines with a certain rovibronic level, so that its relative weight is zero and the corresponding transition is not allowed.

1.4 Evolutionary Algorithms

To aid the analysis of rotationally resolved spectra an automated fitting procedure was developed.[17–19] The advantage is twofold: first, the spectra can be analysed very quickly, and in favorable cases a full analysis only requires a few minutes on a normal desktop computer. More importantly, a solution can be obtained even when the structure of the spectrum is not understood in detail (or, indeed, visible when confronted with overlapping spectral transitions). To solve complex, multi-dimensional problems such as fitting one of the spectra a quick and very reliable approach is the use of evolutionary algorithms. While many different implementations exist they are all based on the same general principles, inspired by the processes of reproduction and natural selection in nature. The concepts common to these implementations will briefly be discussed.

An individual is a trial solution to the problem and therefore consists of a complete set of parameter values that is necessary for the description of a spectrum (such as rotational constants, transition dipole moment direction and temperature). In a first step the value of every parameter is chosen at random, each within a range set by the user. A given number of individuals (called a population) is generated this way, after which the quality of each individual is evaluated. This evaluation proceeds through a fitness function, which in our case is essentially a modified overlap function between the experimental and calculated spectrum. The general idea is now to use the information contained in the best solution(s) (parent(s)) in the generation of a new set of trial solutions (offspring). This process continues cyclically until the fit has converged. The creation of new trial solutions in each generation based on the best solution(s) from last generation ensures that the best solution will progressively improve. Three different implementations have been included in the 'EA' program that is used to fit the spectra: genetic algorithms (GA) and two Evolutionary Strategies (the derandomized-ES DR2 and the Covariance Matrix Adapted-ES (CMA-ES)).

In the GA algorithm, the parameter values from two parents are randomly combined to create the offspring. To protect the algorithm from getting stuck in a local minimum of the error landscape some parameter values are changed at random for a small number of solutions, called a mutation. Since we don't want mutations to deteriorate those individuals that are already quite good the best solutions within a generation are excluded from this process (elitism). The genetic algorithm typically uses a population size of around 300 individuals and about the best half of the solutions within a generation is allowed to reproduce. The GA typically needs between 300 and 500 generations to converge.

In the derandomized-ES DR2 algorithm offspring is produced by creating a set of random mutation vectors and applying these to a parent; each mutation vector thus gives a new individual.[20] Typically about 200 offspring are created this way. The parent(s) to be used for the next generation are now either computed from the old parent(s) and the best of its offspring or from its offspring alone. The strength of the DR2 algorithm lies in the fact that the mutation vectors leading from one (set of) parent(s) to the next are stored for the last couple of generations, and the correlation between these vectors is used to adapt the parameter values to be used in the computation of the next offspring. This means that the algorithm, unlike the genetic algorithm, has a sense of direction and can feel the direction in which the best

solution is most likely located. This approach makes the algorithm both very fast and reliable,[21] and convergence is generally reached within 200 generations. Even though the calculation of a single trial solution is more expensive than is the case for the GA, an increase in computation speed by a factor of 2 results. For this reason the DR2 algorithm has largely superseded the GA.

Although much more advanced, the basic operation of the CMA-ES algorithm is the same as that of the DR2. The main differences are that the search strategy parameters are now chosen by the algorithm itself rather than by the user, and that a more complicated procedure is used to compute the mutation vectors to be used for the next generation, where instead of adapting the step size for each parameter individually the complete covariance matrix is adapted.[22] This approach endows the CMA-ES with several invariances, which implies a more general applicability and makes it ideally suited for solving problems with a wild, erratic error landscape. It also means that far larger parameter ranges can be specified than for the DR2 algorithm.[23]

1.5 From Rotation to Structure

The principal moments of inertia $I_{a,b,c}$ are connected to the rotational constants A, B, C through the relationship:[11]

$$I_a = \frac{h}{8\pi^2 A}, \qquad I_b = \frac{h}{8\pi^2 B}, \qquad I_c = \frac{h}{8\pi^2 C}, \tag{1.19}$$

where h is Planck's constant. Once the rotational constants for the molecule have been determined, this expression combined with equation 1.2 leads to a constraint on the possible mass distributions and thus on the structure. For example, the inertial defect Δ, which is defined as

$$\Delta = I_c - I_a - I_b, \tag{1.20}$$

is zero for planar molecules and becomes negative for non-planar systems. In some cases these constraints suffice to determine the conformation of a molecule. However, when we want to extract the complete geometry we are posed with a problem: we only have three rotational constants while the molecules we are interested in possess (3N-6) degrees of freedom, which is larger for N$\geq$4. The usual solution to this is to measure isotopically substituted species. Isotopic substitution is a nuclear effect while a molecule's geometry is primarily determined by its electronic configuration, so that the subsitution is expected to have little effect on the geometry. Since the substituted molecule has a different mass distribution, its rotational constants will differ from the parent molecule. Thus each isotopomer gives three new rotational constants, and hence three additional molecular parameters can be determined.

In principle the complete molecular structure can be deduced this way; in practice the size of the molecules makes this procedure very cumbersome. In most cases we therefore choose to measure as many isotopomers as necessary to determine the values of the most interesting geometric parameters and consider the geometry of the rest of

the molecule to be known, either from measurements on related molecules or, more commonly, from calculations. A least-squares fit of the rotational constants using the parameters we are interested in as variables then gives the molecular geometry.[24] For molecular clusters we are often most interested in the intermolecular parameters, and the approach outlined above therefore usually means that intramolecular parameters of the constituent molecules are kept fixed in the determination of the cluster structure.

It is important to realise that the molecular parameters that are derived using this procedure include zero-point energy vibrational effects and are therefore different from those for the hypothetical vibrationless state (called the equilibrium parameters). It also means that the derived structures of different isotopomers will not be the same. When several isotopomers are used to deduce a molecular geometry, this geometry will therefore depend on which isotopomers are used in the analysis. If no attempt is made to correct for these effects the resulting parameters are called effective parameters. Whenever a molecule possesses symmetry, or if the fit is insensitive to a certain parameter, a more elegant approach due to Kraitchman might be used;[25] a structure derived this way is called a substitution structure. The use of Kraitchman's equations tends to cancel zero-point vibrational effects, and molecular parameters derived from substitution structures are therefore more reliable.

1.6   Quantum Chemical Methods

Although the focus of this thesis is on the analysis of experimental data, many important conclusions will be (partially) based on quantum chemical calculations. It is therefore important to briefly introduce the basic concepts behind the most commonly used methods.[26]

The only molecular system for which the geometry and energy levels can be derived exactly is the H_2^+ molecule; all other systems have to be solved numerically. Because the computational effort needed in the derivation of such a solution invariably increases with the size of the system under investigation, the level of theory which can be used always depends on this size. The result is that, in order to achieve the highest possible accuracy for a certain system within the computational budget, the most suitable type of calculation depends on the property of interest. This means that, for the same system, different methods and basis sets are commonly employed for the calculation of different properties. This is also the reason why two very different types of calculation are used in this thesis: wave function based *ab initio* quantum chemical methods and density functional theory.

The wave function based approach usually starts out with the Born-Oppenheimer approximation, where it is assumed that the nuclei move on a potential energy surface which can be determined solely by solving the electronic part of the Schrödinger equation, which only depends parametrically on the nuclear coordinates, and neglect of relativistic effects. Assuming the nuclei to be at rest the energy of a nuclear configuration can then be calculated as:

$$
\begin{aligned}
E_e &= \frac{\langle \Psi_e | H_e | \Psi_e \rangle}{\langle \Psi_e | \Psi_e \rangle} \\
H_e &= T_e + V_{ne} + V_{ee} + V_{nn},
\end{aligned}
\tag{1.21}
$$

where T_e is the electron kinetic energy and V_{ne}, V_{ee} and V_{nn} are the nuclear-electron, electron-electron and nuclear-nuclear interaction potentials, respectively. The electronic wavefunctions Ψ_e are described by a trial solution, which is commonly constructed using products of one-electron wavefunctions and spin functions, called molecular orbitals. When the components of the N molecular orbitals (ϕ_i) for a given system are arranged along the columns of a matrix, as a function of the positions of the N electrons along the rows, then the determinant of this matrix automatically fulfills the Pauli exclusion principle. This is called a Slater determinant.

It can be shown that the wavefunction which minimizes the energy is the best approximation to the real solution, which therefore serves as a target for the optimization procedure. The simplest way to obtain a solution is now to take a single Slater determinant as a trial wavefunction. This assumption leads to the so-called Hartree-Fock equations, which can be solved iteratively. The corresponding technique is called self-consistent field (SCF) theory. The result of using a single Slater determinant is that electron-correlation effects are only treated in an average fashion, for which reason they are sometimes also referred to as mean-field theory. To mend this situation several more advanced models, which are collectively called electron correlation methods, have been developed. The three most important ones are configuration interaction, Møller-Plesset perturbation theory and coupled cluster methods.

Each of the three methods mentioned above starts by generating excited Slater determinants, where one or several electrons have been moved to an excited state. In configuration interaction (CI) the molecular orbitals for each of these excited Slater determinants are held fixed to those determined at the Hartree-Fock level, and the relative weights of the excited Slater determinants is now optimized as well. The types of excitations that are added are indicated by a letter and added to the end of the corresponding name: S for single excitations, D for double excitations and so on, leading to CIS, CID, CISD, etc. When the molecular orbitals are optimized as well the technique is called multi-configuration self-consistent field (MCSCF). In the special case where the configurations to be used in the expansion are selected by partitioning the orbitals into active and inactive spaces, as is often done, it is referred to as complete active space self-consistent field (CASSCF).

In Møller-Plesset (MP) perturbation theory the electron-correlation effects are treated as a perturbation to a sum of molecular orbital energies. The perturbation term is the exact electron-electron potential (V_e) minus twice its average. Since a sum over molecular orbital energies counts the electron repulsion twice, the first order correction yields the Hartree-Fock energy levels. Each additional term improves on this, and the method is termed by the order at which the expansion is cut off (MP2, MP3, etc.) Although this approach is very powerful, it has the drawback that the perturbation is not necessarily small, and the analysis may converge very slowly, if at all.

In coupled cluster (CC) methods, finally, excited Slater determinants are generated by operators that excite one or several electrons. By writing the exact wavefunction

of a system as a power series of such operators acting on the Hartree-Fock wavefunction it becomes mathematically possible to include all corrections of a given type to infinite order. The major difference with Møller-Plesset theory is that, due to this, all contributions of the same relative size are treated at the same step in the expansion, and results are therefore more likely to become better with each additional term. Like with CI methods, the corresponding name is generated by adding the type(s) of excitations to the name, giving rise to CCD, CCSD, etc. Since this series quickly grows in computational effort a few special variations of coupled cluster methods exist. In one of these, CCSD(T), the triples contribution is calculated from perturbation theory and added to a normal CCSD calculation. Alternatively, the full CCSD or CCSDT calculation can be simplified by applying perturbation theory to the most expensive step and retaining only the leading term, in which case the method is called CC2 or CC3, respectively.

Quite different from all models mentioned above, which are based on wave-mechanics, is density functional theory (DFT). Rather than describing the energy of a system through its Hamiltonian and wavefunction (equation 1.21) it employs an electrostatic model where the electron distribution is described using a density functional. The main task is now to use a functionals which properly relates the electron density to an overall energy for a given system. Many different forms exist, the most elaborate of which also depend on the derivatives of the energy. The names these DFT methods carry, like the commonly used B3LYP, are related to the names of the functionals. An important extension of the DFT method is the combination with multi-reference configuration interaction methods (DFT/MRCI). This allows for the computation of electronically excited states with multi-configurational character, which cannot be tackled using normal DFT methods.

The computational cost of the methods which are most commonly used in this thesis increases in the order DFT-MP2-CC2; larger calculations are not feasible for the systems under investigation here. Not only does the computation time for a particular system increase with the use of more advanced methods, but critically the scaling with the number of basis functions gets worse as well. For DFT methods it increases linearly, for the MP2 and CC2 methods it increases with the fifth power and CCSDT is already an eighth order method. This means that the more advanced the method, the smaller the basis set needs to be in order to be able to perform the calculation. For this reason the basis sets for wave mechanical methods such as MP2 and CC2 are usually restricted to the chemically interesting orbitals; the rest is either omitted or modeled crudely. Since this may introduce additional errors it is evident that the optimal basis set size has to be balanced against the chosen method. This, then, is the main reason that different methods are used for the calculation of different properties. If, for example, we want to calculate the length of a van der Waals bond we may choose to include diffuse, long-range functions in our basis set. Although they may not improve the overall energy all that much, they might lead to a more accurate bond length. To make the calculation possible, this might mean that instead of the CC2 method the cheaper MP2 method is now chosen. On the other hand, the geometry of the rest of the molecule might be more accurate if a calculation at the CC2 level is made with a more limited basis set. The main drawback of both the MP2 and the CC2 technique is that they are not variational, which means that the energy found is not necessarily an upper limit to the global minimum energy and there is no

guarantee that the expansions which are employed will actually converge.

The interpretation of results from DFT calculations is more troublesome. Since they don't try to improve the energy of a system by progressively improving its wave-function but instead try to approximate the Hamiltonian, their accuracy depends on the chosen functionals. These generally were constructed with little guidance from theory and, as a consequence, their results can only be assessed by comparison with high-quality wave-mechanical methods or with experiments. However, they are also very cheap, which means that very large basis sets can be used and/or large systems can be studied. It is found that the structure of a system may be predicted with an accuracy comparable to the MP2 method at the cost of only an HF calculation. Transition frequencies and transition dipole moment (direction) can be determined with particularly high accuracy. On the other hand, van der Waals type interactions are usually modeled poorly.

The tunneling splittings in the benzoic acid dimer S_0 and S_1 states determined by high resolution UV spectroscopy

Five different isotopologues of the benzoic acid dimer as well as a vibronic band located 57 cm^{-1} above the electronic origin, which is assigned to the out-of-plane butterfly motion, have been measured using rotationally resolved UV spectroscopy. From these measurements a ground state structure with C_{2h} symmetry was deduced whereas the symmetry is lowered to C_s in the S_1 state. The center of mass distance between both monomer moieties was found to increase upon electronic excitation, indicating a decrease in hydrogen bond strength. The tunneling splittings in the S_0 and S_1 state could also be determined, yielding 1385.2 $\pm$ 0.7 MHz and 271.2 $\pm$ 0.7 MHz, respectively, corresponding to an increase in barrier height by 7.2 % upon electronic excitation.

2.1   Introduction

It is well known that hydrogen bonding is very important in biological systems and the topic has therefore been the subject of a considerable amount of research. Some systems employ multiple hydrogen bonds to connect molecular subunits; most notable among these is DNA, the base pairs of which are connected by double or triple hydrogen bonds. Because of their high symmetry the dimers of carboxylic acids like formic acid, acetic acid and benzoic acid have become model systems for double hydrogen bonding. Their carboxy groups link up to create a cyclic, eight-membered ring leading, in the examples above, to a ground state dimer structure of C_{2h} symmetry. This doubly hydrogen bonded structure is so strong that even at room temperature mostly dimers are present.

Since many biologically relevant processes involve proton transfer, one of the most interesting aspects of carboxylic acid dimers is the possibility of double proton tunneling. The tunneling path has long been the subject of debate however, resulting in theoretical estimates for proton transfer times spanning several orders of magnitude

(see, e.g., Madeja and Havenith[27] and references therein). Early calculations agreed that extensive geometry optimization of the transition state was necessary and that the transition itself was strongly coupled to a deformation of the whole molecular frame but the predicted barrier heights differed significantly.[28,29] Anomalous isotope effects observed for two formic acid dimer vibrations lead Maréchal to conclude that the transfer of protons could not be described as a simple tunneling motion in a double minimum potential.[30] Recent direct dynamics calculations using a single multidimensional coordinate system could explain a variety of gas phase and crystal data by carefully considering the contributions of various zero-point vibrations to the tunneling rates and assuming a negligible splitting in the electronically excited state.[31] Coupling between the tunneling mode and transverse modes was calculated to result in a more than 20-fold increase in the tunneling splitting. Recently, ^{1}H-NMR relaxometry and quasi elastic neutron scattering have shown conclusively that proton transfer in the benzoic acid crystal is a strongly correlated motion of the two protons while the tunneling path is little affected by deuteration in the carboxy group.[32] Fillaux *et al.* deduced from powdered crystal spectra that the potential barrier for the transfer of a single proton is already on the order of 5000 cm^{-1} which means that semiclassical jumping over the top is negligible.[33] In conclusion, the picture that has emerged is that double proton transfer in carboxylic acid dimers is a pure tunneling motion that occurs in concert, initiated by a zero-point vibrationally induced symmetric decrease of the distance between both monomer units.

Experimental data on the barriers for concerted proton tunneling reflect the sensitive dependence on the vibrations in both monomer units. In one of the earliest measurements on such systems, Costain found that the barrier height is larger than 6000 cm^{-1} in the CF_3COOH-$HCOOH$ system but less than 5000 cm^{-1} in CF_3COOH-CH_3COOH.[34] From fluid-phase absorption spectra the barrier heights in both formic and acetic acid dimers was deduced to be in the 6500-7000 cm^{-1} range when a symmetric double minimum potential is assumed.[35] Using high-resolution gas-phase IR spectroscopy on various isotopologues of the formic acid dimer, ground state tunneling splittings of 375 MHz and 474 MHz were observed for the $(DCOOH)_2$ and the $(HCOOH)_2$ dimers, respectively, whereas for the $(DCOOD)_2$ dimer an upper limit of 60 MHz was deduced.[27,36,37] This corresponds well with an effective barrier height of 6940 cm^{-1} for the fully protonated dimer.[31]

In the benzoic acid dimer attempts to determine the magnitude of the tunneling splitting have mainly been made using crystallographic methods. Although the benzoic acid crystal is composed of dimer units its lattice structure destroys the symmetry between both monomers, which results in two inequivalent potential minima and an inability to determine the tunneling splitting. However, with a suitable dopant the inequivalence between the two minima can locally be nearly lifted which allows a coarse estimate. The values found using thioindigo and selenoindigo as dopants were 8.4 ± 0.1 GHz and 6.5 ± 1.5 GHz, respectively.[38,39] Remmers *et al.*[40] studied the gas phase dimer using high resolution UV spectroscopy. The spectrum they recorded consisted of two rigid rotor components with a separation of 1107 ± 7 MHz between them which they assumed to be the difference between the tunneling splittings in the S_0 and S_1 states. These data were later re-analysed using genetic algorithms to yield a more accurate value of 1116 ± 3 MHz.[19] Smedarchina *et al.* were able to theoretically reproduce this value quite well (1920 MHz) by assuming it was due solely to

the ground state splitting, taking it to be zero in the excited state, and showed it corresponds to an effective tunneling barrier of 5793 cm^{-1}.[31]

The electronic coupling between the two monomer units in a doubly hydrogen bonded system depends very sensitively on the nature of the hydrogen bonds. Perhaps the most striking example of this is the 7-azaindole dimer, where electronic excitation was shown to be localized on one of the monomer units in all isotopologues with the exception of a single asymmetric doubly deuterated structure where it was found to be completely delocalized.[41,42] This is remarkable since the latter structure only differs from two others by a single deuteration in the aromatic ring. Fortunately, in many other systems the situation seems to be more clear-cut. In the 2-pyridone dimer the excitation is completely delocalized[43,44] whereas in carboxylic acids the excitation generally seems to be localized.[45–47] By observing a vibronic band in the gas phase benzoic acid dimer split into four components upon partial deuteration, Poeltl *et al.* showed that also in this system electronic excitation resides on a single half of the complex.[48,49]

With localization of excitation comes the question how feasible excitation transfer is. Very interesting in that respect is the existence of a vibronic band around 57 cm^{-1} above the benzoic acid dimer origin. This band is shared with many other carboxylic acid dimers, including the anthranilic acid dimer where it was recently found that, although there is a strong Franck-Condon progression in this mode, the dispersed fluorescence spectrum shows intensity only in even members of the progression.[45] Using DFT calculations the band was assigned as the intermolecular geared bend mode and the anomalous intensity patterns were explained by the possibility of excitation transfer between both monomers, altering the selection rules.[50] Due to large intramolecular geometry changes upon excitation of a monomer unit, however, the exciton splitting could not be observed directly. The corresponding benzoic acid dimer vibronic band shows the same anomalous intensity pattern, but a detailed analysis of IVR rates in isotopically mixed dimers lead to the conclusion that excitation transfer is only appreciable at higher excess energies.[49] Still, due to the absence of an intramolecular hydrogen bond the intramolecular geometry changes upon electronic excitation are much smaller in the benzoic acid dimer than in the anthranilic acid dimer, which means an exciton splitting might be observable in a spectrum of the BA dimer vibronic band. This was also suggested by Baum *et al.*, though given their upper limit of 0.3 cm^{-1} such a measurement would require high resolution.[51]

It should be noted here that the assignment of this band is the topic of some debate. Poeltl *et al.* initially suggested it to be the intermolecular geared bend mode. This was based on the fact that it forms strong combination bands with other vibrations ascribed to internal motions in the carboxy group, and on the observation that in the completely ring-deuterated (d$_5$-d$_5$) dimer the vibration frequency remains virtually unchanged.[48] They later favoured a re-assigment as either the out-of-plane bending motion or torsion given the fact that its frequency is unchanged in the electronically excited state.[49] Dispersed fluorescence spectra of this band lead Tomioka *et al.* to assume it is the torsion mode.[52] Quantum chemical calculations equally seem to disagree among each other. While, based on density functional theory (DFT) calculations, Nandi *et al.* assigned it as the geared bend motion,[53] Antony *et al.* claim it is the torsion mode[54] and following Florio *et al.* it could be either the geared bend or tilting motion.[55,56] Bakker *et al.* found that the difficulties in accurately describing

the hydrogen bonded modes also play a role in the calculation of higher vibrations (500-1900 cm^{-1}).[57]

In this paper the intermolecular structure in both the ground and electronically excited state will be determined from seven different dimer origins in high resolution spectra. Of particular interest will be the question if a reduction in the carboxy O$\cdots$O distance can be observed, as has been suggested[34,37] and if the excited state has a structure that is bent as has been proposed earlier.[40] Furthermore, analysis of a high resolution spectrum of the 57 cm^{-1} vibronic band will teach us whether an exciton splitting is present and which vibration is involved. Lastly, this assignment will allow us to determine the S$_0$ and S$_1$ state splittings separately as well as the relative tunneling barrier height.

2.2   Methods

2.2.1   Experimental procedures

The experimental setup for the rotationally resolved LIF is described elsewhere.[58] Briefly, it consists of a ring dye laser (Coherent 899-21) containing Rhodamine 110, pumped with 6 W of a frequency doubled Yb:YAG laser. The second harmonic of the dye laser output is generated in an external folded ring cavity (Spectra Physics Wavetrain). The resulting output power is typically between 30 and 40 mW and is constant during each experiment. The molecular beam is formed by co-expanding benzoic acid, heated to 390 ° K, and argon through a 100 μm nozzle into the vacuum using a backing pressure of 220 mbar. The molecular beam machine consists of three differentially pumped vacuum chambers that are linearly connected by skimmers (1 mm and 3 mm diameter, respectively) in order to reduce the Doppler width. In the third chamber, 360 mm downstream of the nozzle, the molecular beam is crossed at right angles with the UV laser beam. Imaging optics focus the total undispersed fluorescence from the excited molecules onto a photo-multiplier tube mounted perpendicular to the plane defined by the laser and the molecular beam, the output of which is then discriminated and digitized by a photon counter and transmitted to a PC for data recording and processing. The resulting Doppler width in this set-up is 25 MHz (FWHM). Relative frequencies are determined with a quasi confocal Fabry-Perot interferometer with a free spectral range (FSR) of 149.9434(56) MHz. The absolute frequency was obtained by comparing the recorded iodine absorption spectrum with tabulated lines.[5]

Benzoic acid was purchased from Caelo (p.A.), benzoic acid-d$_5$ (99.2 %) was obtained from CDN isotopes. Both were used without further purification. Benzoic acid-d$_1$ was produced by refluxing benzoic acid with an excess of D$_2$O and subsequent removal of solvent.

2.2.2   Computational methods

Ab initio calculations

Structure optimizations were performed employing the valence triple zeta basis set with one set of polarisation functions per atom (TZVP) from the TURBOMOLE li-

brary.[59,60] The equilibrium geometries of the electronic ground and the lowest excited singlet states were preoptimized using (time dependent) density functional theory with the B3-LYP functional and subsequently optimized at CC2 level within the resolution-of-the-identity approximation.[61,62] In order to ensure that the optimized structure is a real minimum the second derivatives were calculated numerically. No imaginary frequencies were obtained for any of the normal modes, showing that all optimized structures are minima.

The singlet state energies and wavefunctions were calculated using the combined density functional theory/multi-reference configuration interaction (DFT/M-RCI) method by Grimme and Waletzke.[63] The configuration state functions in the MRCI expansion are constructed from Kohn-Sham (KS) orbitals, optimized for the dominant closed shell determinant of the electronic ground state employing the BH-LYP functional.[64,65] All valence electrons were correlated in the MRCI runs and the eigenvalues and eigenvectors of eight singlet states were determined. The initial set of reference configuration state functions was generated automatically in a complete active space type procedure (including all single and double excitations from the five highest occupied molecular orbitals in the KS determinant to the five lowest virtual orbitals) and was then iteratively improved.

The first order transition state for the double proton transfer was preoptimized at the B3LYP level with the 6-31G(d,p) basis set, using the QST3 method[66] as implemented in the Gaussian03 program package.[67] With the so obtained structure the S_0 transition state was optimized at the RICC2 level using the TRIM (Trust Radius Image Minimization) method[68] implemented in the STATPT module from TURBOMOLE V5.8 with the same basis sets as for the minimum structures.

The derandomized-ES DR2 algorithm

Spectra were fit to a simple asymmetric rotor Hamiltonian using a derandomized (DR) evolutionary strategy (ES) which was developed in the mid-90's by Ostenmeier *et al.*[20] This special implementation which is also used here represents the second generation of derandomized ES and is abbreviated in the following as DR2.[21] It is here shown to be a very good alternative for the genetic algorithm based fits we have employed so far.[17,18]

Both evolutionary strategies like the DR2 algorithm and the genetic algorithm belong to the category of global optimizers known as evolutionary algorithms which were inspired by the biological processes of reproduction and natural selection. Their main difference lies in the fact that where the genetic algorithm tries to find a solution in parameter space by combining information from a set of trial solutions with the aim to create better ones, the DR2 algorithm can sense in which direction the fitness increases. In a first step of the DR2 algorithm, some trial solutions are generated (offspring) using a random distribution around some starting point (parent), each consisting of the complete parameter set necessary to describe the spectrum, and the quality of each solution is analyzed using a fitness function.[17,18] Provided one of the offspring is better than the parent this solution is selected and used to compute the next parent, which then serves as the starting point for an iteration of this cycle (generation). In the calculation of the parent for the next generation the DR2 algorithm makes use of the correlation matrix for successive changes in the parents (mutations).

In essence, this means that if for some parameter a parent has evolved in the same direction for several generations, so that their correlation in this parameter is positive, the most likely solution is assumed to be further in that direction and the next parameter mutation will be larger. Correspondingly, two anti-correlated mutations will lead to a smaller mutation size. By discriminating between mutation rates of different parameters the DR2 algorithm can reliably find the optimal solution within a relatively small number of generations.[20]

The usefulness of the DR2 algorithm in solving physical problems was shown by Shir *et al.* when several evolutionary algorithms were tested to be able to find the theoretical alignment of a sample of molecules in space with shaped laser pulses.[69] It turned out that the DR2 algorithm was not only the fastest but also the most reliable algorithm for this task, even outperforming several more advanced alghorithms like DR3 and CMA-ES. Given their success they then turned their attention to the problem of second harmonic generation (SHG) which, although much more difficult, showed that the DR2 algorithm again performed best.[21] When used to fit our spectra, the DR2 algorithm succeeded in obtaining good fits with a smaller population and within fewer generations compared to the genetic algorithm. Although the evaluation of a single trial solution in the DR2 algorithm is more expensive this lead to a reduction in the total computation time by a factor of two compared to the GA.

2.3 Results and Discussion

2.3.1 The dimer origin

The rotationally resolved spectrum of the $S_1 \leftarrow S_0$ origin of the benzoic acid dimer has been reported before[19,40] but was remeasured for this study. It is a b-type spectrum and shows a doubling of all lines due to concerted proton tunneling in the double hydrogen bond. The size of this splitting, Δ, was determined to be 1114.0 ± 1.0 MHz. The spectrum is very congested, with each apparent transition typically consisting of some ten individual rovibrational transitions. The transitions in these K-stacks all share the same ΔK_a but differ in the ground state level they originate from. Under our experimental conditions, transitions originating from ground state levels with J values up to 130 were needed to reproduce contributions to the spectrum with an intensity of at least 0.5 % of the strongest transitions. Since there is no thermal equilibrium in the molecular beam a two-temperature Boltzmann model was employed to describe the energy distribution. This resulted in rotational temperatures of $T_1 = 3.5$ K and $T_2 = 5.3$ K with a relative T_2 weight factor of 0.29.

Besides the d_0-d_0 dimer the $S_1 \leftarrow S_0$ origins of four more isotopologues were observed, which give rise to six additional spectra. These were the d_1-d_1 and d_5-d_5 homodimers, where the first is deuterated in the hydrogen bonds and the latter is completely ring-deuterated, and the d_0^*-d_1/d_1^*-d_0 and d_0^*-d_5/d_5^*-d_0 mixed dimers. Here the asterisk denotes the electronically excited moiety. Due to the weak electronic coupling between the two monomer units the electronic excitation is localized on one of the two and as a result both mixed dimers have two separate origins depending on which monomer is excited.[48] However, since the isotopic shifts upon deuteration are small the origins of these mixed dimers (with the exception of the d_5^*-d_0 dimer) are

not spectrally separated from the homodimers consisting of the excited monomer and have therefore not been resolved in previous studies. As an example the d_0^*-d_5 dimer spectrum is shown in Figure 2.1 together with a simulated spectrum. The simulation consists of two components: the d_0-d_0 dimer spectrum, for the simulation of which the molecular constants were held fixed to the optimal values determined there, and the d_0^*-d_5 dimer spectrum itself, blueshifted by 0.67 cm^{-1}. All other spectra and their simulations can be found in the online supporting information.
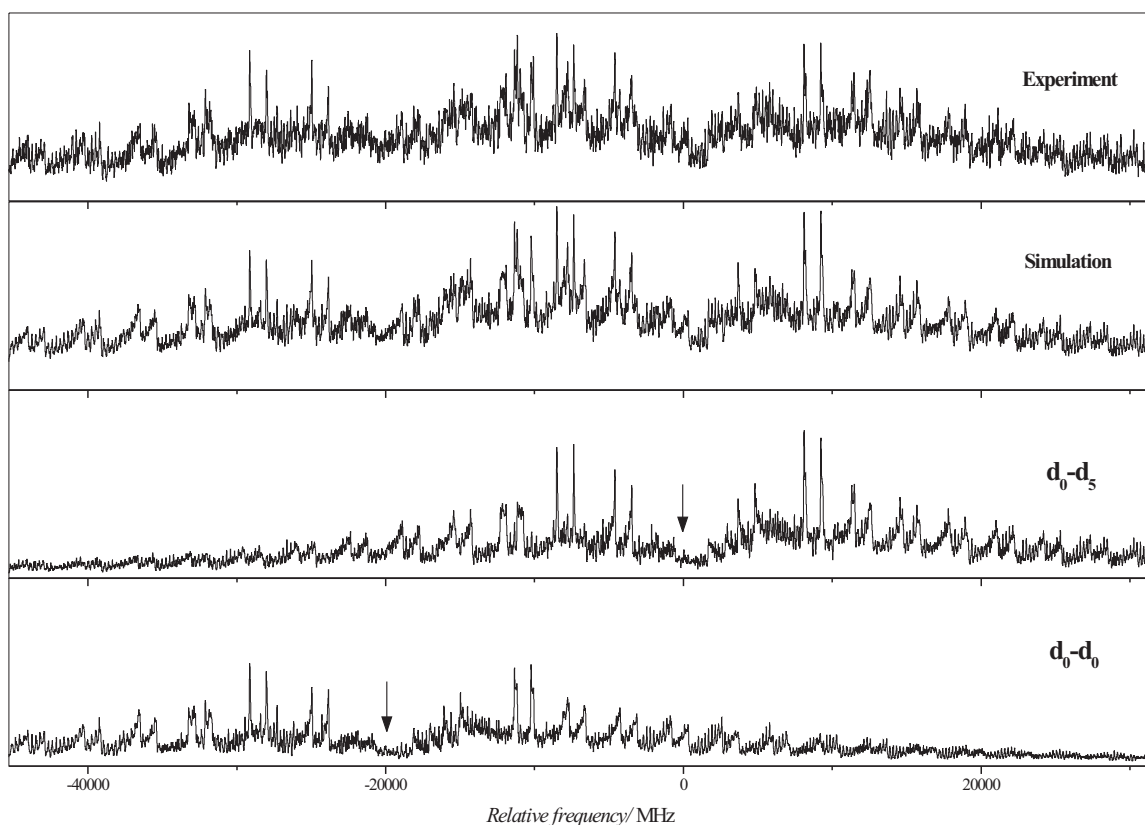
Figure 2.1: The electronic origin of the benzoic acid d_0^*-d_5 dimer at 35724.456 cm^{-1}. In the upper two traces the measured spectrum and the best simulation are given, as indicated. The lower two traces show the two components present in the simulation: the d_0^*-d_5 spectrum and the d_0-d_0 spectrum using the molecular parameters that were deduced from the analysis of a separate measurement. The arrows indicate the spectral origins.

Within the experimental uncertainty all initial simulations produced transition dipole moment directions corresponding to pure b-type spectra and no a-type or c-type components could be incorporated unambiguously. Therefore, to obtain the final results a pure b-type asymmetric rotor Hamiltonian was used. Also, for the the d_0^*-d_1 and d_1^*-d_0, and the d_0^*-d_5 and d_5^*-d_0 mixed dimers, the ground state rotational constants for each set were found to be the same within their experimental uncertainties, confirming that both spectra in each of these two sets indeed originate from a common ground state structure. In a final fit the ground state rotational constants for both spectra in each set were therefore forced to be equal. The parameters obtained from the final fits are given in Table 2.1. The lifetime broadening of the transitions was estimated to be 20 ± 10 MHz, corresponding to an excited state lifetime of 8 ±

4 ns. Unfortunately the congested nature of the spectra prohibits a more accurate determination.

Immediately obvious is the fact that the changes in the rotational constants $(\Delta B_g; g = a, b, c)$ are largely independent of deuteration, leading to spectra that are qualitatively very similar in appearance. It is also very striking that, both for the d_0^*-d_1/d_1^*-d_0 and the d_0^*-d_5/d_5^*-d_0 mixed dimers, the two spectra originating from the same ground state show substantially different tunneling splittings. In the case of the d_1-d_1 dimer no splitting could be observed. From test calculations it was estimated how large the separation between two closely spaced spectral components has to be in order to observe both. This resulted in a value of 45 MHz, which indicates an upper value for the splitting.

2.3.2 The 57 cm^{-1} vibronic band

In Figure 2.2 the rotationally resolved spectrum of the vibronic band located 57 cm^{-1} above the electronic origin of the d_0-d_0 dimer is shown. It can clearly be seen that although the signal-to-noise ratio is more than an order of magnitude lower than that of the origin spectrum the agreement between simulation and experiment is still very good. Upon comparison with the origin spectrum it is also apparent that the amount by which all lines are split due to tunneling is substantially larger; the fit yielded a value of 1656.4 ± 1.1 MHz which corresponds to an increase of almost 50%. The molecular parameters resulting from this fit were added to Table 2.1.
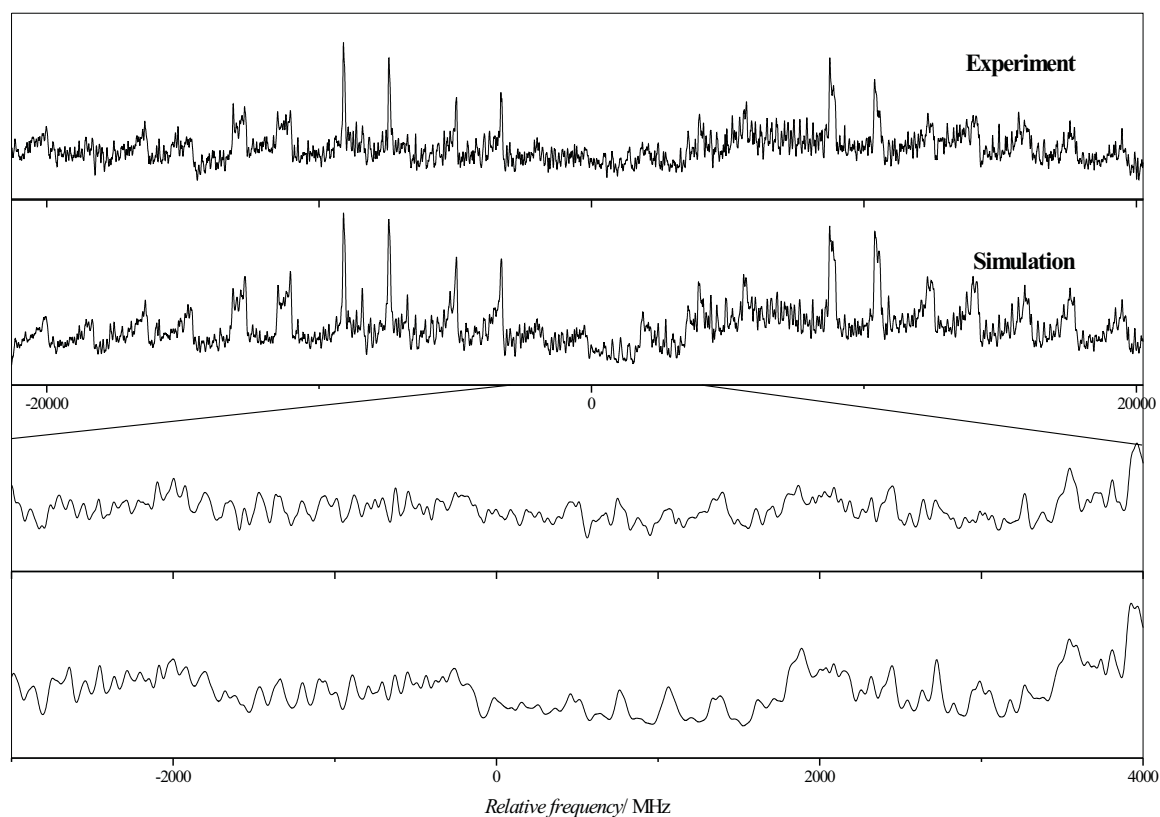
Figure 2.2: The vibronic band at 35781.091 cm^{-1}, around 57 cm^{-1} above the electronic origin of the benzoic acid d_0-d_0 dimer.

Table 2.1: Origins and molecular parameters for the benzoic acid dimer isotopologues determined from fits using evolutionary algorithms, as described in the text.

	d_0-d_0					
	This work	Ref. 40	Ref. 19	d_0-d_0 + 57 cm^{-1}	d_1-d_1	d_5-d_5
A''/MHz	1925.00(20)	1923(16)	1926.87(50)	1925.04(21)	1905.94(18)	1686.92(16)
B''/MHz	128.05(14)	127(8)	128.19(10)	128.08(14)	127.73(14)	118.91(14)
C''/MHz	120.14(14)	114(8)	120.27(10)	120.17(14)	119.79(14)	111.16(14)
A'/MHz	1908.95(16)	1908(16)	1910.70(50)	1920.48(17)	1890.16(15)	1672.95(13)
B'/MHz	127.53(14)	-	127.67(10)	127.57(14)	127.18(14)	118.42(14)
C'/MHz	119.63(14)	-	119.76(10)	119.64(14)	119.24(14)	110.68(14)
ΔA/MHz	-16.05(9)	-15(10)	-16.17(20)	-4.56(9)	-15.78(8)	-13.98(7)
ΔB/MHz	-0.52(12)	-	-0.52(1)	-0.52(12)	-0.55(12)	-0.48(12)
ΔC/MHz	-0.51(12)	-	-0.51(1)	-0.53(12)	-0.55(12)	-0.48(12)
Δ/MHz	1114.0(10)	1107(7)	1116(3)	1656.4(11)	< 45	1077.0(10)
Origin (cm^{-1})[a]	35723.786(1)	35723.82(5)	-	35781.091(1)	35737.416(1)	35874.324(1)

	d_0^*-d_1			d_1^*-d_0	d_0^*-d_5	d_5^*-d_0
A''/MHz	1915.76(32)			1915.76(17)	1798.21(14)	1798.21(15)
B''/MHz	127.91(15)			127.91(14)	123.42(14)	123.42(14)
C''/MHz	119.98(15)			119.98(14)	115.58(14)	115.58(14)
A'/MHz	1899.65(26)			1900.51(14)	1784.55(12)	1782.50(12)
B'/MHz	127.39(15)			127.33(14)	122.95(14)	122.90(14)
C'/MHz	119.50(15)			119.42(14)	115.11(14)	115.07(14)
ΔA/MHz	-16.11(16)			-15.25(10)	-13.66(6)	-15.72(7)
ΔB/MHz	-0.50(12)			-0.57(12)	-0.46(12)	-0.52(12)
ΔC/MHz	-0.50(12)			-0.56(12)	-0.48(12)	-0.51(12)
Δ/MHz	136.7(12)			98.9(11)	1137.0(10)	1116.9(11)
Origin (cm^{-1})[a]	35722.789(1)			35737.574(1)	35724.456(1)	35872.481(1)

[a] In the spectra possessing a splitting the origin of the redmost component is given

2.3.3   Determination of the cluster structure parameters

RICC2 optimizations of the S_0 state structure with C_1 and with C_{2h} symmetry restrictions imposed were performed using the TZVP basis sets. The results of both calculations were identical within the accuracy of the calculation, confirming the symmetry of the equilibrium structure. The rotational constants resulting from the constrained calculations are shown in Table 2.2 along with the experimental rotational constants from this study and the optimized geometry parameters. The agreement between the calulated and the experimental inertial parameters is very good, with the calculated constants differing from the measured ones by less than half a percent. Since the experimentally determined rotational constants are effective values rather than equilibium values the difference is ascribed to zero-point energy vibrational averaging effects and the calculated structure is assumed to be the best possible fit to the measurements. The S_1 state optimizations at the same level of theory result in rotational constants close to those of the ground state. The A constant is found to decrease by 16 MHz upon electronic excitation compared to a 19 MHz difference between the RICC2/TZVP calculations of the excited state and the electronic ground state.

The atomic numbering for the benzoic acid dimer used in the following discussion of the structural parameters of the monomers and the hydrogen bond parameters is given in Figure 2.3. The calculated geometry parameters for both benzoic acid moieties are equal for the ground state (C_{2h} symmetry) while they differ considerably for the electronically excited state, reflecting the localized excitation with a reduction of the symmetry to C_s. The electronically excited benzoic acid moiety (marked with asterisks in the bond definitions in Table 2.2) shows an increase of the average CC bond length from 139.4 pm in the ground state to 143.0 pm, which is typical for benzenoid aromatic compounds. The unexcited moiety of the electronically excited dimer has an average CC bond length of 139.6 pm, nearly the same value as in the ground state, confirming the localization of the excitation on one of the benzoic acid moieties. The decrease of the C_1C_7 bond length, indicating the quinoidal character in the S_1 state, is also found in other monosubtituted benzenes.
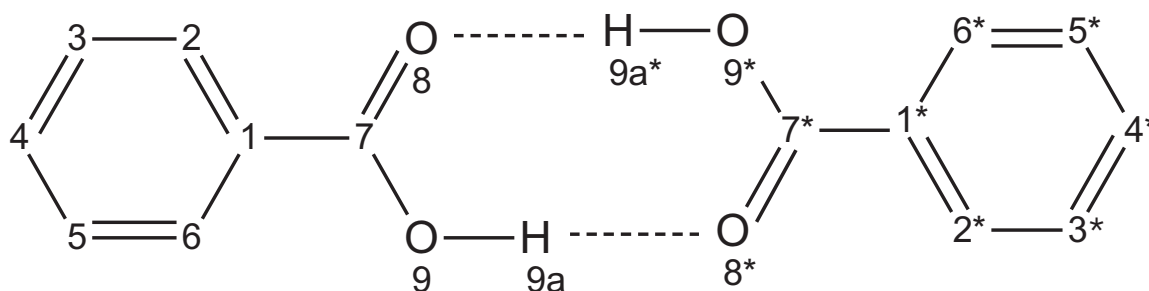
Figure 2.3: Atomic numbering of the benzoic acid dimer used in Table 2.2. The asterisks mark the electronically excited benzoic acid moiety.

The hydrogen bond geometry parameters show the same behavior: two equal O_9H_{9a} hydrogen bond lengths and equal $O_9H_{9a}O_8^*$ angles, which define the deviation from linearity of the hydrogen bonds in the electronic ground state, while both geometry parameters differ considerably in the excited state. The C-O-H$\cdots$O-C* hydrogen bond is considerably shorter than in the electronic ground state (-5.2 pm), while the

Table 2.2: Rotational constants and S_0 and S_1 state geometry parameters of the benzoic acid dimer calculated at the RICC2/TZVP level of theory. The atomic numbering refers to Figure 2.3. All bond lengths are given in pm, angles in degrees. Atoms marked with an asterisk belong to the electronically excited benzoic acid moiety.

	S_0			S_1	
	RICC2	crystal data[70]	Exp.[a]	RICC2	Exp.[a]
A''/MHz	1919	-	1925	1900	1909
B''/MHz	128	-	128	127	127
C''/MHz	120	-	120	119	120
C_1C_2	139.9	139.2	-	140.0	-
C_2C_3	139.2	140.1	-	139.3	-
C_3C_4	139.5	138.4	-	139.6	-
C_4C_5	139.6	137.9	-	139.6	-
C_5C_6	139.1	138.7	-	139.2	-
C_6C_1	139.9	139.0	-	140.0	-
C_1C_7	148.3	148.4	-	148.6	-
C_7O_8	124.0	126.3	-	124.2	-
C_7O_9	130.0	127.5	-	132.8	-
O_9H_{9a}	100.3	$\approx$100	-	100.2	-
$CH_{av.}$	108.3	-	-	108.4	-
$C_2C_1C_7$	121.3	118.8	-	121.3	-
$O_8C_7O_9$	123.8	123.2	-	124.0	-
$C_1C_7O_8$	122.2	120.2	-	121.9	-
$C_7O_9H_{9a}$	108.5	-	-	108.8	-
$C_1^*C_2^*$	139.9	139.2	-	143.4	-
$C_2^*C_3^*$	139.2	140.1	-	143.2	-
$C_3^*C_4^*$	139.5	138.4	-	141.9	-
$C_4^*C_5^*$	139.6	137.9	-	142.9	-
$C_5^*C_6^*$	139.1	138.7	-	143.1	-
$C_6^*C_1^*$	139.9	139.0	-	143.4	-
$C_1^*C_7^*$	148.3	148.4	-	144.3	-
$C_7^*O_8^*$	124.0	126.3	-	125.7	-
$C_7^*O_9^*$	130.0	133.1	-	134.5	-
$O_9^*H_{9a}^*$	100.3	$\approx$100	-	100.0	-
$C^*H_{av.}^*$	108.3	-	-	108.3	-
$C_2^*C_1^*C_7^*$	121.3	118.8	-	122.8	-
$O_8^*C_7^*O_9^*$	123.8	123.2	-	123.6	-
$C_1^*C_7^*O_1^*$	122.2	120.2	-	122.2	-
$C_7^*O_9^*H_{9a}^*$	108.5	-	-	108.2	-
$H_{9a}O_8^*$	165.4	$\approx$160	-	160.2	-
$O_8H_{9a}^*$	165.4	$\approx$160	-	167.2	-
$O_8O_9^*$	265.7	263.3	-	267.2	-
$O_9O_8^*$	265.7	263.3	-	260.4	-
$O_9H_{9a}O_8^*$	179.0	-	-	177.5	-
$O_9^*H_{9a}^*O_8$	179.0	-	-	179.1	-

[a] Experimental values from this study

For exact values and accuracies cf. Table 2.1

*C-O-H$\cdots$O-C bond is longer by 1.8 pm. These opposite changes of the hydrogen bond lengths, which are founded in the decrease of OH acidity upon electronic excitation, result in an in-plane tilting of the monomer moieties in the excited state. The amount by which the structure is bent cannot be determined in the same way as was done by Remmers *et al.*[40] since they assumed both monomer geometries were retained in the dimer, which is not the case and leaves their bending angle ill-defined. When instead the bending angle is defined as C_4-CM-C_4^*, where CM stands for the dimer center of mass, a value of 0.7 ± 0.2 ° results. Since the length decrease of the shortened hydrogen bond is larger than the length increase of the elongated one these results are consistent with the reduction in the average carboxy O$\cdots$O distance found in earlier work.[34,37]

2.3.4   Determination of the center of mass distance

An easy approach to the change of the cluster structure upon electronic excitation can be made using the center of mass (COM) distance of the monomer moieties in the cluster as has been shown by Connell *et al.*[71] The COM distance of two monomer moieties in a dimer is given by:

$$R = \sqrt{\frac{\sum_g I_g^{Dimer} - \sum_g I_g^{Monomer1} - \sum_g I_g^{Monomer2}}{2\mu}}, \tag{2.1}$$

where μ is the reduced mass of the two moieties, and the I_g are the respective moments of inertia, described by their superscripts, which are calculated from experimentally determined rotational constants. The COM distances for the d_0-d_0 and the d_1-d_1 clusters in the ground state were calculated using the monomer rotational constants, taken from the microwave work of Onda *et al.*[72] for both moieties. The difference between the COM distances of d_0-d_0 and d_1-d_1 can be traced back to the different vibrational averaging in these isotopologues.

While the determination of the COM distance in the electronic ground state is conceptually easy, two problems arise for the electronically excited state: first, the rotational constants of the excited state of the monomer are not known. Second, it is not known *a priori* whether the excitation is local or delocalized over both moieties. In the first case different rotational constants have to be used in equation 2.1 for Monomer1 and Monomer2. One of the monomers would then have the rotational constants of benzoic acid in the ground state, the other the rotational constants of the electronically excited state. Since these rotational constants are not available the ground state rotational constants of both monomers were used for a rough model, which in the following will be called model 1.

Because it was concluded in the previous section that the electronic excitation is localized, a more accurate COM distance can be derived when the rotational constants of the monomer excited state are used. These can be obtained by calculating the structure of the benzoic acid monomer using density functional theory with the B3-LYP functional for the ground state and with time dependent DFT for the excited state. The difference between the two sets of rotational constants closely matches the change of the rotational constants upon electronic excitation, while the absolute values

are less reliable. The differences between the calculated rotational constants from the DFT and TDDFT calculations were therefore added to the microwave rotational constants to get the inertial parameters for the excited monomer moiety, and these were used in a more accurate model. This is called model 2.

Table 2.3 compares the COM distances in the ground and electronically excited states of the benzoic acid dimer for both monomer models, described above. For both isotopologues and independent of the model used an increase in the COM distance is found , showing a decrease of the hydrogen bond strength upon electronic excitation.

Table 2.3: Center of mass distance (in pm) of the d_0-d_0 and the d_1-d_1 isotopologues of the benzoic acid dimer in the ground and electronically excited state. For the description of model 1 and model 2 see text.

		d_0-d_0	d_1-d_1
S_0		712.6	708.9
S_1	model 1	714.6	713.3
S_1	model 2	713.1	711.7
Δ	model 1	2.0	4.4
Δ	model 2	0.5	2.8

2.3.5 Symmetry

Both the $S_1 \leftarrow S_0$ spectrum and the vibronic band 57 cm^{-1} above it are b-type spectra consisting of 2 components. Interestingly, the separation between these components is larger in the vibronic spectrum than in the origin spectrum. As can be seen in Figure 2.4 there are three possible ways to combine these two observations: the ground state splitting is very small (a), the S_1 state splitting is very small (b) or both are appreciable (c). Since it is expected from theory that the splitting in the electronically excited state is smaller than that in the ground state due to the weakening of one of the hydrogen bonds (see e.g. Smedarchina *et al.*)[31] we hold the first option for unlikely and will therefore not explore it further. Turning our attention to the other two options the first thing to note is that some of the arrows drawn in figures b and c are not unique; the relative sizes of the tunneling splittings are equally unknown. However, it is clear that without any selection rules restricting the possibilities the vibronic band would consist of 4 components, and in case c the same would hold for the origin transition. This is clearly not what is observed, meaning a closer look at the symmetry of the dimer system is warranted. For a large part the group theory for this system is the same as for the formic acid dimer, which has been described in detail by Madeja *et al.*[27] We will therefore focus on the main differences and conclusions here; more information can be found in their article. Additionally, case b will be considered to be the limiting case for the energy level ordering shown in Figure 2.4c and will no longer be considered separately.

As was shown in section 2.3.3 the ground state structure is of C_{2h} symmetry and if a synchronous tunneling motion is assumed the transition state is of D_{2h} symmetry, which means the ground state has to be described using the molecular symmetry group G_8. For the electronically excited state, however, it was already concluded above that
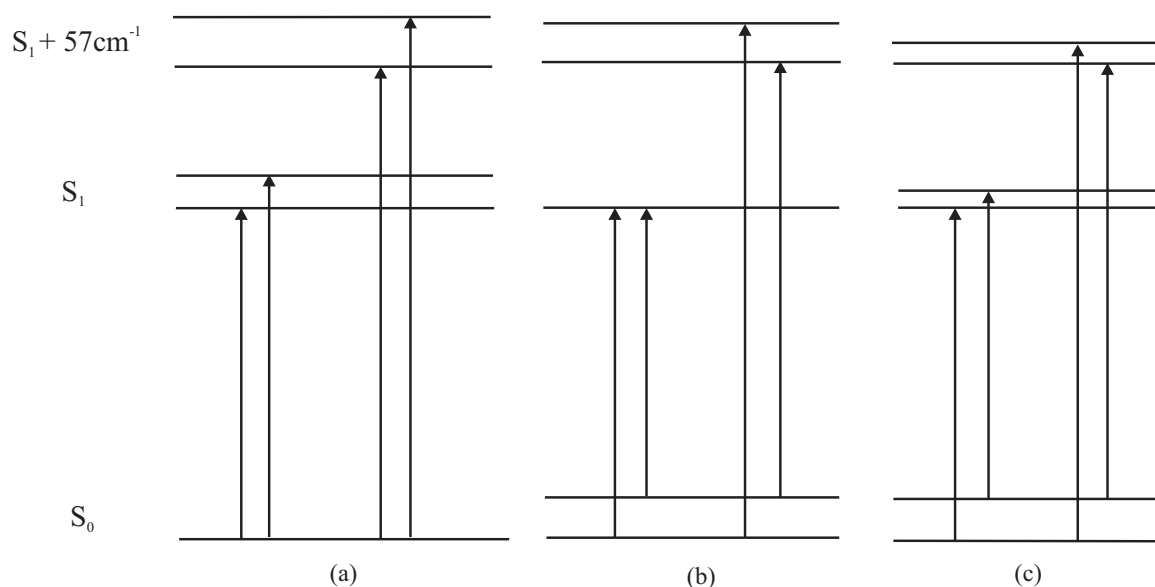
Figure 2.4: Three possible energy level schemes for explaining the observed $S_1 \leftarrow$ S_0 and $S_1 + 57\mathrm{cm}^{-1} \leftarrow S_0$ spectra.

the electronic excitation is localized on one monomer unit. This immediately lowers the symmetry to C_s with a C_{2v} transition state (with the A-axis as the C_2-axis) so that the excited state has to be described using G_4. The energy level diagram and allowed transitions that result for the origin and the seven lowest frequency vibrations (see section 2.3.6) are shown in Figure 2.5. Note that all levels have two symmetry labels due to the unresolved K-type doubling in this system.

If in addition to the localization of the electronic excitation the excited state has a bent structure then the system has $C_s(\mathrm{M})$ symmetry (isomorphic with C_s) and all energy level labels are transformed into A'/A''. This means all transitions would become possible again, in contradiction with observations. Clearly the bending angle for the excited state geometry that was deduced in section 2.3.3 is small enough to approximate the system as G_4 symmetric.

It should be noted that the assumption of G_4 symmetry also has an effect on the intensity ratios between different transitions. The effect, however, is small: when the K-type doubling cannot be resolved (as in our case) a ratio between $\Delta K_a \Delta K_c$ (even/even) and (even/odd) to (odd/odd) and (odd/even) transitions of 31:33 results. This effect is further diminished by the crowdedness of the spectrum, mixing different transitions under each apparent lineshape, and leads to our inability to decide on the correctness of this assumption based on nuclear statistics.

2.3.6   Vibronic band assignment

For a correct assignment of the 57 cm^{-1} band the calculated frequencies for the vibrations indicated in Figure 2.5 will now be needed; they are given for the S_0 state in Table 2.4.

It is known from earlier work by Poeltl *et al.*[49] that for this particular vibration the excited state frequency is practically the same as that in the ground state, which allows the use of these ground state frequencies for the assignment. They were derived
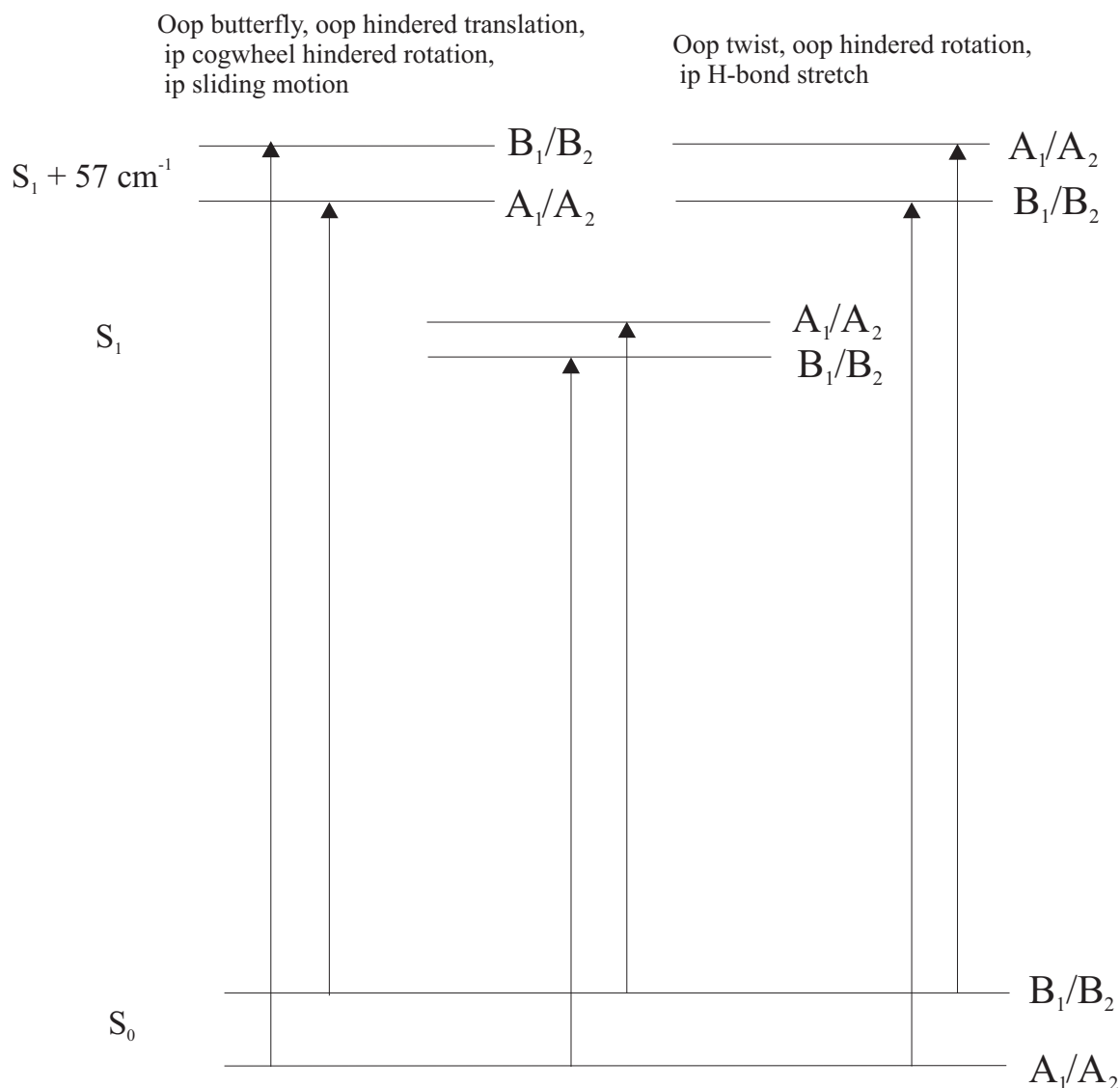
Figure 2.5: The energy level ordering and allowed transitions for the electronic origin and seven lowest frequency vibrations under C_{2v} symmetry; vibrational nomenclature after Florio *et al.*[55] Out-of-plane vibrations are designated as 'oop', in-plane vibrations as 'ip'.

under C_{2h} symmetry and the corresponding symmetry labels are given. However, as was described in the preceding section, due to the feasibility of the tunneling motion and the localization of electronic excitation the G_4 symmetry group, which is isomorphic to C_{2v}, should be used to describe possible transitions. For this reason G_4 symmetry labels were also added. The last three columns list the calculated changes in rotational constants for these vibrations in the harmonic approximation.

Given the fact that the splitting observed in the vibronic band spectrum is larger than that in the origin spectrum (1656.4 vs 1114.0 MHz) it is clear that an assignment to a vibration having the same selection rules as the origin transition (those on the right hand side in Figure 2.5) is only possible if the vibration itself decreases the tunneling rate. Since the out-of-plane twisting motion and the out-of-plane hindered rotation leave the hydrogen bonding network practically unaffected these are ruled

Table 2.4: RICC2/TZVP calculated frequencies for the seven lowest S_0 state vibrations of the d_0-d_0 and d_5-d_5 benzoic acid dimer including their symmetry labels under the C_{2h} point group and the G_4 molecular symmetry group. Also given are the calculated changes in rotational constants they lead to in the harmonic approximation.

Vibration	Frequency (cm^{-1})		Symmetry		$\Delta g; g = A, B, C$/MHz		
	d_0-d_0	d_5-d_5	C_{2h}	G_4	ΔA	ΔB	ΔC
Observed	57.31	-	-	-	11.49	0.00	-0.02
Oop butterfly	58.1	56.5	a_u	B_1	-14.26	-0.06	0.00
Oop hindered translation	88.6	86.7	b_g	B_1	-18.17	-0.08	0.00
Ip cogwheel hindered rotation	97.9	93.5	b_u	B_2	-8.93	-0.01	-0.05
Oop twist	110.9	101.4	a_u	A_2	-7.78	-0.03	0.00
Ip H-bond stretch	116.8	113.8	a_g	A_1	-9.57	5.40	4.69
Ip sliding motion	134.1	129.5	a_g	B_2	2.09	1.58	1.40
Oop hindered rotation	171.7	171.2	b_g	A_2	-13.33	-0.06	0.00

out. The in-plane H-bond stretch is expected to increase the tunneling rate, and the motion itself would lead to a change in the B and C rotational constants. Since this contradicts the measurements the in-plane H-bond stretching motion was also excluded as a possibility, forcing us to conclude that the selection rules for the 57 cm^{-1} vibronic band have to be reversed.

Taking a look at the four vibrations listed on the left hand side of Figure 2.5 the same argument excludes the in-plane sliding motion as it is expected to have an effect on the B and C rotational constants as well as A, contrary to observations. This leaves us with only three possible assignments: the out-of-plane butterfly motion, the out-of-plane hindered translation and the in-plane cogwheel hindered rotation. Without additional information to discriminate between these modes we opt to trust the calculated frequencies and assign the 57 cm^{-1} band as the out-of-plane butterfly motion, in excellent agreement with calculations (58 cm^{-1}). It also agrees with the observation that the frequency is virtually unchanged in the d_5-d_5 dimer,[48] and with the assignment made in a later publication by Poeltl and McVey.[49] Unfortunately however, the effect this vibration has on the A rotational constant does not agree with the measurements. Indeed, even the sign of the predicted change is wrong. Although the vibrational effects on the rotational constants were calculated in the harmonic approximation and it is well known that the vibrations in the benzoic acid dimer are highly anharmonic[55] it is inferred that this vibration must be accompanied by a structural change that is not predicted by the calculations.

2.3.7 Splittings

Interestingly, the out-of-plane butterfly mode involves practically no motion of the hydrogen bonding network. If it is assumed that this means the effect on the tunneling rate is negligible the sizes of the S_0 and S_1 state tunneling splittings can be deduced. As can be seen in Figure 2.5 the splitting observed in the vibronic band spectrum would then be the sum of the S_0 and S_1 tunneling splittings whereas the separation between the two components in the origin spectrum would equal the difference. If

now, like in section 2.3.5, the S_0 splitting is taken to be larger than the S_1 splitting it immediately follows that $\Delta S_0 = 1385.2 \pm 0.7$ MHz and $\Delta S_1 = 271.2 \pm 0.7$ MHz. In the case of a pure, coherent tunneling motion in a simple symmetric double minimum potential well the effective potential barrier V_{eff} can now be calculated in the WKB approximation.[73] The imaginary frequency at the top of the barrier (ω_i) and the corresponding ground state frequency (ω_F) were deduced from a normal mode analysis of the S_0 transition state and ground state RICC2 structures, respectively. Using the resulting values of $\omega_i = 1122$ cm^{-1} and $\omega_F = 3167$ cm^{-1} an S_0 state potential barrier of 6224 cm^{-1} (7.45 kJ/mol) is found. Because no reliable S_1 state transition frequency was calculated the same frequencies are assumed to calculate the S_1 state potential barrier, which results in a value of 6672 cm^{-1} (7.99 kJ/mol).

Since the approximation used here is quite crude these barrier height are not expected to be very accurate, even though the S_0 state barrier is quite close to the 6.93 kJ/mol found in the most extensive calculation done until now.[31] However, the ratio of the S_1 to S_0 barrier heights is expected to be relatively accurate. Thus, it can be concluded that the barrier height increases by about 7.2 % upon electronic excitation.

The fact that the splitting observed in the 57 cm^{-1} band spectrum can be interpreted to arise from proton tunneling while no further splitting has been observed leads to the conclusion that an exciton splitting does not show up in the spectra. This leads to an upper limit of 45 MHz for the exciton splitting and confirms the conclusion from earlier work that excitation transfer only becomes important at higher excess energies.[49]

2.4   Conclusions

From a measurement of the rotationally resolved spectra of five different isotopologues two separate origins were observed for each of the mixed dimers. Together with the observation that the ground state rotational constants are the same for both of these spectra this provides unequivocal proof that the electronic excitation is localized on one of the monomer units. From the structural analysis it can be deduced that this leads to an asymmetry in the hydrogen bonding network geometry and a lowering of the dimer symmetry to C_s. An increase in the center of mass distance between both monomer moieties was also found, from which it is concluded that the hydrogen bond strength is decreased upon electronic excitation. Analysis of a vibronic band located 57 cm^{-1} above the electronic origin leads us to the conclusion that it should be assigned as the out-of-plane butterfly motion and allows the deduction of the S_0 and S_1 state splittings separately. From the resulting splittings, $\Delta S_0 = 1385.2 \pm 0.7$ MHz and $\Delta S_1 = 271.2 \pm 0.7$ MHz, it can be concluded that the barrier height in the S_1 state is 7.2 % larger than that in the S_0 state. No evidence for excitation transfer was found.

The structure of phenol-Ar_n $(n = 1, 2)$ clusters in their S_0 and S_1 states

The stuctures of the van der Waals bonded complexes of phenol with one and two argon atoms have been determined using rotationally resolved electronic spectroscopy. The experimentally determined structural parameters were compared to the results of quantum chemical calculations that are capable of properly describing dispersive interactions in the clusters. It was found that both complexes have van der Waals bonded configurations, with the two argon complex adopting a symmetric (1|1) structure. REMPI spectroscopy was used to measure intermolecular vibrational frequencies and Franck-Condon simulations were performed to check the structure of the two argon cluster. These were found to be in excellent agreement with the (1|1) configuration.

3.1 Introduction

Intermolecular interactions of aromatic molecules are vital for chemical and biological recognition.[74] A detailed understanding of these interactions at the molecular level requires accurate knowledge of the intermolecular potential energy surface. Essential parameters of such a surface include the interaction energy and the geometry of the global minimum, as well as the occurrence of less stable local minima. The fruitful interplay of high-resolution spectroscopy of isolated clusters in molecular beams and high-level quantum chemical calculations provides the most direct access to these potential parameters.[18,75–81] Clusters of phenol with neutral ligands, denoted phenol-L_n, are attractive model systems to investigate the competition of two different fundamental types of intermolecular force, namely hydrogen bonding to the acidic OH group (H-bond) and van der Waals bonding (stacking) to the highly polarizable π electron system of the aromatic ring (π-bond, van der Waals bond). It turns out that the relative interaction strengths of both binding motifs strongly depend on the type of

ligand (L), the degree of solvation (n), and the degree of electronic excitation or ionization. Hence, a plethora of spectroscopic and theoretical studies have been carried out on phenol-bearing clusters in order to determine the preference for stacking or hydrogen bonding interactions.

The present work reports high-resolution electronic spectra of phenol-Ar_n clusters with $n=1$ and 2 in a molecular beam expansion, along with quantum chemical calculations. The analysis of the $S_1 \leftarrow S_0$ spectra obtained at the level of rotational resolution provide for the first time clear-cut information about the geometry and preferential binding motif of these prototype clusters, which are model systems for an acidic polar molecule interacting with a nonpolar solvent. Despite numerous spectroscopic studies on phenol-Ar_n clusters reported in the past, the structural binding motif of this simple system has not been identified unambiguously for the neutral electronic states. An analysis of vibrational frequencies from new REMPI spectra of the phenol-Ar_n ($n = 1 - 3$) clusters will corroborate the results.

In the following, the present knowledge about phenol-Ar_n will be briefly reviewed. In 1985, initial spectroscopic data about phenol-Ar_n ($n = 0 - 2$) came from one-color resonance-enhanced multiphoton ionization (REMPI) spectra of the $S_1 \leftarrow S_0$ transition and two-color photoionization efficiency (PIE) spectra of the cation ground state (D_0) recorded via the S_1 state origins reported by Gonohe *et al.*[82] On the basis of nearly additive shifts in the $S_1 \leftarrow S_0$ transition energies (-33 and -68 cm^{-1}) and ionization potentials (-152 and -297 cm^{-1}) upon complexation with one and two argon atoms, the authors concluded that both argon ligands are π-bonded to phenol on opposite sides of the aromatic ring, denoted (1|0) and (1|1) structure.[82] The intermolecular vibrational structures observed in the $S_1 \leftarrow S_0$ electronic spectra of phenol-Ar[83,84] and phenol-Ar_2[85] have subsequently been assigned assuming π-bonded (1|0) and (1|1) structures, respectively.

Almost negligible complexation-induced frequency shifts of the O$-$H stretch (ν_{OH}) and other skeletal vibrations in the S_0 state of phenol-Ar observed via stimulated Raman[86] and IR dip spectroscopy[87,88] have been indicative for a π-bonded (1|0) geometry for the $n = 1$ complex. In addition, high level quantum chemical calculations of the potential energy surface in the S_0 state yield a π-bonded global minimum, and it is unclear at present whether the H-bonded structure is a shallow local minimum or a transition state.[89–92] Comparison of rotational constants derived from a rotational band contour fit of the S_1 origin spectrum with ab initio rotational constants obtained at the MP2/6-31G(d,p) level also support a π-bonded (1|0) geometry for $n = 1$.[93] Meerts *et al.* presented the fully rotationally resolved electronic spectrum of the d$_1$-phenol-Ar$_1$ cluster.[18] The rotational constants of the S_0 state are close to those of the S_1 state, implying similar π-bonded geometries in both electronic states. Mass-analyzed threshold ionization (MATI) and zero-kinetic-energy photoelectron (ZEKE) spectroscopy have been employed to derive the binding energies of π-bonded phenol-Ar in the D_0, S_1, and S_0 state as 535±3, 397±13 and 364±13 cm^{-1}, respectively, and to measure and assign the intermolecular vibrational modes in the D_0 cation state.[94–97] The intermolecular frequencies are consistent with the π-bonded phenol-Ar geometry. Similarly, the ν_{OH} frequency of phenol$^+$-Ar derived from IR photodissociation of the cation dimer generated by REMPI is compatible only with a π-bonded isomer.[87,98]

Until recently, all spectroscopic studies indicated that phenol$^{(+)}$-Ar has a π-bonded equilibrium structure in the S_0, S_1, and D_0 states and no signature of an H-bonded

phenol$^{(+)}$-Ar isomer had been detected. In 2000, however, the IR photodissociation spectrum of phenol$^+$-Ar generated in an electron impact (EI) ion source clearly demonstrated that the H-bonded isomer is the global minimum on the potential energy surface of the cation cluster, with a characteristic ν_{OH} frequency strongly red-shifted from isolated phenol$^+$ by H-bonding.[99–103] This result was confirmed by quantum chemical calculations, which predict the H-bonded isomer as global minimum in the D$_0$ state, whereas the π-bonded structure is only a local minimum.[92,100,104] The reason why the most stable H-bonded isomer of phenol$^+$-Ar had completely escaped previous spectroscopic detection (MATI, PIE, ZEKE, REMPI-IR),[82,93,95–98] arises from the fact that the phenol$^+$-Ar cation in the D$_0$ state had been prepared by REMPI of the neutral π-bonded precursor, which is governed by the restrictions of minimal geometry changes imposed by the Franck-Condon principle. In contrast, the EI cluster ion source predominantly produces the most stable isomer of a given phenol$^+$-Ar$_n$ cation cluster, because the reaction sequence begins with EI ionization of the phenol monomer, which is followed by threebody cluster aggregation reactions.[101,103] As the H-bond in phenol$^+$-Ar is more stable than the π-bond, the energetically most favorable isomers of larger phenol$^+$-Ar$_n$ clusters (n > 1) have one H-bonded ligand and (n-1) π-bonded ones.[101]

The ionization-induced $\pi \rightarrow$ H switch in the preferred phenol-Ar binding motif has recently been probed by time-resolved IR spectroscopy of the phenol$^+$-Ar$_2$ complex prepared by REMPI.[105,106] These studies revealed that after ionization of π-bonded phenol-Ar$_2$, one Ar ligand isomerizes from the π-bonded site toward the H-bonded site on a timescale of several ps. However, it was noted that for a full understanding of this dynamic process, one must know whether the neutral phenol-Ar$_2$ precursor complex has a symmetric structure with one Ar above and the other symmetrically below the aromatic plane (in the following denoted by (1|1)) or a structure with both Ar atoms at the same side of the aromatic ring (in the following denoted by (2|0)). Unfortunately, no reliable calculations are available for the potential energy surface of phenol$^{(+)}$-Ar$_2$. Moreover, spectroscopic evidence for the geometric structure of neutral phenol-Ar$_2$ is scarce and not unambiguous as it relies on vibrationally resolved spectra only.[82,85,97,107] Recent hole-burning spectra of phenol-Ar$_n$ with $n = 1$ and 2 demonstrated that all spectral features observed in the S$_1 \leftarrow$ S$_0$ REMPI spectra indeed arise from single isomers in the molecular beam expansion, which have been assigned to π-bonded structures for both $n = 1$ and $n = 2$. The refined analysis of the intermolecular vibrational structure observed for phenol-Ar$_2$ was, however, compatible with both a (1|1) and a (2|0) structure. The main purpose of the present work is to provide the definitive answer to the question of the geometry of the phenol-Ar$_2$ trimer.

3.2 Methods

3.2.1 Experimental Procedures

The experimental setup for rotationally resolved laser induced fluorescence spectroscopy is described in detail elsewhere.[58] Briefly, it consists of a ring dye laser (Coherent 899-21) operated with Rhodamine 110, pumped with 7 W of the frequency doubled output of a diode pumped Yb:YAG disc laser (ELS Versadisk). About 600-

700 mW of the fundamental dye laser output is coupled into an external folded ring cavity (Spectra Physics) for second harmonic generation. The typical output power is 20 mW and is constant during each experiment.

The molecular beam is formed by expanding phenol, heated to 365 K and seeded in 600 mbar of argon, through a 230 μm hole into the vacuum. The molecular beam machine consists of three differentially pumped vacuum chambers that are connected by two skimmers (1 mm and 3 mm diameter, respectively) in order to reduce the Doppler width to 25 MHz. The molecular beam is crossed at right angles with the laser beam in the third chamber, 360 mm downstream of the nozzle. The resulting fluorescence is collected perpendicular to the plane defined by the laser and the molecular beam by an imaging optics setup consisting of a concave mirror and two plano-convex lenses. The fluorescence is detected by a UV enhanced photo-multiplier tube whose output is recorded by a PC based photon counter IO card. The relative frequency is determined with a quasi confocal Fabry-Perot interferometer. The absolute frequency was determined by recording the iodine absorption spectrum and comparison of the transitions with tabulated lines.[108]

The experimental apparatus for resonance enhanced multiphoton ionization (REMPI) spectroscopy has been described in detail previously.[109] Phenol-Ar$_n$ clusters were produced in a skimmed supersonic expansion by passing argon gas over a heated phenol sample (330-350 K) in an internal sample holder located directly behind the valve. The pressure of argon gas can be varied up to 8 bar in order to optimize the production of phenol-Ar$_n$ clusters. The rotational temperature of the molecules is approximately 4 K after the expansion.[93] The molecular beam interacts with the counter-propagating, frequency-doubled output of two Nd:YAG pumped dye lasers (Radiant Dyes Narrowscan) using Coumarin 153 for excitation, whilst a mixture of Sulforhodamine B and DCM was used for the ionization laser to achieve a wide tuning range. The lasers were calibrated (± 0.02 cm^{-1}) with reference to simultaneously recorded iodine absorption spectra, corrected from air to vacuum.

Phenol was purchased from Riedel-de Haën (p.A.) and was used without further purification. D-phenol was produced by refluxing phenol with an excess of D$_2$O and subsequent removal of solvent.

3.2.2   Computational Methods

Quantum chemical calculations

Structure optimizations were performed employing the valence triple zeta basis set with polarization functions (d,p) from the Turbomole library.[59,60] The equilibrium geometries of the electronic ground and the lowest excited singlet states were optimized at the CC2 level within the resolution-of-the-identity approximation.[61,62] Ground state vibrational frequencies have been calculated through analytical second derivatives using the aoforce module[110,111] implemented in Turbomole Version 5.8. Excited state vibrational frequencies were calculated using numerical differentiation of analytic gradients using the NumForce script of Turbomole Version 5.8.

The singlet state energies, wavefunctions, and transition dipole moments were calculated using the combined density functional theory/multi-reference configuration interaction (DFT/MRCI) method by Grimme and Waletzke.[63] The configuration state

functions (CSFs) in the MRCI expansion are constructed from Kohn-Sham (KS) orbitals, optimized for the dominant closed shell determinant of the electronic ground state employing the BH-LYP[64,65] functional. All valence electrons were correlated in the MRCI runs and the eigenvalues and eigenvectors of the lowest singlet state were determined. The initial set of reference configuration state functions was generated automatically in a complete active space type procedure (including all single and double excitations from the five highest occupied molecular orbitals in the KS determinant to the five lowest virtual orbitals) and was then iteratively improved. The MRCI expansion was kept moderate by extensive configuration selection. The selection of the most important CSFs is based on an energy gap criterion as described by Grimme and Waletzke.[63] Only those configurations were taken into account whose energy did not exceed a certain cutoff energy. The energy of a given configuration was estimated from orbital energies within the selection procedure. The cutoff energy was given by the energy of the highest desired root as calculated for the reference space plus a cutoff parameter $\delta E_{sel} = 1.0 \mathrm{E_H}$. This choice has been shown to yield nearly converged results.[63]

Franck-Condon simulations

The change of a molecular geometry on electronic excitation can be determined from the intensities of absorption or emission bands using the Franck-Condon (FC) principle. According to the FC principle the relative intensity of a vibronic band depends on the overlap integral of the vibrational wave functions in both electronic states, which is determined by the relative shift of the two potential energy curves connected by the vibronic transition along the normal coordinates of both states and the vibrations involved. The program FCFit[112] determines the structural changes on electronic excitation from the experimentally determined intensity pattern. Simultaneously, the changes of the rotational constants are used in the fit to assess the geometry change on excitation. The program was used to fit the structural change using only the changes in rotational constants, determine the FC factors and from those the absorption spectrum using the Hessians for ground and excited state from the RICC2/TZVP calculations.

Evolutionary strategies

The rotationally resolved electronic spectra were fit to an asymmetric rigid rotor Hamiltonian with the help of Evolutionary Strategies (ES). Contrary to most previous applications of genetic algorithm techniques[113–115] in the evaluation of molecular parameters from rotationally resolved electronic spectra[17–19,116] a different evolutionary strategy with mutative step size control was used in the present work. Mutative step-size control adapts the speed at which the parameter space is explored with each optimization step. It tends to work well for the adaptation of a global step-size but tends to fail when it comes to the step size of each individual parameter due to several disruptive effects.[22] The DR2 Algorithm used here[20] is aimed to accumulate information about the correlation or anti-correlation of past mutation vectors that connect trial solutions in order to tackle this problem. The effectiveness of this approach for spectral analysis has been shown recently.[117]

3.3   Results and Discussion

3.3.1   REMPI spectra of phenol-Ar$_{1-3}$

REMPI spectra of the phenol-Ar$_n$ ($n = 1 - 3$) clusters are shown in Fig. 3.1. Spectroscopic results are in agreement with previous studies[95,97] but show considerable improvement in signal-to-noise ratio.

In the REMPI spectra of the phenol-Ar$_1$ cluster (Fig. 3.1a), the most intense feature, the S$_1$ band origin, appears at 36316.4 ± 0.5 cm^{-1}, in very good agreement with the previous value of 36316 ± 0.5 cm^{-1}.[95,97] The position of the origin transition represents a red-shift of 33 cm^{-1} with respect to the S$_1$ origin of the phenol monomer at 36348.7 cm^{-1}.[24] The spectrum also exhibits a number of vdW vibrational modes at 23, 42 and 53 cm^{-1} above the band origin. They have been previously assigned as the bending mode b$_x$, its overtone, 2b$_x$, and the intermolecular stretch s$_z$.[93]

The most prominent spectral feature in the phenol-Ar$_2$ spectrum (Fig. 3.1b) at 36282.1 ± 0.5 cm^{-1} is assigned to the S$_1 \leftarrow$ S$_0$ origin. Relative to the phenol-Ar$_1$ band origin, this peak is red-shifted by 34 cm^{-1}, suggesting that the argon atom solvates the phenol molecule at a similar binding site to that in phenol-Ar$_1$. In a previous study[107] several smaller visible features in the spectrum were assigned to a progression in an intermolecular bending vibration (b$_x$, 2b$_x$ and 3b$_x$ at 14, 27 and 39 cm^{-1}) and excitation of the intermolecular stretch (s$_z'$ at 36 cm^{-1}). It was argued that this vibronic assignment is not unique and an asymmetric (2|0) structure cannot be excluded for the phenol-Ar$_2$ cluster.

Fig 3.1c displays the phenol-Ar$_3$ spectrum in which the most intense feature appears at 36373.8 ± 0.5 cm^{-1} and is assigned to the S$_1 \leftarrow$ S$_0$ origin. The origin transition is therefore blue-shifted by 25 cm^{-1} relative to the phenol S$_1$0^{0}band. A similar trend was observed in the fluorobenzene-Ar$_3$ system and attributed to the third argon atom adopting a bonding position adjacent to an above-ring argon atom.[118] A progression of peaks located at 23 and 44 cm^{-1} is assigned to vibrational quanta in the b$_x$ bend. The intermolecular stretch mode s$_z$ also can be assigned to the peak at 51 cm^{-1}.

3.3.2   Rotationally resolved electronic spectrum of phenol-Ar$_1$

The rotationally resolved electronic spectrum of the electronic origin of the phenol-Ar$_1$ cluster at 36315.05 cm^{-1} is shown in Figure 3.2. It is a c-type spectrum which is dominated by a strong central Q-branch, shown in an extended view in the lower trace of Figure 3.2. Since no a-type or b-type transitions could be incorporated into the fit unambiguously, the final fit was made to a pure c-type asymmetric rotor Hamiltonian. The same is true for the other high-resolution spectra discussed below.

Close agreement between the experimental spectrum and the simulation is obtained. The parameters deduced from this fit, listed in Table 3.1, are the rotational constants in the S$_0$ state (A, B, C), the change in rotational constants on electronic excitation ($\Delta(A, B, C)$), the frequency of the S$_1 \leftarrow$ S$_0$ origin transition, the direction of the transition dipole moment with respect to the system's main inertial axes (expressed in the angles ϕ and θ)[19] and the Lorentz width of each rovibronic transition
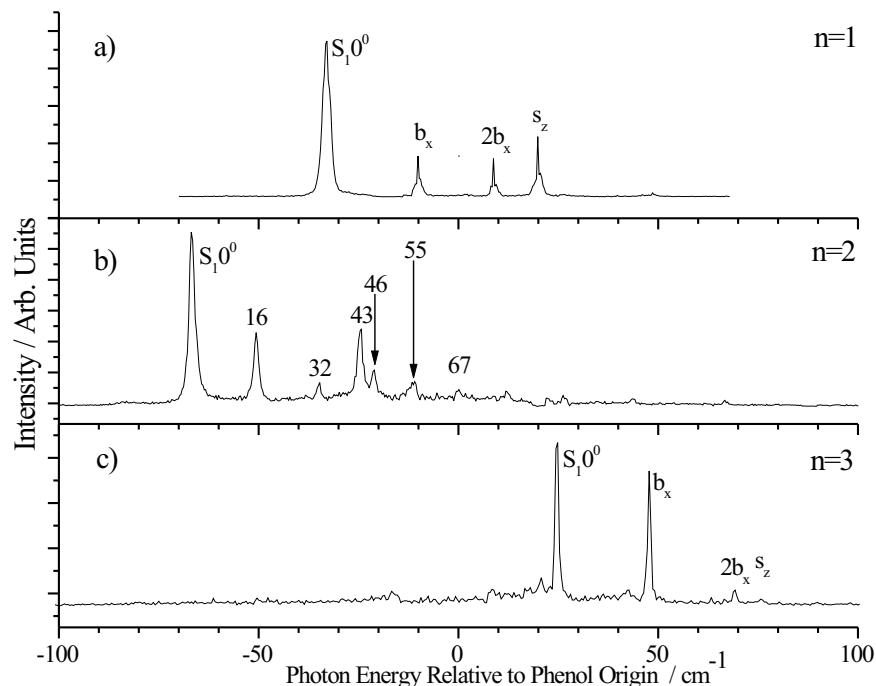
Figure 3.1: Two-colour $(1 + 1')$ $S_1 \leftarrow S_0$ REMPI excitation spectra of phenol-Ar_n ($n = 1 - 3$). The spectra were recorded with the probe laser set to 32210 cm^{-1}. Assignments of intermolecular modes are included for the $n = 1$ and $n = 3$ complexes. The spectra have been plotted relative to the phenol monomer $S_1 \leftarrow$ S_0 origin at 36348.71 cm^{-1}. The numbers in trace b (phenol-Ar_2) refer to the vibrational energy (in cm^{-1}) relative to the origin of phenol-Ar_2 at 36280.94 cm^{-1}.

(see section 3.3.7). The temperature of the molecular beam was described using a two temperature model[19,119] with $T_1 = 2.1$ K, $T_2 = 6.5$ K and a relative weight factor of 0.01.

The second isotopologue which has been investigated is the 7D-phenol-Ar_1 cluster, which has its electronic origin at 36312.74 cm^{-1}. The linewidth of the rovibronic transitions in the deuterated cluster is considerably smaller than that of the undeuterated cluster, as is the case in the bare monomer. A comparison of the molecular parameters obtained from the ES fits of the phenol-Ar_1 and 7D-phenol-Ar_1 spectra with the results of quantum chemical calculations is given in Table 3.1.

3.3.3 Rotationally resolved electronic spectrum of phenol-Ar_2

Figure 3.3 shows the rotationally resolved electronic spectrum of the phenol-Ar_2 origin at 36280.94 cm^{-1}. At 36278.62 cm^{-1} the origin of its hydroxy deuterated isotopologue is found, depicted in Figure 3.4. Also displayed are the simulations using the best fit parameters from Table 3.2. Just like in the $n = 1$ cluster the width of the individual transitions is indicative of an excited state lifetime that is considerably shorter than that in the monomer.

Table 3.2 lists the molecular parameters obtained from ES fits of the phenol-Ar_2 and 7D-phenol-Ar_2 spectra together with the results of quantum chemical calculations.
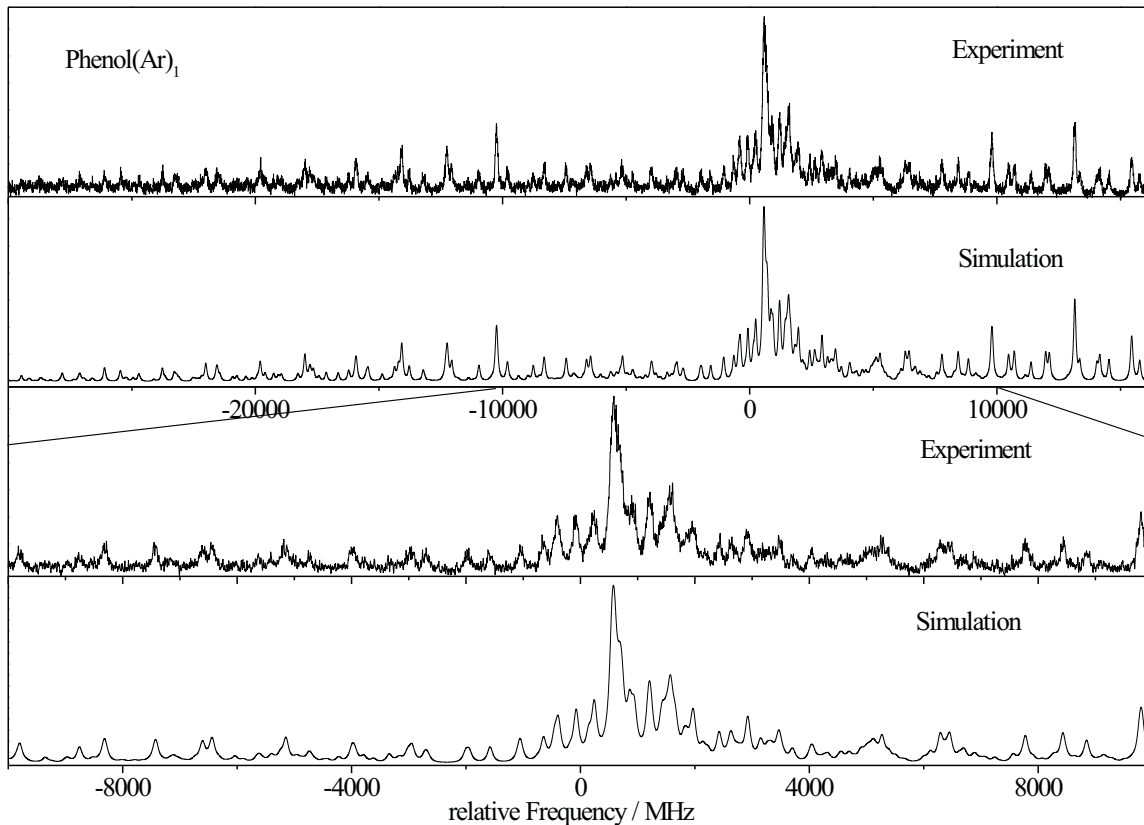
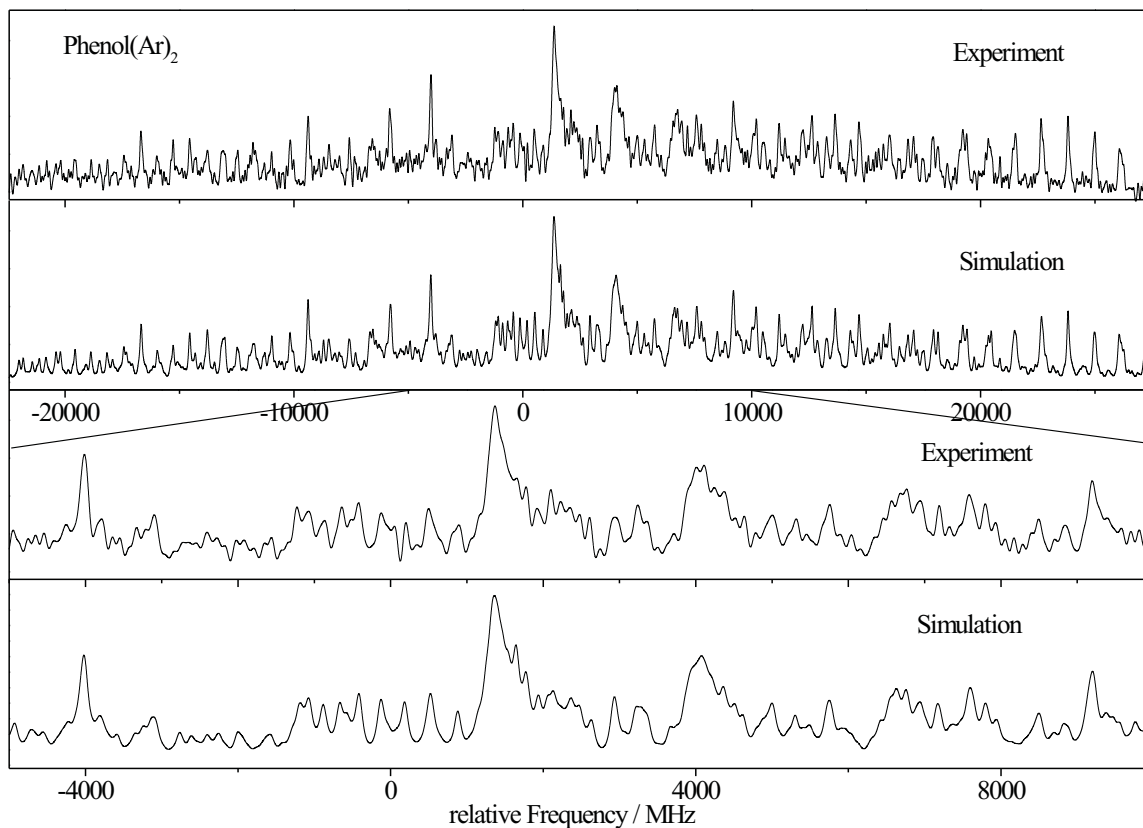**Figure 3.2:** Rotationally resolved spectrum of the electronic origin of the phenol-Ar$_1$ cluster at 36315.05 cm^{-1} and simulation of the spectrum using the molecular parameters from the best ES fit, given in Table 3.1. The lower two traces show an expanded view in the range -10000 to 10000 MHz relative to the electronic origin.

Table 3.1: Comparison of the molecular parameters from the fit to the rotationally resolved electronic spectrum of phenol-Ar$_1$ (shown in Figure 3.2) and 7D-phenol-Ar$_1$ (not shown), respectively, to the results of *ab initio* calculations.

	phenol-Ar$_1$		7D-phenol-Ar$_1$	
	Exp.	RICC2	Exp.	RICC2
A'' / MHz	1818.7(5)	1804.00	1780.1(5)	1760.85
B'' / MHz	1124.9(5)	1210.25	1120.2(5)	1202.34
C'' / MHz	917.5(14)	973.25	905.5(7)	958.00
ϕ / $^\circ$	0^a	0.36	0^a	0.37
ν_0 / cm^{-1}	36315.05(1)	36202	36312.74(1)	-
ΔA / MHz	-43.94(6)	-37.12	-43.44(3)	-34.61
ΔB / MHz	24.40(3)	31.66	25.19(2)	31.30
ΔC / MHz	23.35(2)	32.16	23.26(2)	31.44

^{a} Fixed to zero in the fit

The performance of different basis sets for these calculations is compared in Table 3.3.

Figure 3.3: Rotationally resolved spectrum of the electronic origin of phenol-Ar_2 at 36280.94 cm^{-1} and simulation of the spectrum using the molecular parameters from the best ES fit, given in Table 3.2. The lower two traces show an expanded view in the range -5000 to 9000 MHz relative to the electronic origin.
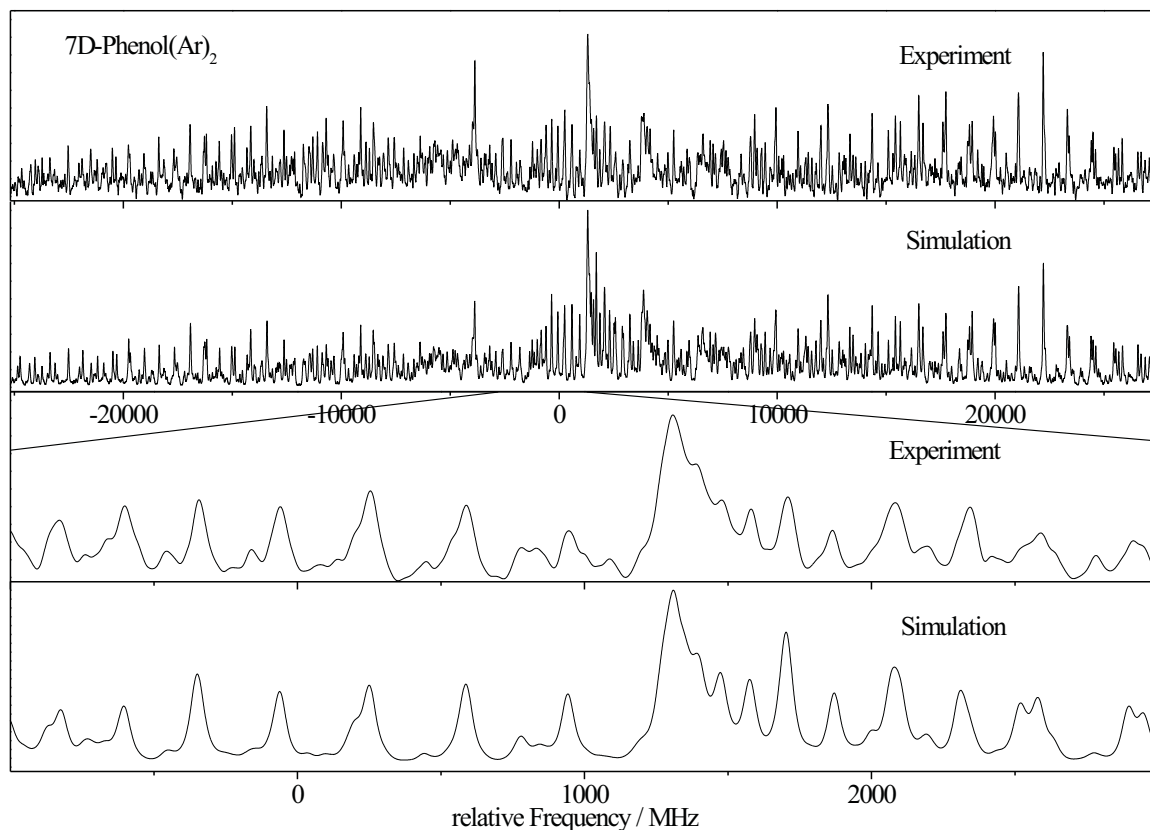
Table 3.2: Comparison of the molecular parameters from the fit to the rotationally resolved electronic spectrum of phenol-Ar_2 and 7D-phenol-Ar_2 shown in Figures 3.3 and 3.4, respectively, to the results of *ab initio* calculations of the (1|1) structure.

	phenol-Ar_2		7D-phenol-Ar_2	
	Exp.	RICC2	Exp.	RICC2
A'' / MHz	1777.6(5)	1774.10	1726.4(5)	1724.23
B'' / MHz	462.5(3)	496.74	462.1(2)	496.41
C'' / MHz	420.7(5)	449.69	417.8(2)	446.67
ϕ / $^\circ$	0^a	0.35	0^a	0.35
ν_0 / cm^{-1}	36280.94(1)	37395	36278.62(1)	-
ΔA / MHz	-18.44(2)	-25.92	-15.45(2)	-22.76
ΔB / MHz	12.33(2)	19.23	12.31(2)	19.21
ΔC / MHz	13.23(2)	18.97	13.19(2)	18.85

^{a} Fixed to zero in the fit

3.3.4 The structure of the phenol-$Ar_{1,2}$ clusters

The structure of the phenol-Ar_1 cluster is clear from previous work,[18,78] as well as from the data in Table 3.1: it is a van der Waals bonded structure. Calculations

Figure 3.4: Rotationally resolved spectrum of the electronic origin of 7D-phenol-Ar$_2$ at 36278.62 cm^{-1} and simulation of the spectrum using the molecular parameters from the best ES fit, given in Table 3.2. The lower two traces show an expanded view in the range -1000 to 3000 MHz relative to the electronic origin.

Table 3.3: Calculated ground state geometry parameters of phenol-(Ar)$_2$.

			RICC2		Exp.
	TZVP	TZVPP	aug-cc-pVTZ	aug-cc-pVQZ	
A'' / MHz	1724.23	1755.58	1751.42	1757.51	1777.6(5)
B'' / MHz	496.41	495.06	509.21	509.92	462.5(3)
C'' / MHz	446.67	447.16	458.48	459.24	420.7(5)

also indicate the existence of a second stable structure, in which the argon atom is hydrogen bonded to the phenol OH group. However, this structure was not found in the experiment. Both structures are depicted in Figure 3.5. The structure of the phenol-Ar$_2$ cluster, however, has been the subject of considerable debate. The most important clue as to its structure is the rotationally resolved electronic spectrum of its origin. The rotational constants that can be expected for the different possible configurations are given in Table 3.4. Only for the hydrogen bonded structure are the changes in rotational constants on electronic excitation not given, since no stable S$_1$ state minimum was found. The corresponding structures are depicted in Figure 3.6. Comparison with the best experimental parameters from Table 3.2 provides clear evidence for the (1|1) structure of this cluster. Furthermore, the A rotational constants of phenol-Ar$_2$ in its ground (A''=1777.52(5) MHz) and electronically excited state

(A'=1759.17(5) MHz) are very close to the respective C rotational constants in bare phenol (C''=1789.855(3) MHz), C'=1756.10(4) MHz).[120] This finding immediately allows the conclusion that both Ar atoms are located close to the a-axis in the cluster (which was the c-axis in the monomer) and that the change of the position of the Ar atoms on electronic excitation occurs nearly perpendicular to the aromatic plane. The combination of these two observations doesn't leave any room for debate: the cluster observed here is the symmetric, van der Waals bonded (1|1) cluster.
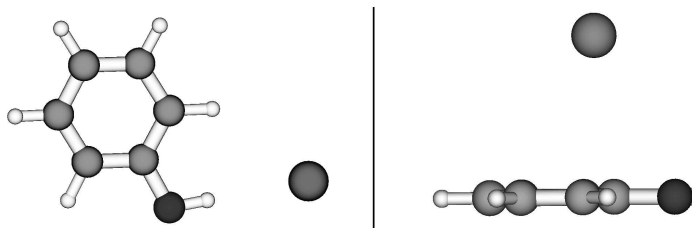
Figure 3.5: Geometries of both calculated phenol-Ar$_1$ clusters: the hydrogen bonded structure (left) and the van der Waals bonded structure (right).

Table 3.4: RICC2 calculated rotational constants for several possible phenol-Ar$_2$ complexes. In the hydrogen bonded structure one of the argon atoms is van der Waals bonded to the benzene ring while the other is hydrogen bonded to the hydroxy group and located in the phenol plane.

	Van der Waals		Hydrogen bonded
	(1|1)	(2|0)	
A'' / MHz	1774.10	1095.36	1133.3
B'' / MHz	496.74	651.69	443.3
C'' / MHz	449.69	512.40	384.9
ΔA / MHz	-25.92	93.12	-
ΔB / MHz	19.23	-52.02	-
ΔC / MHz	18.97	-15.05	-

3.3.5   Structural parameters

The exact structures of the van der Waals bonded phenol-Ar$_{1,2}$ clusters were determined from the rotational constants by a pseudo-Kraitchman fit as described by Schmitt *et al.*[121] using the normal and hydroxy deuterated isotopologues and RICC2/TZVP calculated monomer geometries.

For the $n = 1$ cluster the perpendicular distance of the argon atom to the aromatic plane is given in Table 3.5 and compared to the respective result from the RICC2 optimized structures. On electronic excitation, the Argon distance decreases by more than 6 pm. This decrease can be traced back to the expected increase of dispersion energy for excited state complexes and to favorable orbital interactions that are repulsive in the ground state due to the Pauli exclusion principle.

For the $n = 2$ cluster a slightly larger distance (about 2 pm) of the Argon atom to the aromatic plane is observed for both the ground and the electronically excited
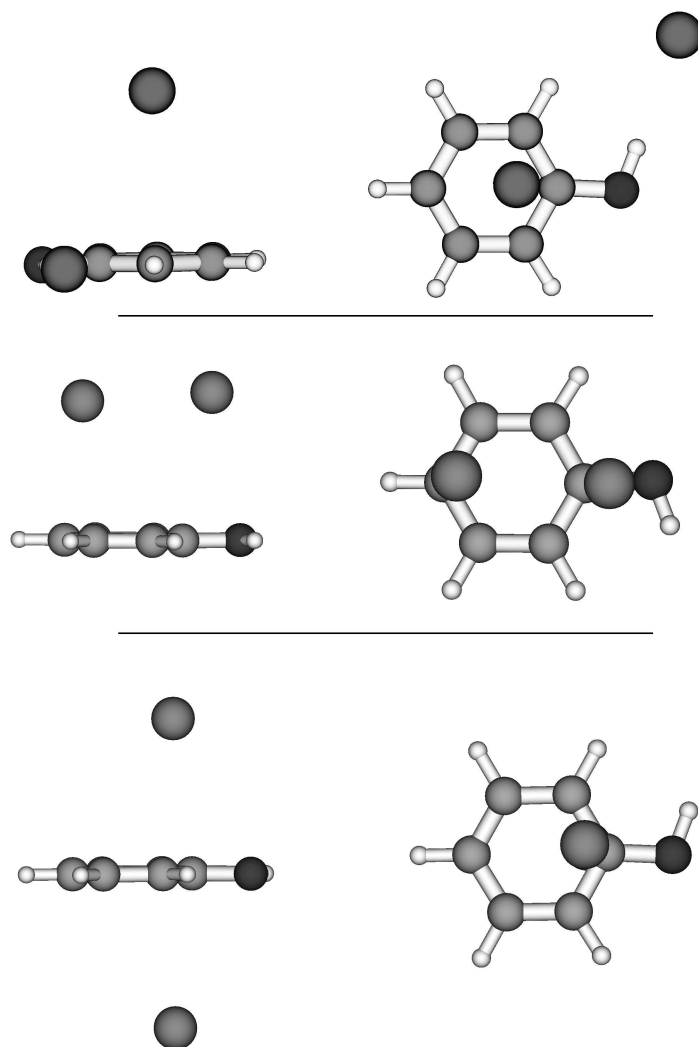
Figure 3.6: Geometries of various phenol-Ar_2 clusters: the hydrogen bonded structure (top), the (2|0) structure (middle) and the (1|1) structure (bottom).

Table 3.5: Aromatic plane-Ar atom distances (pm) in the phenol-Ar_1 complex obtained from a pseudo-Kraitchman fit and calculated from the RICC2/TZVPP optimized structures in the ground and first electronically excited state.

	RICC2	Experiment
S_0	340.7	352.6(9)
S_1	333.9	346.1(8)

state than for the $n = 1$ cluster (cf. Table 3.6). For the *pseudo*-Kraitchman fit the distance of both Argon atoms to the ring system was chosen to be the same. The experimentally determined distances in the $n = 1$ and $n = 2$ clusters agree reasonably well with the *ab initio* RICC2 calculated parameters.

In order to understand why the distance of the argon atoms to the phenol ring is larger for the $n = 2$ cluster, a breakdown of the total binding energy of the argon atoms to the phenol ring into its constituents is presented in Table 3.7. As can be seen from the table, the combination of Pauli exchange repulsion and electrostatic

Table 3.6: Aromatic plane-Ar atom distances (pm) in the phenol-Ar_2 complex obtained from a pseudo-Kraitchman fit and calculated from the RICC2 optimized structures in the ground and first electronically excited state.

			RICC2		Experiment
	TZVP	TZVPP	aug-cc-pVTZ	aug-cc-pVQZ	
S_0	343.5	345	336	336	354.5(2)
S_1	336.0	336	-	-	348.5(4)

interaction for the $n = 2$ cluster is a little less than half that for $n = 1$, which is compatible with the larger distance to the phenol plane. The contribution per argon atom due to dispersion interaction is exactly equal for both clusters, and only the induction part is notably different. Since the dominant induction term is the dipole - induced dipole interaction, the most likely explanation for the importance of this term is that the symmetry of the $n = 2$ complex does not allow the existence of a contribution to the induced dipole moment perpendicular to the phenol-plane. In the $n = 1$ complex, however, a small contribution is possible if the argon atom is not located exactly above the center of mass of the complex.

Table 3.7: Breakdown of the different contributions to the binding energy (in kJ/mol) of argon atoms to the phenol ring. Calculations were done at the B97-D/def2-TZVP EDA level of theory.

Complex	Total	Pauli	Electrost.	Pauli + Electrost.	Induct.	Dispers.
phenol-Ar_1	-0.378	0.282	0.659	0.941	-0.282	-1.037
phenol-Ar_2	-0.705	0.493	1.369	1.863	-0.493	0.705
$\frac{1}{2}*$phenol-Ar_2	-0.352	0.247	0.685	0.930	-0.247	-1.037

Table 3.8 compares the calculated and experimentally determined distances of the argon atom(s) in the $n = 1$ and $n = 2$ clusters of the phenol-Ar and benzene-Ar systems. Theory clearly shows that attachment of the second argon atom weakens the first van der Waals bond in both the phenol and the benzene system. This trend is reproduced in the current experiments but does not show up in the benzene-Ar clusters, investigated by Weber and Neusser.[122] For both $n = 1$ and $n = 2$ the benzene-Ar clusters are more tightly bound than the respective phenol-Ar cluster. It therefore seems that in the latter system the increase in electrostatic repulsion due to the donation of π-electron density into the ring by its hydroxy group is larger than the increase in inductive and dispersive attraction.

3.3.6 Vibrational frequencies

Shown in Table 3.9 are the vibrational frequencies for the phenol-$(Ar)_2$ cluster obtained from its REMPI spectrum (Figure 3.1) together with the RICC2 S_1-state vibrational frequencies for the (1|1) cluster. The frequencies are somewhat overestimated, but on the whole the agreement is satisfactory. To check whether the assignments given in Table 3.9 are reasonable a Franck-Condon simulation was performed using the geometries and the Hessian matrix from the RICC2 calculations of both electronic

Table 3.8: Comparison of the experimental and calculated aromatic plane-Ar atom distances (pm) for the phenol-$(Ar)_n$ and the benzene-$(Ar)_n$ complexes from the RICC2/TZVPP optimized structures. Experimental results for benzene-$(Ar)_n$ from Weber and Neusser.[122]

	Theory		Experiment	
	n=1	n=2	n=1	n=2
phenol-Ar_n	341	345	353	355
benzene-Ar_n	333	336	358	358

states and the changes of the rotational constants given in Table 3.2. The result is displayed in Figure 3.7 and can be seen to be in excellent agreement with the assignments of Table 3.9.

Table 3.9: Phenol-Ar_2 vibrational frequencies (in cm^{-1}) as determined from Figure 3.1 together with RICC2/TZVP S_1-state vibrational frequencies for the (1|1) cluster.

Experiment	RICC2	Assignment
16	18	b_x^1
32	-	b_x^2
43	51	s_z'
46	-	b_x^3
55	-	$s_z'+b_x$
67	-	b_x^4

The vibrational assignments show that all peaks in REMPI spectrum can be explained as progressions and combinations of just two modes: b_x and s_z. In transitions from the ground state, these two modes are the only two that are allowed if C_{2v} symmetry is assumed, which is a near-symmetry group for the (1|1) cluster.[107] Under its proper symmetry group, C_s, b_y also becomes allowed, although its transition strength is expected to be low. In contrast, the (2|0) structure has C_1 symmetry and all intermolecular vibrations are allowed in this isomer. The vibrational assignments of Table 3.9 are therefore in agreement with the (1|1) structure of the observed cluster.

3.3.7 Excited state lifetimes

From the Lorentzian contribution to the Voigt linewidth the lifetimes of the different phenol-Ar_n clusters and their deuterated isotopologues were assessed. The values are compiled in Table 3.10 and compared with the respective lifetimes of the monomers. Both the lifetimes for the undeuterated and the deuterated clusters are considerably shorter than the monomer lifetimes. Furthermore, the longer lifetime of the deuterated isotopomer relative to the natural isotopomer is maintained in the argon clusters.

Two competing models of nonradiative decay have been discussed in the literature to explain the phenol excited state lifetime. Following initial work by Bixon and Jortner[123] the first model, introduced by Lipert and Colson,[124–126] suggests that the dominant pathway of nonradiative decay of the S_1 state is intramolecular vibrational
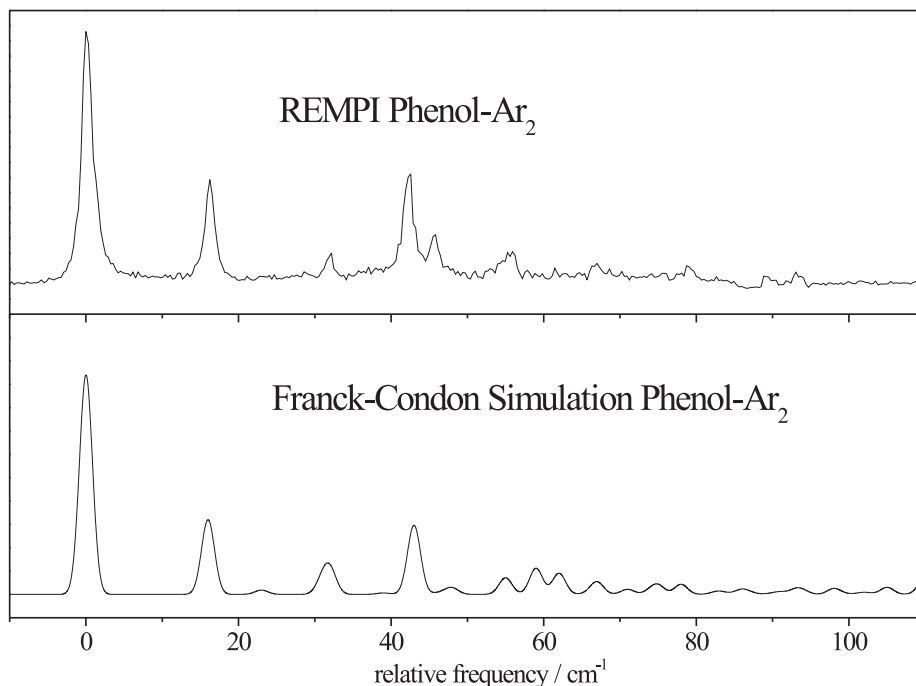
Figure 3.7: Franck Condon simulation of the Phenol-Ar_2 REMPI spectrum shown in Figure 3.1b. Frequencies are given with respect to the $S_1 \leftarrow S_0$ origin transition at 36280.94 cm^{-1}. The corresponding peak assignments are given in Table 3.9.

Table 3.10: S_1 state life times (in ns) of phenol, 7D-phenol, and their $n = 1$ and $n = 2$ argon clusters.

n	phenol	[7D]-phenol
0^a	2.4 ±0.3	13.3±1.6
1	1.5±0.4	8.2±0.2
2	1.5±0.4	3.9±0.2

^{a} Ratzer *et al.*[24]

relaxation (IVR) to the S_0 state. Since in bare phenol the OH stretching mode has the highest frequency it should be the main accepting mode for this process. Lowering its frequency by deuteration or hydrogen bonding will lead to a smaller Franck-Condon factor, which will lower the IVR rate and result in a longer excited state lifetime, as was observed in their experiments. Formation of a van der Waals cluster with argon will add three low-frequency intermolecular vibrational modes, which will increase the S_0 vibrational state density at the position of the S_1 state. In this model the lifetimes would therefore be expected to decrease with the addition of argon atoms, in agreement with experimental observations.

More recently, Sobolewski and Domcke[127,128] performed calculations on nonradiative decay in the phenol S_1 state. They showed that the potential energy surface of the $^1\pi\sigma^*$ state, when plotted as a function of the OH stretching coordinate, intersects both the $S_1(^1\pi\pi^*)$ state and the S_0 state. Once the system tunnels through the barrier separating the $^1\pi\pi^*$ state from the $^1\pi\sigma^*$ state it will therefore very quickly relax back to the ground state. The different lifetimes of the deuterated and hydrogen bonded

clusters with respect to the bare phenol are now explained by a shift in the relative position of their potential energy curves. Given the fact that in the argon cluster the phenol π-electron system is involved in van der Waals bonding to the argon atom, it would seem likely that transferring one of the π-electrons to a σ^* orbital would require more energy than it would in the bare phenol. This means that in the argon cluster, the $^1\pi\pi^*$ state would be stabilized with respect to the $^1\pi\sigma^*$ state leading to a longer lifetime, contrary to observation. In light of this disagreement it is interesting to note that the excited state lifetimes derived by Ratzer *et al.*[24] for a variety a phenol isotopomers show that deuteration in the 2- or 3-position of 7D-phenol substantially lengthens the excited state lifetime. This means that the 1-dimensional model employed by Soboloweski and Domcke is certainly insufficient for a good description of the cluster dynamics in this system. If this theory is to explain the experiments we therefore speculate that vibrational modes other than the OH stretching mode also play a part in the determination of the effective barrier between the $^1\pi\pi^*$ and $^1\pi\sigma^*$ states. More calculations will need to be performed to test this hypothesis.

3.4 Conclusions

The intermolecular structure of the phenol-Ar_n ($n = 1, 2$) clusters has been investigated with high resolution UV spectroscopy. From the rotational constants it could be deduced that in both clusters the argon atoms are van der Waals bonded to the phenol ring, with the $n = 2$ cluster adopting a conformation where one argon atom is located on each side of the ring (the (1|1) structure). Further evidence for these structures was extracted from REMPI spectra with the help of Franck-Condon simulations. Quantum chemical calculations at the RICC2 level of theory was performed to identify the most stable isomers and was found to be in agreement with these assignments.

The distance between the argon atoms and the phenol ring was found to be slightly larger in the $n = 2$ cluster than in the $n = 1$ cluster. A decomposition of the cluster binding energy into individual contributions showed that this is due to a smaller inductive force between the ring and the argon atom in the $n = 2$ cluster. Since the dominant inductive force arises from dipole-induced dipole interaction it was concluded that a small contribution to the induced dipole moment perpendicular to the phenol plane, which is forbidden by symmetry in the $n = 2$ cluster, is most likely responsible for the smaller distance in the $n = 1$ cluster.

From the Lorentz contribution to the Voigt lineprofile of rovibronic transitions in the high resolution spectrum it was deduced that the phenol excited state lifetime is shortened on cluster formation. Although the dominant pathway of nonradiative decay could not be determined from the experiment, it is suspected that intramolecular vibrational relaxation (IVR) plays an important role.

Structure and internal rotation in the S_0 and S_1 states of *o*-toluidine studied by high resolution UV spectroscopy

The rotationally resolved spectrum of the *o*-toluidine $S_1 \leftarrow S_0$ origin was measured using laser induced fluorescence spectroscopy. From the resulting spectrum torsional barriers to internal rotation of the methyl group were derived, which resulted in S_0 state values of $V_3 = 699 \pm 11$ cm^{-1} and $V_6 = 64 \pm 11$ cm^{-1} with an effective rotational constant F of 5.38 ± 0.04 cm^{-1} while for the S_1 state the result was $V_3 = 40.87 \pm 0.14$ cm^{-1} and $V_6 = $ -16.8 $\pm$ 0.8 cm^{-1} with $F = 5.086 \pm 0.001$ cm^{-1}. The S_1 state structure was found to be severely distorted, with the methyl group making a 7.7° degree angle with the benzene ring. Evidence for an excited state precessional motion of the methyl group was found.

4.1   Introduction

One of the fundamental motifs in organic chemistry are aromatic rings, and substituted benzenes have therefore been studied vigorously over the years using a plethora of spectroscopic techniques. Some of the more interesting substitutions involve flexible groups which give rise to dynamics, such as an amino group (aniline) or a methyl group (toluene). In this paper the dynamics in *o*-toluidine (also named *o*-methylaniline), where both these groups are attached to the benzene ring in neighbouring positions, will be investigated.

From aniline it is known that in the ground state its amino group is pyramidal with respect to the benzene plane but that its structure is quasi-planar in the S_1 state.[129,130] From far-infrared (FIR) spectra the inversion barrier was determined to be around 525 cm^{-1}.[131,132] High resolution laser induced fluorescence (LIF) spectra were unable to resolve a tunneling splitting corresponding to the inversion motion, in keeping with this high barrier.[133,134] The situation for the toluidines is very similar. The NH$_2$ inversion barriers in *o*-, *m*- and *p*-toluidine were measured to be 558, 528 and 588 cm^{-1}, respectively, all a little higher than in aniline due to a higher electron

density on the amino nitrogen atom.[135] High-resolution spectroscopy of *p*-toluidine did not reveal a tunneling splitting due to the inversion motion.[136] Such a splitting is therefore not expected to show up in the *o*-toluidine spectrum.

The barrier to internal rotation of the methyl group in substituted toluenes has been investigated for a large number of substituents and substitution positions; a nice overview can be found in a paper by Zhao *et al.*[137] Looking through the tables in this paper a general trend can be observed: for ortho-substituted toluenes electronic excitation dramatically reduces an initially high threefold barrier, whereas for meta-substituted toluenes the methyl group rotation is almost free in the S_0 state but becomes severely hindered in the S_1 state. Since the para-substituted toluenes have no threefold barrier due to their higher symmetry their barriers are generally lower, but the same general effect as in meta-substituted toluenes can be observed. This means that the barrier height depends much more on the substitution position than on the exact nature of the substituent, and an explanation for these effects is most likely connected to the electronic configuration of these substances. When the substituents considered here, which are all electron donating groups, are replaced with an electron withdrawing group we would therefore expect to see very different behavior, as was confirmed in later experiments on tolunitrile.[138] In the case of *o*-toluidine the barriers to internal rotation were determined from fluorescence excitation and dispersed fluorescence spectra by Okuyama *et al.* which resulted in $V_3 = 703$ cm^{-1}, $V_6 = 62$ cm^{-1} in the S_0 state and $V_3 = 40$ cm^{-1}, $V_6 = -11$ cm^{-1} in the S_1 state.[139] The barrier in the cation was measured to be $V_3 = 649$ cm^{-1}, $V_6 = 19$ cm^{-1}.[140,141]

Calculations on various substituted toluenes have been quite succesful in reproducing measured barriers by relating its height to the Hammett σ constant of the substituent combined with substitution position[142] and the difference in π- bond order between both ring carbon bonds geminal to the methyl rotor.[143] These calculations show that the molecular structure changes with rotation of the methyl group, regardless of substituent or substitution position. Molecular geometries and conformational preferences of toluidines are therefore closely connected to the barriers to internal rotation.

P-toluidine has been studied most extensively since steric hindrance between the methyl and amino groups is absent and it is highly symmetric.[136,144–147] The electronic effects described in the previous paragraph are found to induce a precession of the methyl group with its rotation. Moving to *m*- and *o*-toluidine steric hindrance enhances this precessional motion and leads to distortions of both the methyl and the amino group.[148–151] Simulations by Brodersen *et al.* have revealed that typical changes in rotor axis orientation in substituted toluenes are on the order of 1.5 degrees.[152]

In this paper the rotational constants of *o*-toluidine in its S_0 and S_1 states will be determined from rotationally resolved UV LIF spectra and these will be used to derive an exact molecular structure. Furthermore, accurate barriers to internal rotation of the methyl group will be derived from the spectra and possible evidence for a precessional motion of the methyl rotor will be discussed.

4.2 Methods

4.2.1 Experimental procedures

The experimental setup for the rotationally resolved LIF is described elsewhere.[58] Briefly, it consists of a frequency doubled Nd: YAG laser which pumps a ring dye laser (Coherent 899-21) operated with Rhodamine 6G. The dye laser output is coupled into an external folded ring cavity (Spectra Physics Wavetrain) for second harmonic generation. The typical output power is 20 mW and is constant during each experiment.

The molecular beam is formed by co-expanding argon at a backing pressure of 340 mbar and room temperature *o*-toluidine into the vacuum through a 320 μm nozzle. The molecular beam machine consists of three differentially pumped vacuum chambers that are linearly connected by skimmers (1 mm and 3 mm diameter, respectively). In the third chamber, 360 mm downstream of the nozzle, the UV laser beam crosses the molecular beam at right angles. Imaging optics focus the total undispersed fluorescence from the excited molecules onto a photo-multiplier tube mounted perpendicular to the plane defined by the laser and the molecular beam. Its output is discriminated and digitized by a photon counter card inside a personal computer. The Doppler width of measured transitions is 25 MHz (FWHM). Relative frequencies are determined with a quasi-confocal Fabry-Perot interferometer with a free spectral range (FSR) of 149.9434(56) MHz. The absolute frequency is obtained by comparing the recorded iodine absorption spectrum with tabulated lines.[5]

O-toluidine ($\geqslant 99\%$) was obtained from Aldrich and used without further purification.

4.2.2 Computational methods

Ab initio calculations

Structure optimizations were performed employing the valence triple zeta basis set with polarization functions (d,p) from the TURBOMOLE library.[59,60] The equilibrium geometries of the electronic ground and the lowest excited singlet states were optimized at the CC2 level within the resolution-of-the-identity approximation.[61,62] Ground state vibrational frequencies have been calculated through analytical second derivatives using the aoforce module[110,111] implemented in Turbomole Version 5.8. Excited state vibrational frequencies were calculated using numerical differentiation of analytic gradients using the NumForce script of Turbomole Version 5.8.

The singlet state energies, wavefunctions, and transition dipole moments were calculated using the combined density functional theory/multi-reference configuration interaction (DFT/MRCI) method by Grimme and Waletzke.[63] The configuration state functions (CSFs) in the MRCI expansion are constructed from Kohn-Sham (KS) orbitals, optimized for the dominant closed shell determinant of the electronic ground state employing the BH-LYP functional.[64,65] All valence electrons were correlated in the MRCI runs and the eigenvalues and eigenvectors of the lowest singlet state were determined. The initial set of reference configuration state functions was generated automatically in a complete active space type procedure (including all single and double excitations from the five highest occupied molecular orbitals in the

KS determinant to the five lowest virtual orbitals) and was then iteratively improved. The MRCI expansion was kept moderate by extensive configuration selection. The selection of the most important CSFs is based on an energy gap criterion as described by Grimme and Waletzke.[63] Only those configurations were taken into account whose energy did not exceed a certain cutoff energy. The energy of a given configuration was estimated from orbital energies within the selection procedure. The cutoff energy was given by the energy of the highest desired root as calculated for the reference space plus a cutoff parameter $\delta E_{sel} = 1.0 E_{\mathrm{H}}$. This choice has been shown to yield nearly converged results.[63]

Spectral analysis

To describe the *o*-toluidine spectrum a torsion-rotation Hamiltonian of the following form was used:[11]

$$H_{tr} = F(p - \vec{\rho} \cdot \vec{J})^2 + V(\alpha) + A J_a^2 + B J_b^2 + C J_c^2. \tag{4.1}$$

In this equation A, B and C are the molecule's rotational constants, J_a, J_b and J_c are the projections of the total angular momentum $\vec{J}$ onto the main inertial axes a, b and c, respectively, and $V(\alpha)$ is the torsional potential, which takes the form:

$$V(\alpha) = \frac{V_3}{2}(1 - \cos 3\alpha) + \frac{V_6}{2}(1 - \cos 6\alpha). \tag{4.2}$$

Furthermore, $p = -i\hbar\frac{\partial}{\partial\alpha}$ is the angular momentum operator conjugate to the torsional angle α and F is the internal rotation constant, which is related to the moment of inertia of the internal rotor I_α and its torsional constant, F_{top}, *via*:

$$F = \hbar^2/2 r I_\alpha = F_{top}/r, \tag{4.3}$$

with

$$r = 1 - I_\alpha \sum_g \cos^2(\eta_g)/I_g. \tag{4.4}$$

I_g (g = a,b,c) are the moments of inertia of the entire molecule and $\cos\eta_g$ are the direction cosines of the methyl top axis with respect to the main inertial axes. Finally, the parameter ρ in equation 4.1 is related to these direction cosines through the equation:

$$\rho_g = (I_\alpha/I_g)\cos\eta_g. \tag{4.5}$$

This equation can be rewritten in terms of the polar angles (ζ,η), where ζ is the angle between the methyl top axis and the c-axis and η is the angle between the projection of the methyl top axis onto the *ab*-plane and the a-axis. When this is done the components of ρ are given by:

$$
\begin{aligned}
\rho_a &= (I_\alpha/I_a)\sin\zeta\cos\eta \\
\rho_b &= (I_\alpha/I_b)\sin\zeta\sin\eta \\
\rho_c &= (I_\alpha/I_c)\cos\zeta.
\end{aligned} \qquad (4.6)
$$

It will be shown in section 4.3 that the torsional splitting in the ground state is too small to be measured in the experiment described here, which means that no information on the corresponding ground state parameters can be derived. The only information on the torsional potential that can be extracted from the spectrum are the values of V_3', F', η' and ζ'. An initial fit of the rotationally resolved spectrum was performed with the Evolutionary Algorithm (EA) automatic fitting program[17–19] using the recently implemented DR2 algorithm.[117] For this fit the values of V_3'', V_6'', F'' and V_6' were taken from Okuyama *et al.*[139] while the values for η'' and ζ'' were fixed to those that resulted from RICC2 calculations. In a second step the resulting V_3', F', η' and ζ' were used in combination with torsional transition frequencies measured by laser induced fluorescence[151] and dispersed fluorescence[139] spectroscopy to determine the values of the torsional parameters that were kept fixed in the first fit. This was done with the program HTorFit.[153]

4.3 Results and Discussion

Figure 4.1 shows the rotationally resolved $S_1 \leftarrow S_0$ origin spectrum of *o*-toluidine. It consists of two spectral components separated by 98584 ± 5 MHz. As has been shown previously[150,151] these result from transitions between the two lowest torsional levels which arise from internal rotation of the methyl group. The lower of the two components is due to transitions between nondegenerate levels of a_1 symmetry while the upper one results from transitions between doubly degenerate torsional levels of e symmetry. Shown in the panel below the spectrum is the best fit. The correspondence between the two is excellent, as is also evidenced by the enlarged portion depicted in the two panels below it. The bottom panel of Figure 4.1 shows a stick spectrum of the strongest transitions in the simulation and a convolution of these with a Lorentzian function with a width (FWHM) of 0.3 cm^{-1}; the resulting spectrum matches the rotational contour spectra from Ballesteros and Santos[151] quite well.

From the ordering of the two torsional components it can immediately be concluded that the barrier to internal rotation must be lower in the S_1 state than it is in the S_0 state. To obtain exact values for the barriers to internal rotation a combined fit of this spectrum with the torsional bands measured in previous work[139,151] was performed as described in section 4.2.2. The molecular parameters deduced from this analysis, together with the values obtained from *ab initio* calculations, are given in Table 4.1. Calculated torsional transitions are compared with measured ones in Table 4.2. From the second table it can be seen that, again, the deduced parameters are in excellent agreement with experiment.

A two temperature model[119] was used to describe the rotational temperature in the molecular beam, which yielded $T_1 = 2.1$ K and $T_2 = 3.6$ K with a relative T_2 weight of 0.14. From a 26.8 MHz Lorentzian contribution to the total linewidth the excited
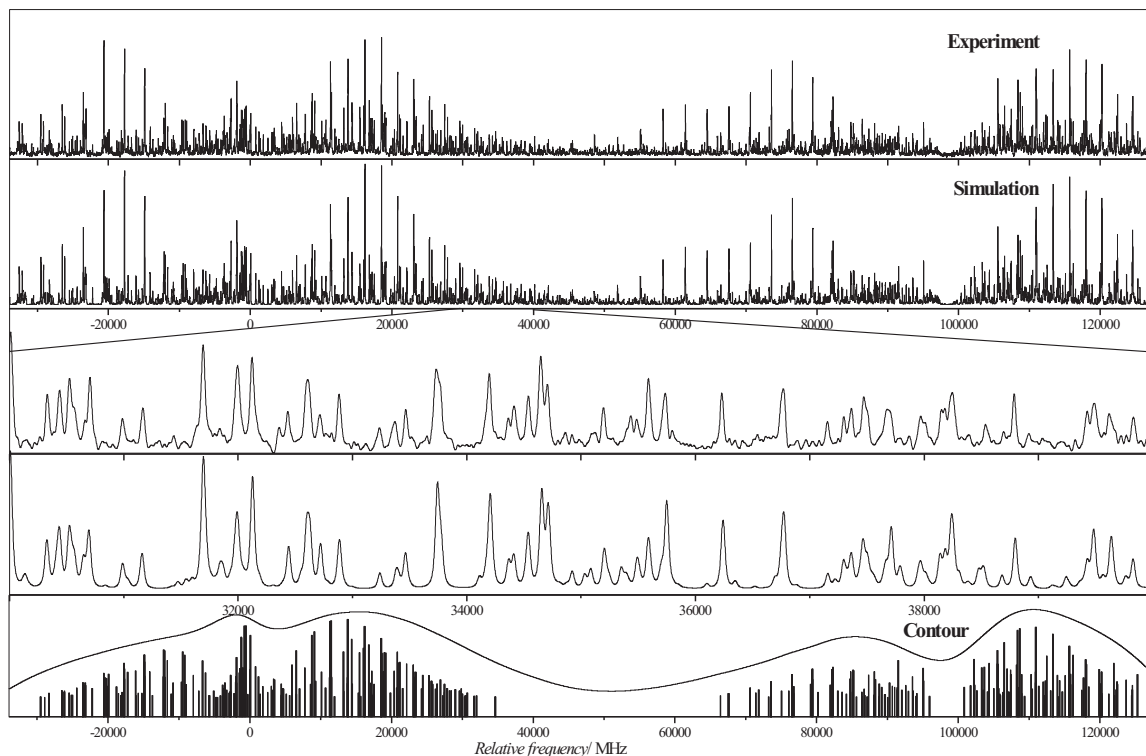
Figure 4.1: The electronic origin of *o*-toluidine at 34316.848 cm^{-1}. The upper two traces show the measured spectrum and the best simulation. In the two traces below that an enlarged part of the spectrum is shown. The bottom trace shows a stick spectrum which contains the strongest transitions from the simulation shown in the second trace and a convolution of these with a Lorentz function (FWHM 0.3 cm^{-1}).

state lifetime is found to be around 6.0 ns, which is substantially longer than the 3.5 ns lifetime in *p*-toluidine[136] and much closer to the 7.2 ns measured in aniline.[130]

4.3.1 Transition dipole moment

The value of ϕ in Table 4.1 indicates that the transition dipole moment (TDM) lies in the plane of the benzene ring. While the sign of the angle θ normally cannot be determined from the experiment since the relative intensities in the spectrum only depend on the square of the transition dipole moment components, its sign can be determined in molecules that possess an internal rotor. This happens because the intensities of some of the e-type transitions depend on the relative signs of θ and η.[154–156] Since the sign of η is known from geometrical considerations this fixes the absolute sign of θ. In the case at hand the result is that the TDM orientation has to be in the direction of the methyl group, which corresponds to the plus sign in Figure 4.2.

From a comparison of the measured rotational constants with those resulting from RICC2 calculations it can be seen that the correspondence is satisfactory, and as will be discussed in section 4.3.3 the calculations indicate that the amino group is nonplanar in the S$_0$ state and becomes more planar in the S$_1$ state. This effect is also observed in aniline, where the transition dipole moment is perpendicular to the amino

Table 4.1: Molecular parameters of *o*-toluidine as determined from the fits to the $S_1 \leftarrow S_0$ origin transition shown in Figure 4.1. For a description of the fitting procedure see section 4.2.2. Also listed are the results of *ab initio* calculations at the RICC2/TZVP and DFT/MRCI levels of theory.

	S_0			S_1				$\Delta(S_1 - S_0)$
	Exp.	RICC2	Ref. 139	Exp.	RICC2	Ref. 139	Ref. 149	Exp.
A/MHz	3229.60(17)	3268	-	3121.92(14)	3098	-	-	-107.68(18)
B/MHz	2188.49(16)	2219	-	2181.97(13)	2187	-	-	-6.52(22)
C/MHz	1316.82(9)	1334	-	1296.03(12)	1295	-	-	-20.79(13)
ΔI (amu Å^2)	-3.62(4)	-3.59	-	-3.60(5)	-4.00	-	-	0.02(5)
V_3 (cm^{-1})	699(11)	657	703	40.87(14)	120	40	35	-658(11)
V_6 (cm^{-1})	64(11)	-	62	-16.8(8)	-	-11	28	-81(11)
F_{top} (cm^{-1})	5.28(4)	5.51	5.18	5.086(1)	5.48	5.30	5.1	-0.19(4)
F (cm^{-1})	5.38(4)	5.62	5.28	5.184(1)	5.59	5.40	5.2	-0.19(4)
η (°)	28.7^a	28.7	-	28.14(12)	26.1	-	-	7.1(23)
ζ (°)	89.5^a	89.5	-	71.6(7)	88.1	-	-	-18.3(6)

|	Exp.	RICC2	DFT/MRCI	Ref. 139	Ref. 149
θ (°)	+37.47(26)	±31.5	+38.9	-	-
ϕ (°)	89.3(8)	90.0	88.9	-	-
ν_0 (cm^{-1})	34316.848(1)	36137	34706	34316	34316
$\nu_0(E)$-$\nu_0(A_1)$/MHz	98584(5)	-	-	≈90000	≈105000
$\Delta_{Lorentz}$/MHz	26.8(10)	-	-	-	-
$\tau_{1/2}$ (ns)	5.95(22)	-	-	-	-

^{a} Fixed to RICC2 calculated value

Table 4.2: Torsional transitions used in the determination of some of the internal rotor parameters of *o*-toluidine given in Table 4.1. For a description of the fitting procedure see section 4.2.2. All values are relative to the $0a_1 \leftarrow 0a_1$ transition, where $\nu\sigma(S_1) \leftarrow \nu\sigma(S_0)$ indicates an absorption band and $\nu\sigma(S_1) \rightarrow \nu\sigma(S_0)$ an emission band.

Transition	Exp.	Fit	Diff.	
$1e \leftarrow 1e$	$98584(5)^a$	98584	0	MHz
$1e \leftarrow 2e$	$27.8(3)^b$	27.4	-0.4	cm^{-1}
$0a_1 \leftarrow 3a_2$	$45.0(3)^b$	45.5	+0.5	cm^{-1}
$0a_1 \leftarrow 3a_1$	$56.2(3)^b$	57.5	+1.3	cm^{-1}
$1e \leftarrow 4e$	$86.8(3)^b$	87.8	+1.0	cm^{-1}
$1e \leftarrow 5e$	$132.1(3)^b$	134.0	+1.9	cm^{-1}
$0a_1 \leftarrow 6a_1$	$196.6(3)^b$	190.9	-5.7	cm^{-1}
$1e \rightarrow 2e$	$182(6)^c$	189	+7	cm^{-1}
$0a_1 \rightarrow 3a_1$	$361(6)^c$	358	-3	cm^{-1}
$1e \rightarrow 4e$	$362(6)^c$	355	-7	cm^{-1}
$1e \rightarrow 5e$	$472(10)^c$	489	+17	cm^{-1}
$0a_1 \rightarrow 6a_1$	$578(10)^c$	578	0	cm^{-1}
$1e \rightarrow 7e$	$589(10)^c$	602	+13	cm^{-1}
$1e \rightarrow 8e$	$684(10)^c$	669	-15	cm^{-1}

[a] This work

[b] Ballesteros and Santos[151]

[c] Okuyama *et al.*[139]
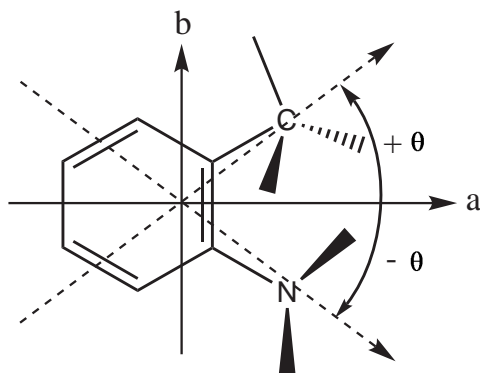
Figure 4.2: Definition of the transition dipole moment direction with respect to the main interial axes.

group CN bond.[130,157] Because the methyl group has a relatively small influence on the benzene π electron system compared to the amino group (inductive vs. mesomeric effect) it therefore seems reasonable to conclude that the electronic excitation must be similar to that in aniline and the transition dipole moment is directed towards the methyl group, which only induces a moderate change in TDM direction with respect to that in aniline.

As can be seen from Table 4.1, the RICC2 calculations also predict the torsional barriers very accurately. Since the torsional barrier in *o*-toluidine is very sensitive

to the local electronic environment at the ring carbon atom the methyl group is attached to, this is another indication that the *ab initio* results are reliable. However, Table 4.1 shows that it doesn't predict the $S_1 \leftarrow S_0$ excitation energy very accurately. Moreover, no information on the sign of the angle θ can be extracted from it. A single point DFT/MRCI calculation at the RICC2 optimized S_1 state geometry was therefore performed, the results of which were added to Table 4.1. Both the size and the direction of the resulting TDM as well as the excitation energy agree very well with experiment.

4.3.2 The methyl rotor

The last piece of information that results from the spectral analysis concerns the methyl rotor geometry contained in the parameters F, η and ζ. To avoid confusion both the values for F and F_{top} defined in equation 4.3 are given in Table 4.1. Immediately apparent is the fact that the parameter ζ has a value which is very different from 90 degrees in the S_1 state. This is certainly not expected and the possibility that the rotor actually makes an 18.4 degree angle with respect to the *ab*-plane is ruled out by the inertial defect, which points to an almost planar structure. This interpretation is therefore disregarded, and since a reasonable correspondence between model and experiment could only be obtained with the parameter values given in Table 4.1 it seems that an alternate model is needed.

For the interpretation of *p*-toluidine spectra Tan *et al.*[136] were forced to use a modified Hamiltonian which accounts for a precessional motion of the methyl rotor axis. Although in the case considered here a fit to the data is possible without inclusion of a precession angle it cannot be ruled out that a second, physically more acceptable solution is possible when it is included. The appropriate form of this Hamiltonian, including a V_3 potential term, was therefore used in an attempt to obtain a fit, but this resulted in a zero degree precession angle. However, this does not rule out the possibility that precessional motion is responsible for the observed effective value of ζ. As was pointed out by Brodersen and Gordon[152] this Hamiltonian does not allow for any motion of the methyl carbon atom with torsional angle and it is therefore still possible that the observed effect is due to motion of the *whole* methyl group. They showed that this results in a marked decrease of the effective rotational constant F with respect to its equilibrium value, and that a precession angle of 1.5° is typical for substituted toluenes. Looking at Table 4.1 again it can indeed be seen that measured values are much smaller than calculated ones and that the difference between the two is much larger in the S_1 state than it is in S_0. The fact that the *ab initio* results predict that the angle ζ becomes 88.1° on electronic excitation, which would mean that the methyl group comes out of the plane by 1.9°, can be viewed as further evidence to support this theory.

4.3.3 Molecular structure

As was already noted in section 4.3.1 the rotational constants that result from RICC2 calculations compare favourably with those obtained from the experiment, which adds credibility to the structure derived from them. A list of geometric parameters is given in Table 4.3; the corresponding atomic numbering is depicted in Figure 4.3.
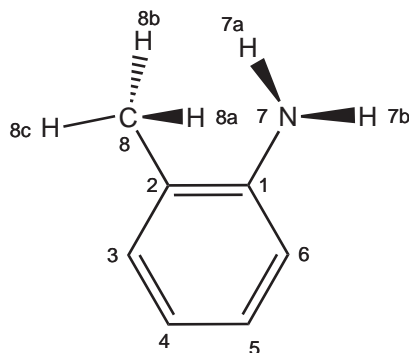
Figure 4.3: Atomic numbering of *o*-toluidine used in Table 4.3.

Table 4.3: Rotational constants and S_0 and S_1 state geometry parameters for *o*-toluidine. Calculated values from this work were obtained at the RICC2/TZVP level of theory. The atomic numbering refers to Figure 4.3.

		S_0				S_1	
	Exp.[a]	RICC2[a]	MP2[b]	HF[c]	Exp.[a]	RICC2[a]	CIS[b]
A/MHz	3229.60	3268	3228	-	3121.92	3098	3196
B/MHz	2188.49	2219	2178	-	2181.97	2187	2240
C/MHz	1316.82	1334	1313	-	1296.03	1295	1328
Bond lengths (pm)							
C_1C_2	-	139.8	141.1	140.1	-	142.9	142.7
C_2C_3	-	138.3	140.0	138.8	-	144.1	137.0
C_3C_4	-	138.4	139.8	138.8	-	141.9	140.0
C_4C_5	-	138.0	139.8	138.5	-	141.6	139.8
C_5C_6	-	138.1	139.6	138.5	-	142.2	136.3
C_6C_1	-	138.7	140.3	139.2	-	143.5	143.6
C_1N_7	-	139.9	141.0	140.1	-	137.2	131.1
C_2C_8	-	150.8	150.5	151.1	-	149.4	150.1
CH (ring)[d]	-	107.5	108.9	107.6	-	108.4	107.3
N_7H_{7a}	-	99.5	101.7[d]	99.8[d]	-	101.1	100.4[d]
N_7H_{7b}	-	99.5	101.7[d]	99.8[d]	-	101.1	100.4[d]
C_8H_{8a}	-	108.8	109.6[d]	108.6[d]	-	109.9	108.4[d]
C_8H_{8b}	-	108.5	109.6[d]	108.6[d]	-	109.3	108.4[d]
C_8H_{8c}	-	108.2	109.6[d]	108.6[d]	-	109.4	108.4[d]
C_1C_4	-	278.4	281.0	279.3	-	281.3	278.8
Bond angles (°)							
$C_1C_2C_3$	-	118.5	118.6	118.5	-	116.7	117.4
$C_2C_3C_4$	-	122.0	121.6	122.0	-	119.0	121.9
$C_3C_4C_5$	-	118.9	119.2	118.9	-	122.4	121.0
$C_4C_5C_6$	-	120.1	120.0	120.1	-	119.4	119.5
$C_5C_6C_1$	-	120.8	120.7	120.8	-	117.9	120.4
$C_6C_1C_2$	-	119.6	119.7	119.6	-	123.2	119.9
$N_7C_1C_2$	-	120.3	119.7	120.2	-	119.5	121.3
$N_7C_1C_6$	-	120.1	120.6	120.1	-	116.8	118.8
$C_1C_2C_8$	-	120.6	120.0	120.6	-	123.2	121.1
$C_3C_2C_8$	-	120.9	121.4	120.9	-	119.8	121.5
$H_{7a}N_7C_1$	-	115.1	114.2	-	-	119.0	123.1
$H_{7b}N_7C_1$	-	114.1	113.2	-	-	117.5	121.2
$H_{7a}N_7H_{7b}$	-	111.0	109.9	110.1	-	116.1	115.7
$C_2C_8H_{8a}$	-	111.8	-	111.3[d]	-	112.4	-
$C_2C_8H_{8b}$	-	111.3	-	111.3[d]	-	113.1	-
$C_2C_8H_{8c}$	-	110.7	-	111.3[d]	-	109.7	-
$H_{8a}C_8H_{8b}$	-	107.5	107.3[d]	107.5[d]	-	107.9	108.0[d]
$H_{8b}C_8H_{8c}$	-	108.0	107.3[d]	107.5[d]	-	106.7	108.0[d]
$H_{8c}C_8H_{8a}$	-	107.3	107.3[d]	107.5[d]	-	106.6	108.0[d]
Dihedral angles (°)							
$C_1C_2C_3C_4$	-	-0.5	-	-	-	-6.0	-
$C_2C_3C_4C_5$	-	-0.1	-	-	-	1.9	-

Continued on next page

Table 4.3 – continued from previous page

| | S0 | | | S1 | | |
	Exp.[a]	RICC2[a]	MP2[b]	HF[c]	Exp.[a]	RICC2[a]	CIS[b]
$C_3C_4C_5C_6$	-	0.2	-	-	-	-4.4	-
$C_4C_5C_6C_1$	-	0.2	-	-	-	10.4	-
$C_5C_6C_1C_2$	-	-0.7	-	-	-	-13.6	-
$C_6C_1C_2C_3$	-	0.9	-	-	-	11.8	-
$C_5C_6C_1N_7$	-	-177.3	-176.8	-	-	-177.5	0.0
$C_6C_1N_7H_{7a}$	-	-148.5	-	-	-	-165.5	-
$C_6C_1N_7H_{7b}$	-	-18.5	-	-	-	-16.8	-
$C_4C_3C_2C_8$	-	179.2	-	-	-	172.3	-
$C_3C_2C_8H_{8a}$	-	116.0	-	-	-	79.0	-
$C_3C_2C_8H_{8b}$	-	-123.7	-	-	-	-158.5	-
$C_3C_2C_8H_{8c}$	-	-3.6	-	-	-	-39.4	-

[a] This work
[b] MP2/6-31+G* (S0) & CIS/6-31+G* (S1), Ballesteros and Santos[151]
[c] HF/6-31+G*, Tzeng *et al.*[150]
[d] Average value

For the S_0 state it can be seen that, with the exception of the C_8H_{8a} bond, all bond lengths are shorter than in either of the two calculations performed so far. In the S_1 state the opposite is found, and most bond lengths tend to be longer. In combination with the observation that almost all bond lengths increase on electronic excitation this means that the effect the excitation has on the *o*-toluidine geometry is much greater than previously thought. This picture is confirmed by the bond angles: whereas in the ground state they coincide very well with the values from previous work, they differ substantially in the electronically excited state.

When the detailed benzene ring geometry is investigated it can be seen that in the S_0 state the ring carbon bond between both atoms the substituents attach to, C_1C_2, is longest whereas the one on the opposite side of the ring, C_4C_5, is shortest. Furthermore, the $C_1C_2C_3$ angle is only 118.5° whereas the $C_2C_3C_4$ angle is 122.0°. These all act to tilt the methyl group away from the amino group. Since the amino group is electron withdrawing in nature, an attempt to explain this using only natural hybrid orbitals (NHOs), as was done for *o*-chlorotoluene and *o*-fluorotoluene by Lu *et al.*,[143] would lead us to expect that the $C_6C_1C_2$ angle is substantially larger than 120°. This is not the case, with its actual value at 119.6° even slightly smaller than 120°. Moreover, NHOs have a local effect on the ring structure and cannot explain the fact that the C_4C_5 bond is shorter than both its neighbours. These results are therefore viewed as evidence that, unlike in *o*-chlorotoluene and *o*-fluorotoluene, steric hindrance is an important factor for the *o*-toluidine structure.

The approximate C_2 symmetry axis which the benzene ring possesses in the ground state, intersecting both the C_1C_2 and the C_4C_5 bonds, is retained on electronic excitation. Simultaneously all ring CC bond lenghts increase, which corresponds to an expansion of the ring. With respect to the average ring CC distance, the C_2C_3 and C_6C_1 bonds are elongated while the C_2C_3 and C_5C_6 bonds are shortened. Combined with the fact that both the C_2C_8 and the C_1N_7 bonds lengths increase this means that the S_1 state is strongly ortho-quinoidal in character. From the ring dihedral angles it can be deduced that the ring geometry also becomes distorted in the out-of-plane direction and adopts a chair conformation similar to that of cyclohexane. Interestingly, while the difference between both CC bond lengths geminal to the methyl group (C_1C_2 and C_2C_3) is 0.3 pm smaller in the excited state than it is in the ground state, they are by no means equal. This means that the barrier to internal rotation of the methyl group is low in the S_1 state even though good, local C_{2v} symmetry at the

C_2 carbon atom is absent. This confirms the conclusion from earlier work that the barrier is mostly electronic in nature and that steric effects are only of secondary importance.[142,143]

From the geometries of the methyl and amino groups it is deduced that steric hindrance not only affects the benzene ring, but also both substituents themselves. In the ground state it can be seen from the methyl group dihedral angles that it is rotated by about 3.8° with respect to its equilibrium position in toluene, which has the C_8H_{8c} bond in the plane of the benzene ring. For the amino group the combination of steric repulsion and the addition of another electron donating group to the ring causes it to be much more planar than in aniline (where it is out of the plane by a 37.5° angle[130]) and tilted away from the methyl rotor, with one hydrogen atom 31.5° below the plane and the other just 18.5°. In the electronically excited state the amino group becomes more planar due to sharing of its lone pair electron with the benzene π-electron system, which points to an electronic excitation comparable to that in aniline. As a result the methyl group orientation is now completely different, with the C_8H_{8a} bond in a much more vertical position, not unlike the situation in toluene.[158] Especially for the methyl group the distortions in the S_1 state are severe, with the three C_2C_8H bond angles differing by as much as 3.4°. Most significantly though, from the $C_4C_3C_2C_8$ dihedral angle the methyl carbon atom is found to move out of the plane of the benzene ring by as much as 7.7°. This supports the explanation that the effective value of 71.6° found for ζ in section 4.3.2 is due to a precessional motion of the whole methyl group.

4.4   Conclusions

The $S_1 \leftarrow S_0$ transition in *o*-toluidine has been measured using rotationally resolved electronic spectroscopy. The resulting spectrum consists of two overlapping spectral components which can be assigned to the $0a_1 \leftarrow 0a_1$ and $1e \leftarrow 1e$ transitions between torsional subbands that arise from internal rotation of the methyl group. The torsional parameters that can be derived were combined with frequencies of torsional transitions from previous work[139,151] to derive accurate barriers to internal rotation in both electronic states. It was found that the V_3 barrier is lowered from 699 cm^{-1} in the S_0 state to 40.87 cm^{-1} in the S_1 state. This dramatic lowering of the barrier to internal rotation is similar to that observed in other ortho-substituted toluenes[137] and can be explained in terms of the difference in π- bond order between both ring carbon bonds geminal to the methyl rotor.[143]

The rotational constants that were determined for both electronic states are close to those that result from RICC2 calculations, and an extensive analysis of the predicted molecular geometry was therefore made. As is usual for substituted benzenes the benzene ring was found to expand on electronic excitation, and the amino group becomes more planar. The excited state geometry has a strongly ortho-quinoidal character which shortens both the methyl CC bond and the amino CN bond. Para-quinoidal distortion is frequently encountered in *p*-substituted benzenes on electronic excitation[158–161] and given the fact that *o*- and *p*-substituted benzenes are electronically similar this is therefore not unexpected. As a result the steric interactions between both substituents, which are already visible in the S_0 state, are increased dramatically

in the S_1 state: the methyl group makes a 7.7° degree angle with the local benzene ring orientation and rotates away from the S_0 state geometry. Combined with the fact that an unrealistically large angle between the normal of the benzene plane and the methyl rotor axis resulted from spectral analysis and that the effective rotational constant F was found to decrease dramatically on electronic excitation, this constitutes compelling evidence for an S_1 state precessional motion of the whole methyl group.[152]

Rotationally resolved electronic spectroscopy of water clusters of 7-azaindole

The rotationally resolved electronic spectra of the electronic origin of the 7-azaindole-$(H_2O)_1$ and 7-azaindole-$(H_2O)_2$ clusters have been measured in a molecular beam. From the rotational constants the structures in the S_0 and S_1 electronic states were determined as cyclic with the pyrrolo NH and the pyridino N atom being bridged by one and two water molecules, respectively. Excited state lifetimes of about 10 ns for both clusters have been found. In the spectrum of the 7-azaindole-$(H_2O)_2$ cluster a splitting of the rovibronic band is observed, which can be traced back to a large amplitude motion involving the out-of-plane hydrogen atoms of the water chain. Both the changes of the rotational constants upon electronic excitation and the orientation of the transition dipole point to a solvent induced state reversal between the L_a and the L_b state upon microsolvation.

5.1   Introduction

In a preceding theoretical study on the lowest electronically excited states of 7-azaindole and the 7-azaindole$(H_2O)_{1,2}$ clusters, the geometries, excitation energies, transition dipole orientations, and natures of the excited states have been predicted at the RICC2 and DFT/MRCI level of theory.[162] In the following some of these theoretical predictions will be tested using rotationally resolved electronic spectroscopy of the 7-azaindole$(H_2O)_{1,2}$ clusters.

Laser spectroscopic investigations of the structures and photophysical properties of azaindole and its hydrogen and van der Waals bound clusters range back to the early 80s of the last century. Fuke *et al.*[163] measured mass-resolved ionization spectra and fluorescence excitation spectra of 7-azaindole, 7-azaindole$(H_2O)_{1,2}$ and (7-azaindole)$_2$. From the large spectral red shift (1285 cm^{-1}) they proposed a considerable distortion of the geometry upon electronic excitation of the water clusters.

Kim and Bernstein[164] presented mass-resolved excitation spectra of 7-azaindole and its clusters with Ar, CH_4, NH_3, H_2O, D_2O, CH_3OH, and C_2H_5OH. For the azaindole-water cluster they deduced a structure in which the water moiety is bound to the π-system instead of a hydrogen bonded structure.

Nakajima *et al.*[165] investigated the geometric structures of 7-azaindole$(H_2O)_{1-3}$ and of the 7-azaindole dimer using laser-induced fluorescence spectroscopy with high resolution (~ 0.01 cm^{-1}, equivalent to 300 MHz). They deduced a planar ring structure of 7-azaindole$(H_2O)_1$ from the rotational analysis of the spectrum and from *ab initio* calculations. For the n=2 and 3 clusters also cyclic hydrogen bonded ring structures with the water oxygen atoms in the aromatic plane were suggested.

In the group of Castleman pump-probe experiments have been performed on the n=2, 3, and 4 water clusters of azaindole, which for the doubly and triply hydrated clusters yielded biexponential decays with a short component (a few hundred fs) and a long component (6 ps). They attributed this behavior to a stepwise proton transfer from the $1H$ to the $7H$ position in the n=2 and 3 cluster, while a single exponential decay for the n=4 cluster was believed to be the signature of a concerted proton transfer.[166]

Yokoyama *et al.* performed IR-UV double resonance spectroscopy on 7-azaindole water clusters together with *ab initio* molecular orbital calculations.[167] From their results hydrogen bonded single ring structures for the 7-azaindole$(H_2O)_n$ with n=1 - 3 clusters were deduced in the electronic ground state.

The structural changes of the 7-azaindole$(H_2O)_1$ cluster upon electronic excitation were determined from a Franck-Condon analysis of the emission spectra obtained via pumping of several vibronic bands.[168] The lengths of both the $O \cdots H$ and the $H \cdots N$ hydrogen bond were found to decrease upon electronic excitation, accompanied by a distortion of the monomer geometry.

Dispersed fluorescence spectra of 7-azaindole$(H_2O)_{1-3}$ clusters were presented by Hara *et al.*.[169] No visible emission from the proton transferred tautomers could be observed in their experiment, excluding the possibility that excited state proton transfer (ESPT) takes place in the gas phase on a time-scale comparable to the fluorescence life time.

The geometrical changes of the 7-azaindole monomer itself were investigated using rotationally resolved electronic spectroscopy of four different isotopomers of 7-azaindole[170,171] as well as a Franck-Condon analysis.[172] The nature of the electronically excited state has been shown by Schmitt *et al.* to be predominantly of L_b-character.[170] Recently, the excited state dipole moment of 7-azaindole has been determined in the group of Pratt from the Stark effect in a rotationally resolved LIF spectrum.[173]

5.2   Methods

The experimental setup for the rotationally resolved laser induced fluorescence is described in detail elsewhere.[58] Briefly, it consists of a ring dye laser (Coherent 899-21) operated with Kiton Red, pumped with 7 W of the frequency doubled output of a diode pumped Yb:YAG disc laser (ELS Versadisk). About 600-700 mW of the fundamental dye laser output is coupled into an external folded ring cavity (Spectra

Physics) for second harmonic generation.

The molecular beam is formed by expanding 7-azaindole heated to 100° C and seeded in 300-700 mbar of argon through a 100 μm hole into the vacuum. The molecular beam machine consists of three differentially pumped vacuum chambers that are connected by two skimmers (1 mm and 3 mm diameter, respectively) in order to reduce the Doppler width to 25 MHz. The molecular beam is crossed at right angles with the laser beam in the third chamber, 360 mm downstream of the nozzle. The resulting fluorescence is collected perpendicular to the plane defined by the laser and the molecular beam by an imaging optics setup consisting of a concave mirror and two plano-convex lenses. The fluorescence is detected by a UV enhanced photo-multiplier tube whose output is recorded by a PC based photon counter IO card. The relative frequency is determined with a quasi confocal Fabry-Perot interferometer. The absolute frequency was determined by recording the iodine absorption spectrum and comparising the transitions to tabulated lines.[108]

5.3 Results and Discussion

5.3.1 7-Azaindole(H$_2$O)$_1$

Figure 5.1 shows the rotationally resolved spectrum of the electronic origin of 7-azaindole-(H$_2$O)$_1$. The spectrum spans about 60 GHz and displays a well resolved rovibronic structure of predominantly *ab*-hybrid type.

The molecular parameters obtained from a genetic algorithm (GA) based automated fit of the spectrum are given in Table 5.1, and are compared to the results of various *ab initio* calculations for both electronic states. For details about the fitting procedure using the GA technique see previous work.[18,19,116] Although, as in the case of the azaindole monomer[170] a simple rigid rotor Hamiltonian without axis reorientation was employed, all intensities and line positions are well reproduced (cf. Figure 5.1). The slightly negative inertial defect ΔI and the negligible change of ΔI upon electronic excitation ($\Delta\Delta I$) point to nearly planar structures with at most one hydrogen atom pointing out of the molecular plane in both electronic states. The transition dipole moment, determined from the relative intensities of *a*- and *b*-lines in the spectrum, makes an angle of ± 27 ° with the inertial *a* axis, slightly different from the value, which has been obtained from a fit to the rovibronic contour (± 16 °) taken at much lower resolution (300 MHz).[168] The polar angle ϕ, which introduces *c*-type character in the vibronic band, was determined to be ± 86 °, meaning less than 1% *c*-type. Thus, the transition dipole moment is located in the plane of the chromophore. For the discussion of the sign of the TDM angle θ cf. section 5.3.5. The lineshape was fit to a Voigt profile with a Doppler contribution of 25 MHz, resulting in a Lorentz contribution of 15 ± 4 MHz.

The agreement between the experimental and computed rotational constants in both electronic states is very good for the time dependent density functional theory and the correlated coupled cluster RICC2/TZVP *ab initio* calculations from Svartsov and Schmitt[162] which are also given in Table 5.1 for comparison. The complete active space CAS(10,9)/cc-pVDZ calculations[168] agree well in the electronic ground state, but even the signs of the changes of the rotational constants upon electronic excitation

are predicted wrongly for all rotational constants at this level of theory. The rotational constants reported for DFT/MRCI calculations are the ones of the relaxed RICC2 geometry, at which DFT/MRCI has been performed.[162]

The transition properties like excitation energies and transition dipole moments are quite satisfactorily reproduced with RICC2/TZVP and even better at the DFT/MRCI level, while the CASSCF calculations predict the band type completely wrong, as well as the adiabatic excitation energy, which is off by nearly 4000 cm^{-1}.
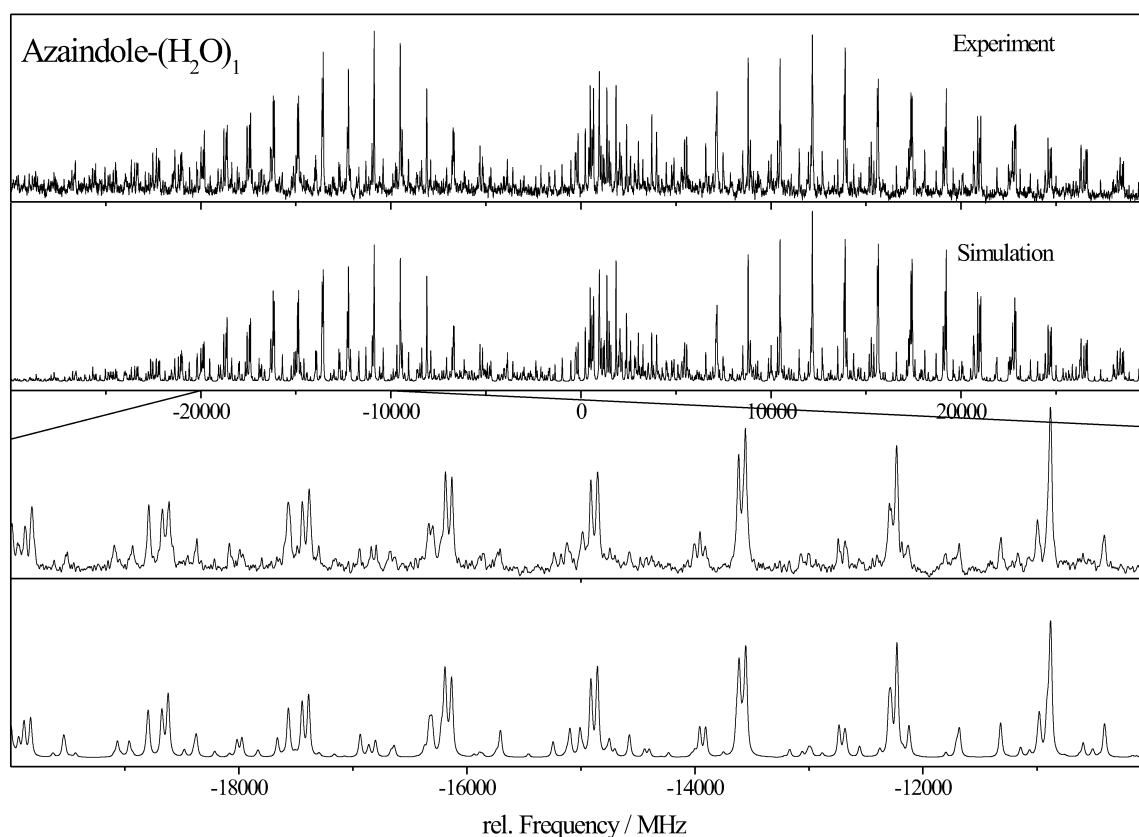
Figure 5.1: Rotationally resolved spectrum of the electronic origin of the 7-azaindole-$(H_2O)_1$ water cluster and simulation of the spectrum using the molecular parameters from the best GA fit, given in Table 5.1. The lower two traces show an expanded view in the range -20000 to -10000 MHz relative to the electronic origin.

5.3.2   7-Azaindole$(H_2O)_2$

Due to the large oscillator strength of transitions to the lowest electronically excited state of 7-azaindole, and the large stability of the hydrogen bonded water clusters, also higher water clusters can be observed with rotationally resolved electronic spectroscopy. Figure 5.2 shows the spectrum of the electronic origin of the 7-Azaindole$(H_2O)_2$ cluster. In contrast to the case of the 1:1 cluster, the spectrum of the 1:2 cluster consists of two closely spaced components with a splitting of 29469 MHz, which can easily be determined from an auto-correlation of the spectrum. The spectrum has been fit using a rigid rotor Hamiltonian without axis reorientation for each of the components using the GA technique, as for the 1:1 water cluster.

Table 5.1: Comparison of the molecular parameters from the fit of the rotationally resolved electronic spectrum of 7-azaindole$(H_2O)_1$ shown in Figure 5.1 to the results of *ab initio* calculations. (TD)DFT and RICC2 calculations were performed with the TZVP basis. For details of the DFT/MRCI calculations cf. Svartsov and Schmitt.[162]

	Exp.	(TD)B3-LYP[a]	RICC2[a]	DFT/MRCI[a]	CAS(10,9)[b]
A'' / MHz	1761.75	1775	1784	1784[c]	1780
B'' / MHz	1342.80	1349	1353	1353[c]	1288
C'' / MHz	762.89	768	771	771[c]	749
ΔI / amu Å^2	-0.77	-1.31	-1.04	-1.04	-1.56
θ / °	±27	-17	-3	+19	-89
ϕ / °	±86	+90	+90	+89	+90
μ_a^2	0.777	0.914	0.995	0.896	0.000
μ_b^2	0.217	0.085	0.005	0.104	1.000
μ_c^2	0.006	0.000	0.000	0.000	0.000
ν_0 / cm^{-1}	33340.43	32360	33288	33214	37320
ΔA / MHz	35.97	25	35	35	-13[c]
ΔB / MHz	15.34	15	14	14	-22[c]
ΔC / MHz	11.80	9	11	11	-10[c]
$\Delta\Delta I$ / amu Å^2	-0.09	0.45	-0.15	-0.15	0.23

[a] Svartsov and Schmitt[162]

[b] Brause *et al.*[168]

[c] Structure used for the DFT/MRCI calculations is the RICC2/TZVP relaxed structure

The rotational constants for both electronic states are given in Table 5.2 and are compared to the results of *ab initio* calculations. The agreement with the results of the time dependent DFT and the RICC2 calculations is as satisfying as for the n = 1 cluster. The considerably larger inertial defect in both electronic states points to a slightly out-of-plane geometry for at least one of the heavy atoms. Comparison with the calculated structures shows that the oxygen atoms of both water moieties in the hydrogen bond chain are slightly out of plane - one being below, the other above the aromatic plane.

As can already be inferred from the strong and unusually sharp correlation side peak at a shift of 29469 MHz relative to the unshifted auto-correlation, the rotational constants of the two subbands are very similar, cf. Table 5.2. The nature of the large amplitude motion which is responsible for the splitting in the spectrum will be investigated in detail in section 5.3.7.

The characteristics of the electronic excitation (adiabatic excitation energy and orientation of the transition dipole moment) are again well reproduced at the DFT/M-RCI level of theory. The angle θ between the TDM and the *a*-axis is determined to be ±34 ° from the intensities in the experimental spectrum and predicted to be +33.7 ° by the DFT/MRCI calculations.

As for the 7-azaindole$(H_2O)_1$ cluster the lineshape was fit to a Voigt profile with a Doppler contribution of 25 MHz, resulting in a Lorentz contribution of 15 ± 6 MHz.

5.3.3 Determination of the cluster structures

The partial intermolecular structures of the n=1, 2 clusters have been determined from the rotational constants given in Tables 5.1 and 5.2 using the program *pKrFit*.[24,121]
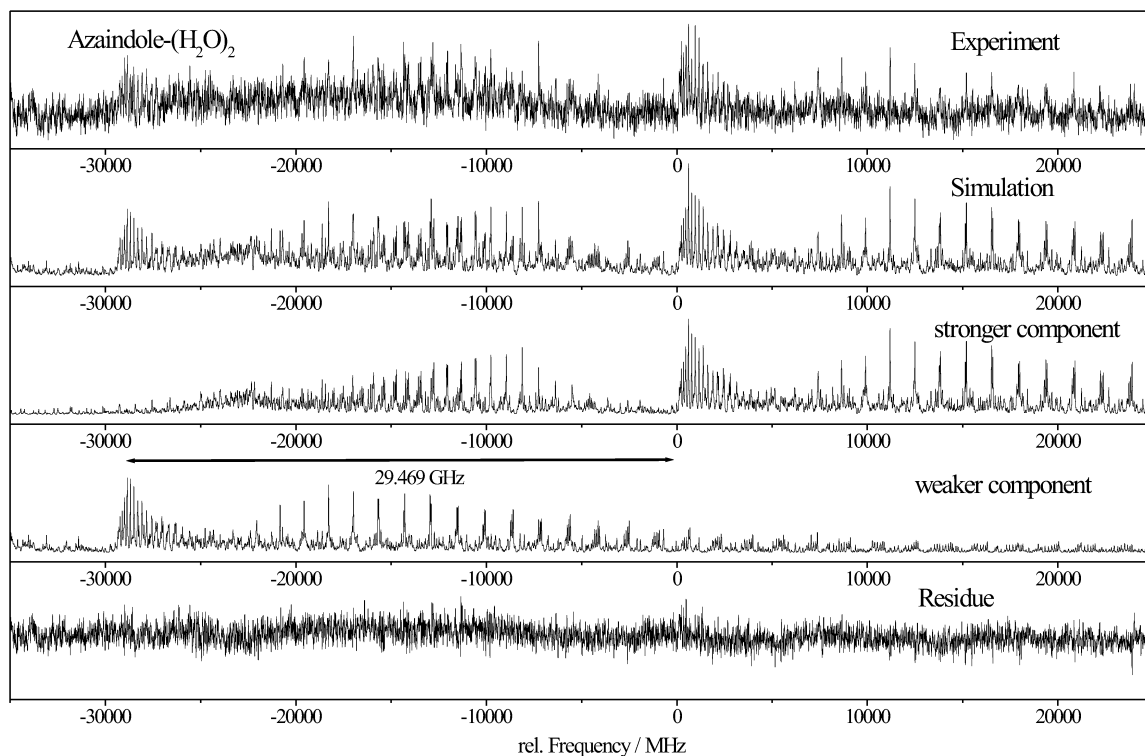
Figure 5.2: Rotationally resolved spectrum of the electronic origin of 7-Azaindole$(H_2O)_2$ and simulation of the spectrum using the molecular parameters from the best GA fit, given in Table 5.2. The last trace shows the residue of the sum of the individual fits of the subcomponents and the experimental spectrum. Frequencies in MHz are given relative to the origin of the stronger component.

Table 5.2: Comparison of the molecular parameters from the fit of the rotationally resolved electronic spectrum of 7-azaindole$(H_2O)_2$ shown in Figure 5.2 to the results of *ab initio* calculations. The (TD)DFT and RICC2 calculations were performed with the TZVP basis. For details of the calculations cf. Svartsov and Schmitt.[162]

	Exp. Band 1	Exp. Band 2	(TD)B3-LYP	RICC2	DFT/MRCI
A'' / MHz	1413.81(25)	1415.46(52)	1424	1425	1425
B'' / MHz	827.61(9)	828.00(18)	856	842	842
C'' / MHz	524.02(5)	524.15(8)	537	533	533
ΔI / amu Å^2	-3.7	-3.2	-5.0	-6.9	-6.9
θ / °	±34	±35	-22	+16	+33.7
ϕ / °	±74	±66	+90	+90	+87.1
μ_a^2	0.6336	0.5594	0.8536	0.9200	0.690
μ_b^2	0.2956	0.2805	0.1463	0.0799	0.307
μ_c^2	0.0708	0.1600	0.0001	0.0001	0.003
ν_0 / cm^{-1}	32632.10	-	32850	29358	32751
$\Delta\nu_0$ / MHz	-	29469	-	-	-
ΔA / MHz	9.35(3)	9.47(2)	+30	+5	+5
ΔB / MHz	27.54(2)	27.38(5)	+31	+28	+28
ΔC / MHz	12.59(2)	12.48(1)	+16	+16	+16
$\Delta\Delta I$ / amu Å^2	-0.6	-0.5	-0.3	-0.7	-0.7

The structure of the 7-azaindole monomer in both electronic states was taken from a combined structural fit to rotational constants of four different isotopomers and to the Franck-Condon intensities of 107 emission bands.[172] The OH distance in the water moiety was set to 96 pm, the water HOH angle to 104 °. Only three geometry parameters could be determined, because for each cluster the rotational constants of only one isotopomer have been measured. For the n=1 cluster the H_1O_8 bond length, the $N_1H_1O_8$ angle and the $N_1H_1O_8H_{8b}$ dihedral angle were chosen. The definitions of the distances, angles, and dihedral angles are given in Figure 5.3. The second hydrogen bond length N_7H_{8a} was not included in the fit, but is obtained implicitly from the definition of the Z-matrix used in the fit. A distinct shortening of both hydrogen bonds upon electronic excitation is found.

Table 5.3: S_0 and S_1 state geometry parameters (r_0) of the 7-azaindole$(H_2O)_{1,2}$ clusters as determined from the fit to the experimental rotational constants. All bond lengths are given in pm, angles and dihedral angles are given in degrees.

	7-AI$(H_2O)_1$			7-AI$(H_2O)_2$	
r_0	S_0	S_1	r_0	S_0	S_1
$H_1O_8{}^a$	215.3	195	$H_1O_8{}^a$	175.2	169.3
$N_1H_1O_8{}^a$	131	127	$H_{8a}O_9{}^a$	170.2	167.9
$N_1H_1O_8H_{8b}{}^a$	139	95	$O_8H_1N_1{}^a$	167	162
N_7H_{8a}	228.1	211.7	$O_9H_{8a}O_8{}^b$	167	162
$N_7H_{8a}O_8$	116	124	$H_{9a}N_7$	214.1	181.8
$H_1O_8H_{8b}$	110	110	$H_{9a}N_7O_9$	156	166

[a] Used in the fit

[b] The angle $O_9H_{8a}O_8$ was kept fixed at the fitted value of $O_8H_1N_1$

Table 5.3 presents the results of the fit. In addition to the three fitted parameters, the other three values which determine the intermolecular geometry are given for completeness.

For the n=2 cluster the restriction of the geometry model due to the small number of inertial parameters is even more dissatisfying. As for the binary cluster, the geometry of the monomer for both electronic states was taken from the Franck-Condon analysis presented by Brause *et al.*[172] Two hydrogen bond distances and the angle which describes the deviation of the $N-H_1 \cdots O_8$ hydrogen bond from linearity were fit. Again, the last hydrogen bond length $H_{9a}N_7$ results automatically from the definition of the internal coordinates. As in the case of the 1:1 cluster, all hydrogen bond lengths decrease upon electronic excitation. Spectra of a much larger number of isotopomers will be necessary to completely unravel the structure of the n=2 cluster in both electronic states in the future.

5.3.4 The structures of the clusters in ground and excited states

Comparison of the measured rotational constants with calculated ones shows that for both the ground state and the excited state the $1H$ tautomer is experimentally observed, although the $7H$ tautomer is found to be considerably more stable in the
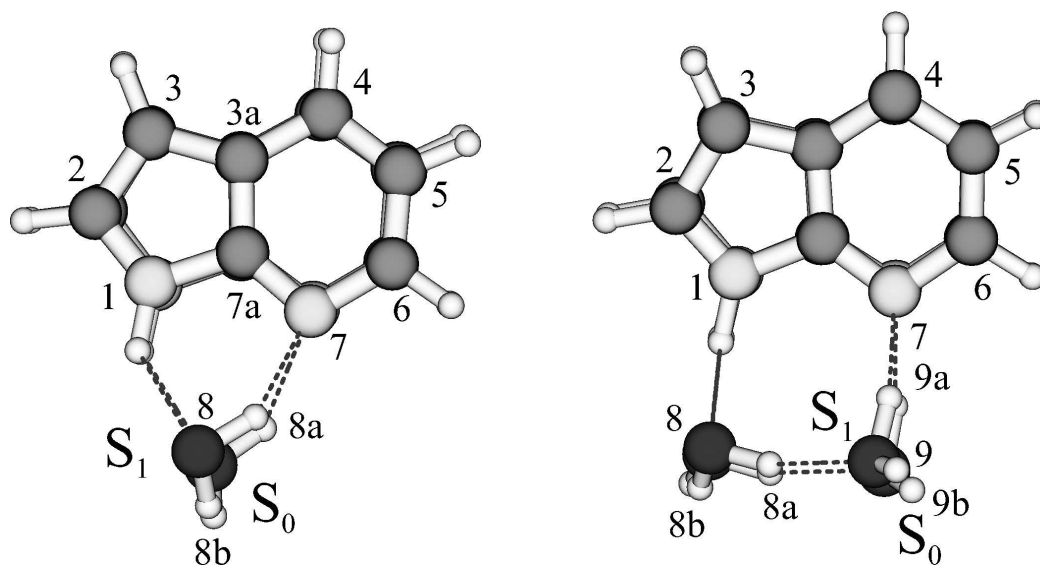
Figure 5.3: Structures of 7-Azaindole$(H_2O)_1$ and 7-Azaindole$(H_2O)_2$ in the ground and first excited singlet state as determined from the fit to the rotational constants. The structures for both states are overlayed, with a maximum of congruence for the azaindole moiety. In each case, the upper structure shows the excited state.

S_1 state. Comparison with the results of RICC2/TZVP calculations[162] shows a large change in the geometry of the azaindole monomer moiety upon water complexation in the electronically excited state, while the ground state geometries of the 7-azaindole monomer and its water cluster are nearly the same. The reason for this strange behavior in the excited state is a solvent induced state reversal between the L_b and L_a state, the former being the S_1 state in the monomer, the latter that in the 1- and 2-water cluster. Of special interest for future experiments will be the determination of selected geometry parameters of the monomer in the cluster, using isotopically substituted species and Kraitchmans equations. These provide direct access to the question of the electronic nature of the excited states.

Both hydrogen bond lengths in the 7-azaindole$(H_2O)_1$ cluster (H_1O_8 and N_7H_{8a}) are considerably shortened upon electronic excitation which can be explained by the increased excited state acidity of the pyrrole moiety and the increased basicity of the pyridine moiety in the first electronically excited $\pi - \pi^*$ state.[174] Figure 5.3 shows the simultaneous decrease of both hydrogen bonds in the excited state.

For the 7-azaindole$(H_2O)_2$ cluster, the H_1O_8 bond length also decreases upon electronic excitation. The hydrogen bond length between the two water moieties $H_{8a}O_9$ decreases slightly, due to polarization effects on both water moieties, mediated by the basicity increase of the pyridino N atom and the increase in acidity of the pyrrolo N(H) site.[175]

5.3.5 Orientation of the transition dipole

The orientation of the transition dipole moment in the 7-azaindole monomer was experimentally determined to be -14°[171] or -20°[170] with respect to the *a*-axis. The minus sign refers to an orientation in which the TDM points in the direction of the

pyrrolic NH group (orientation I in Figure 5.4a). However, DFT/MRCI calculations predict a TDM orientation of $+20°$ (orientation II in Figure 5.4a).[162]

The orientation of the TDM in the water cluster is determined in the present work to be $\pm 27°$ with respect to the a-axis of the cluster. The RICC2/TZVP calculations reported by Svartsov and Schmitt,[162] which reproduce the experimental excited state rotational constants to better than 1%, show that the angle of the inertial a-axis in the cluster with the $C_{3a}C_{7a}$ bond (cf. Figure 5.4) is $30°$. In the monomer the angle between the a-axis and the $C_{3a}C_{7a}$ bond is found to be $90°$. Therefore, the inertial axis system in the frame of the azaindole monomer is rotated counterclockwise by $60°$ upon cluster formation as shown in Figure 5.4. The inertial axes of the monomer and the water clusters are shown with the azaindole monomer moieties oriented equally in Figure 5.4.
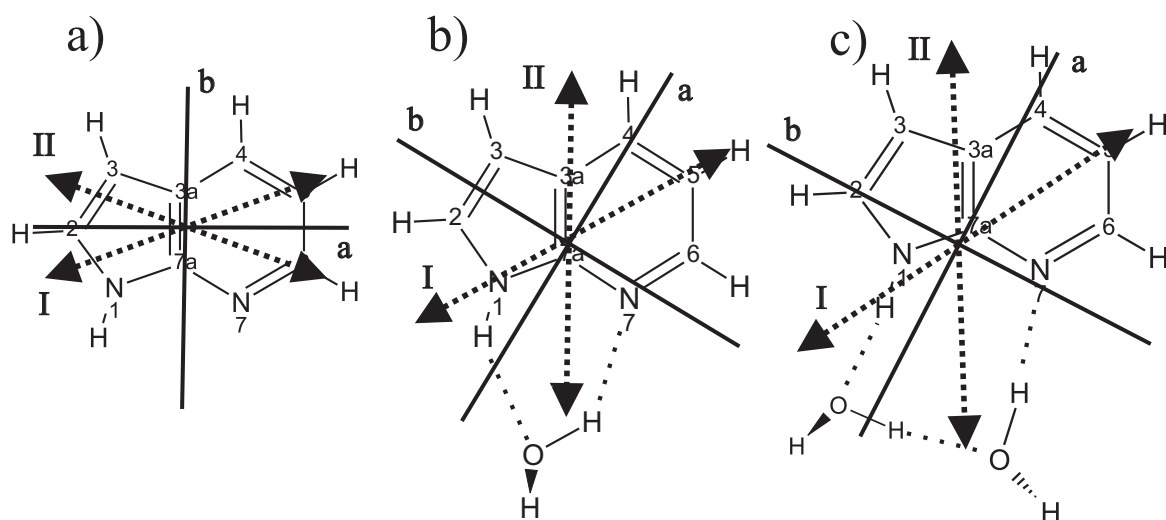
Figure 5.4: Inertial axis systems and TDM orientations of 7-azaindole, 7-azaindole$(H_2O)_1$, and 7-azaindole$(H_2O)_2$.

If the positive sign of the TDM orientation in the n=1 cluster applies, as predicted by the DFT/MRCI calculations, the TDM would make an angle with the a-axis of the monomer of -33° (orientation I in Figure 5.4b). If, on the other hand, the negative sign would apply then the angle of the TDM with the a-axis in the monomer geometry would be 87° (orientation II). This orientation is completely different from both orientations I and II in the 7-azaindole monomer.

For the n=2 cluster the rotation of the inertial axes upon water complexation is calculated from the geometries of the RICC2 calculations to be -70° (cf. Figure 5.4c). The experimentally determined angle of the TDM with the a-axis in the inertial system of the cluster is ± 34 °, while DFT/MRCI calculations predict a value of +35 °, which is in very good numerical agreement. In the inertial system of the monomer, this would correspond to angles of -35° for the + sign (close to orientation I in the monomer) or to 75° for the - sign (different from both orientations I and II). Again, the positive direction gives an orientation, similar to orientation I in the monomer.

Comparison of the experimental rotational constants of the azaindole monomer and the water clusters to the results of the RICC2 calculations for the lowest excited states showed that the excited state of the clusters has a completely different geometry

from that of the monomer, while the ground state geometry is similar.[162] This points to a change in the ordering of the lowest two excited states upon cluster formation.

Summarizing these findings, it appears as if the TDM angle in the monomer should have a positive sign, as predicted by the DFT/MRCI calculations, but in contradiction with previous experiments. Since these experiments were performed independently in two different groups, the reason for this discrepancy is not easily allegeable. Maybe the assumption made in the interpretation, that deuteration leaves the molecule electronically unchanged and rotates only the inertial axes, is not correct.[170,171] If one looks into the theoretical results for the other tautomer of 7-azaindole (the H being at the 7-position instead of the 1-position), the direction of the TDM is reversed between L_a and L_b compared to the "normal" *1H* tautomer. If tunneling between the two positions (N_1 and N_7) is now assumed to occur, the resulting TDM orientation might deviate from that of the pure *1H*-7-azaindole. Since the barrier is high, most of the contribution to the TDM comes from the "normal" tautomer, but a small fraction is induced by the other tautomer. In the case of the deuterated isotopomer tunneling is quenched, and the orientation is governed exclusively by that of the "normal" tautomer. This means that the reason for the change of the angle might be different from what was assumed in both analyses (a pure effect of deuteration on the inertial axes).

5.3.6 Excited state lifetimes

The Voigt profiles of single rovibronic lines in the 7-azaindole$(H_2O)_1$ and 7-azaindole-$(H_2O)_2$ spectra both exhibit Lorentz components of 15 ± 5 MHz. This broadening corresponds to an excited state life time of about 10 ns. This value is considerably larger than the excited state life time in the 7-azaindole monomer of 2.5 ns.[170] Huang *et al.* reported lifetimes of 8.1 ns for 7-azaindole$(H_2O)_1$ and of 6.6 ns for 7-azaindole$(H_2O)_2$ using time-correlated single-photon counting.[176] Folmer *et al.* found a biexponential decay of the 7-azaindole$(H_2O)_2$ excited state with time constants of 360 fs and 6 ps using pump-probe spectroscopy.[166] They suggested that the existence of two different time constants points to a stepwise proton transfer reaction in the excited state. Later Hara *et al.* showed that in the fluorescence emission spectra of the 7-azaindole$(H_2O)_{1-3}$ clusters in a molecular beam no visible fluorescence could be detected on this timescale.[169] From this they concluded that ESPT does not occur on the timescale of direct (resonant) fluorescence emission in the gasphase. The present investigations confirm this conclusion. The much shorter transients, shown in Figure 2 of Folmer *et al.*,[166] are only recorded up to 7 ps. Thus, it is possible that a much longer time component is contained in their transient. By-eye extrapolation of the data in Figure 2 of Folmer *et al.*[166] points to a remaining intensity offset, which might be due to a slow component observed in our cw experiment. Alternatively, the transients which were observed on the different mass channels of the clusters might be contaminated by fragmentation from higher cluster sizes, thus yielding an averaged lifetime of many cluster sizes, including very large ones.

5.3.7 Internal motion in the 7-azaindole(H₂O)₂ cluster

The splitting which is observed in the spectrum of the 7-azaindole(H_2O)$_2$ cluster might be caused by the existence of two different conformers of the cluster, with a small spectral shift due to different zero-point-energy differences. Regarding the fact that the splitting is very small, the chromophore of the two conformers and its close vicinity must be very similar. One possibility for two different conformers in the 7-azaindole(H_2O)$_2$ cluster is shown in Figure 5.5. Here the potential energy is plotted for the tunneling motion, which interchanges the up and down hydrogen atoms in the water chain, projected to a one-dimensional reduced coordinate. The line of view is from the central hydrogen bond ($H_{8a} \cdots O_9$) to the azaindole moiety, oriented as shown in Figure 5.3. The global minimum has an up/down or down/up arrangement of the two H-atoms of the water moieties. From this minimum a transition state is reached in which one of the two hydrogen atoms is in-plane. By further rotation of this H-atom in the same direction a second (local) minimum is reached in which both H-atoms point down(up)wards. Both local minima with the hydrogens pointing both up or both down have the same energy with respect to the the up/down and down/up conformations of the global minimum. The stationary points along this coordinate have been calculated at the RICC2/TZVP level of theory for both electronic states. All energies relative to the global minimum are given at the respective stationary points in Figure 5.5. From the relative energies of the transition states in Figure 5.5 it is clear that the arrangement with the in-plane hydrogen atom at the pyrrolo side has a slightly different energy than that where it is at the pyridino side.

A normal mode analysis at the level of structure optimization has been performed to check the number of imaginary and non-imaginary frequencies for the minima and the transition states. The splitting in the spectrum would then arise from two transitions connecting the global and the local minimum in each electronic state (cf. Figure 5.6a). Since the ground state energy difference between the two conformers amounts only to 285 cm^{-1} (including zero-point-energy correction) and the barrier separating them is calculated to be 372 cm^{-1}, both conformers might be frozen out in the course of the expansion, forming an intensity ratio between the two bands which is governed by the expansion conditions.

If, on the other hand, the most stable conformer is exclusively frozen out in the supersonic expansion, an alternative explanation for the splitting can be given on the basis of a tunneling splitting of the lowest vibrational level in the potential energy curve of Figure 5.5, which differs from the excited state splitting by the absolute value of the observed splitting.

In the following the order of magnitude of the splitting is estimated. Since the energy differences between the various transition states (at least in the electronic ground state) are small, it is possible to approximate the potential by an expansion in cosine terms:

$$V_4 = \frac{1}{2}(V_2(1 - \cos 2\alpha) + V_4(1 - \cos 4\alpha)) \tag{5.1}$$

with V_2 = -290 cm^{-1} and V_4 = +200 cm^{-1} in the electronic ground state.

Using the potential given above and a reduced torsional constant B of 23 cm^{-1}, which is typical for a hydroxy torsion,[120] a ground state torsional level splitting of 0.4
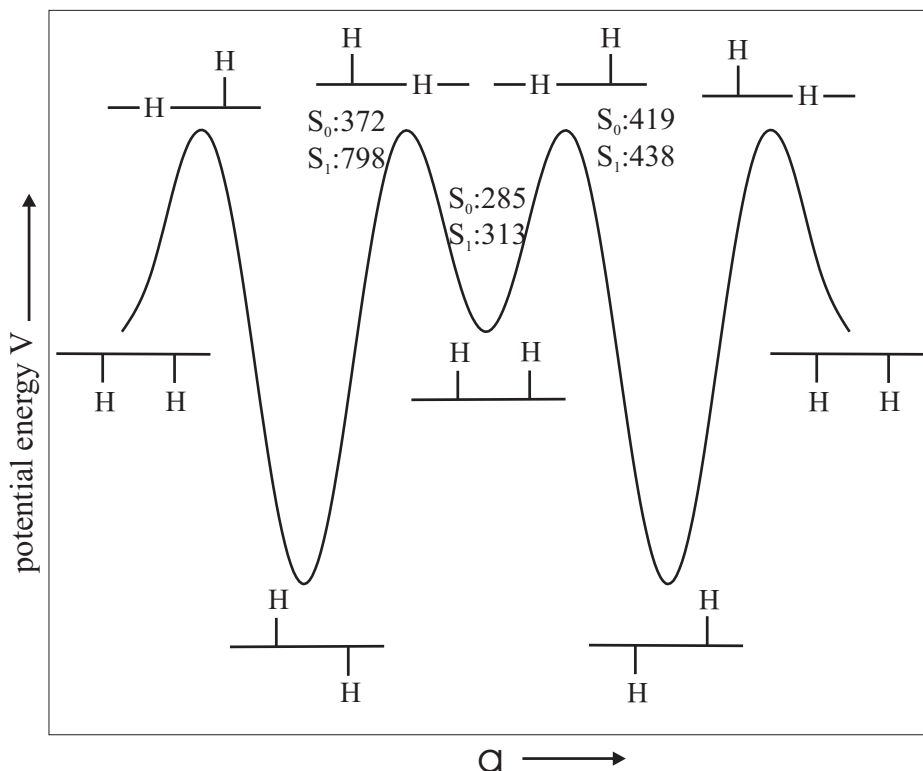
Figure 5.5: One-dimensional potential energy curve of the tunneling coordinate in the 7-Azaindole(H$_2$O)$_2$ cluster. The conformations of the stationary points have been depicted symbolically with the line of sight into the plane of the hydrogen bond ring and the azaindole monomer. The two out-of-plane hydrogen atoms are labeled 8b and 9b in Figure 5.3. All energies are in cm^{-1}.

cm^{-1} is obtained using the analytical solutions from Lewis *et al.*[177] of the Schrödinger equation with the Hamiltonian:

$$H_T = B\frac{d^2}{d\alpha^2} + \frac{1}{2}\sum_n V_n(1 - \cos n\alpha) \tag{5.2}$$

as implemented in the program *HTorFit*, which was described by Jacoby and Schmitt.[178] For the excited state a negligible splitting results due to the much higher barrier. Therefore, the very crude approximation that the potential in the excited state is also approximated by a sum of cosine terms does not influence the result.

The two possible explanations for the splitting of the electronic origin of the 7-azaindole(H$_2$O)$_2$ cluster are depicted in Figure 5.6. Making a distinction between these two possibilities seems to be difficult. In case b), the relative intensities of the subbands will only depend on the spin statistical weights of the two components but not on the expansion conditions, since both transitions originate from the same ground state potential energy minimum. In case a) the expansion conditions should alter the relative intensities. In none of the experiments we performed a change of the relative intensities could be observed, which would point to case b). Nevertheless, the range over which the expansion conditions can be varied without losing the signal is quite small for the 7-Azaindole(H$_2$O)$_2$ cluster. Thus, at the present moment, no definite answer can be given to this question. Given the small chance that the difference of two
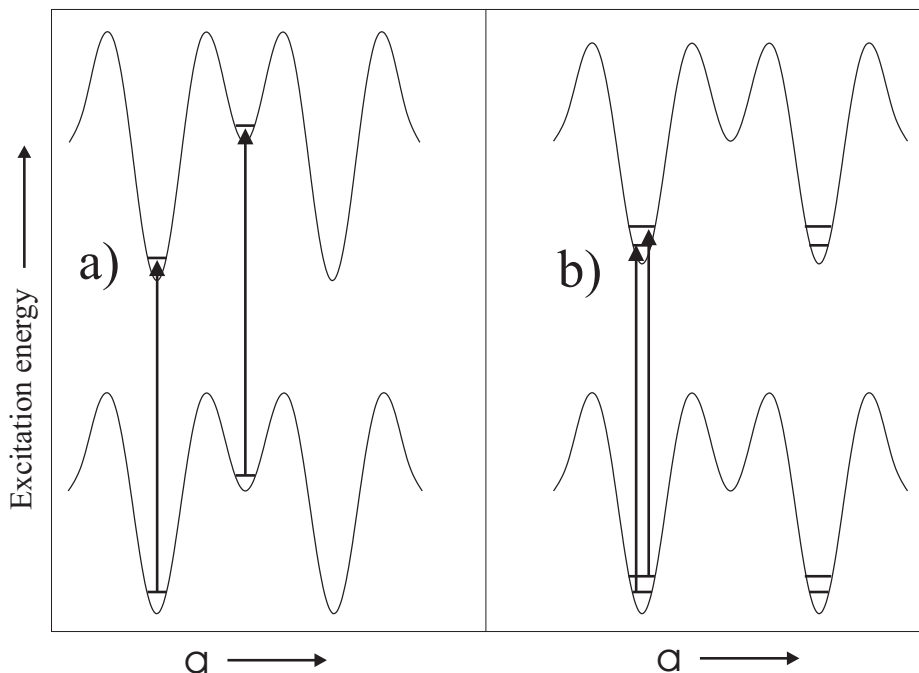
Figure 5.6: Energy level scheme for the possible transitions in 7-Azaindole$(H_2O)_2$.
a) Transitions between different conformers. The assumption is made that under
the expansion conditions both conformers are frozen out simultaneously. b) Transitions between different tunneling components of the most stable conformer, which
in this model is frozen out exclusively in the supersonic expansion.

excitations originating from different minima on the potential energy surface shown
in Figure 5.6a is as small as observed experimentally we strongly prefer the tunneling
model (case b).

5.4 Conclusions

The structures of the 7-azaindole$(H_2O)_{1,2}$ clusters were determined in the S_0 and the
S_1 state. Both in the ground and excited state cyclic hydrogen bonded clusters of the
1H tautomer were found, although in the excited state the *7H* tautomer is the more
stable one. Of course this is not in the Franck-Condon region for transitions from the
1H ground state.

Contrary to the case of the 7-azaindole monomer the S_1 state in the microsolvated
clusters is found to be of L_a character in Platts nomenclature (HOMO $\rightarrow$ LUMO).
This conclusion can be drawn on the basis of the excited state structures, the transition
dipole moment orientations and the adiabatic excitation energies.

The increased acidity of the pyrrolic NH group and the increased basicity of the
pyridino N atom in the electronically excited state leads to a considerable shortening
of both hydrogen bonds in the cyclic 7-azaindole$(H_2O)_1$ cluster.

Excited state lifetimes of 10 ns have been determined from the Lorentz contribution
to the line profiles for both clusters, which are orders of magnitude larger that the
two time constants for a biexponential decay that has been measured by pump-probe
spectroscopy.

The spectral splitting observed in the 7-azaindole$(H_2O)_2$ cluster can be explained on the basis of a tunneling motion which interconverts the two out-of-plane hydrogen atoms of the water molecules.

Electronic excitation in the phenol dimer: The intermolecular structure in the S_0 and S_1 state determined by rotationally resolved electronic spectroscopy

The rotationally resolved UV spectra of the electronic origins of five isotopomers of the phenol dimer have been measured. The complex spectra were analyzed using a genetic algorithm based fitting strategy. From the inertial parameters, the intermolecular geometry parameters were determined for both electronic states and compared to the results of *ab initio* calculations. In the electronic ground state a larger hydrogen bond length than in the *ab initio* calculations is found and a smaller tilt angle of the aromatic rings, showing a more pronounced dispersion interaction. In the electronically excited state the hydrogen bond length decreases, as has been found for other hydrogen bonded clusters of phenol, and the two aromatic rings are tilted less toward each other.

6.1   Introduction

The phenol dimer is an ideal model system to study the very sensitive equilibrium between hydrogen bonding and dispersion interaction. The spectroscopy of complexes of phenol with different solvent molecules has been the subject of a plethora of publications in the last decades. In most of these complexes phenol acts as a proton donor with respect to the solvent molecule, due to its acidic character. Phenol in its electronically excited state is a much stronger acid than in the ground state. $(pK_s(S_1) = 6;$ $pK_s(S_0) = 9.8)$.[179] The phenol dimer takes a special position, since one of the cluster constituents acts as proton donor, the other as proton acceptor. Dispersive interactions between the aromatic rings are likely to play an important role for the structure, while for most of the other phenol-X clusters (X=H_2O[24,120,124,180–190], CH_3OH[58,191,192], N_2[79,87,93,99,109,193], NH_3[194–203], CO[193,204]) the hydrogen bond is the main structure determining parameter. Exceptions here are of course clusters of phenol with noble gases[18,205] or with CH_4[206] which are stabilized by pure van der Waals interactions.

The first multiphoton ionization spectrum of the phenol dimer in a molecular beam was presented by Fuke and Kaya.[207] Later, the same authors showed that the electronic origin of the donor moiety is redshifted by 303 cm^{-1} relative to the origin of bare phenol, while the acceptor origin is blueshifted by 353 cm^{-1}.[208] Only the donor moiety of the dimer fluoresces, while the acceptor moiety could only be detected via ionization[209] or hole burning schemes.[210] The electronic ground state has been investigated using dispersed fluorescence spectroscopy after excitation of the donor moiety. The intermolecular stretching vibration in the electronic ground state (109 cm^{-1}) and in the excited state of the donor (120 cm^{-1}) and the acceptor (106 cm^{-1}) have been found to be very similar. Hartland *et al.* performed Ionization-Loss Stimulated Raman Spectroscopy and discussed the observed vibrational frequency shifts for both donor and acceptor phenol in terms of the strength of the hydrogen bond.[86] The fluorescence lifetime of the donor moiety was determined to be 16 ns by Sur and Johnson using pump-probe photoionization.[181] Felker[211] and Connell *et al.*[71] determined the rotational constants of the phenol dimer using rotational coherence spectroscopy (RCS). As a consequence of the low temporal resolution of their experiment, the rotational constants reported by them are averaged over ground and electronically excited state constants and no information on the geometry change upon electronic excitation was obtained. Later Weichert *et al.*[212] performed an RCS experiment on the dimer with higher resolution and were able to extract the rotational constants of ground and excited state separately. Hobza *et al.*[213] performed *ab initio* calculations on the RI-MP2/TZVPP level of theory and found good agreement with the experimental inertial parameters from Weichert *et al.*[212] IR-UV double-resonance spectroscopy and stimulated Raman-UV double-resonance spectra of the phenol dimer were published by Ebata *et al.*[214] For the dimer, they found that the IR intensity of the OH stretching vibration of the donor moiety is four times larger than that of the acceptor moiety. Ebata *et al.* investigated IVR from OH stretching vibrations of the phenol dimer using picosecond IR-UV pump-probe spectroscopy.[215] They found a strong site-dependence of the IVR rate. IVR of the donor site was found to occur much faster (5 ps) than of the acceptor site (14 ps).

Prior to the determination of the cluster structure, the geometries of the constituents have to be known as exactly as possible. Phenol in the electronic ground state has been thoroughly investigated by microwave spectroscopy and a complete Kraitchman structure has been deduced by Larsen.[216] Christoffersen *et al.* calculated a shortening of the CO bond of 4.4 pm and an increase in the $C_6C_1C_2$ angle (cf. Figure 6.1) of 3.7° upon excitation using rotational constants obtained from a band contour analysis.[217] Ratzer *et al.* determined the structure of phenol in the S_1 state by a fit to the rotational constants of 12 isotopomers, which were obtained from rotationally resolved UV-spectroscopy.[24]

In the present paper the intermolecular geometry of the phenol dimer will be elucidated in both the S_0 and the S_1 state on the basis of rotational constants of five isotopomers. The first rotationally resolved electronic spectrum of the phenol dimer was measured as early as 1995 by us. Nevertheless, at that time we were not able to extract the molecular constants from the spectra using the classical line position assigned fitting procedure. Since then, we have made great progress in the automated fitting of very complex spectra using a genetic algorithm (GA) approach. An additional motivation to show the extreme power of this method in combination with

rotationally resolved electronic spectroscopy is a statement made in a recent publication on the phenol dimer:[213] "The RCS technique is complementary to frequency-resolved spectroscopic techniques since it can be successfully applied to large systems, where the latter techniques are not applicable due to overlapping resonances. The phenol dimer is such an example, since until now the frequency spectra could not be assigned." In the following it will be shown that this statement has become obsolete by the development of the GA based fitting strategy.

6.2 Methods

6.2.1 Experimental procedures

The experimental setup for the rotationally resolved laser induced fluorescence (LIF) is described in detail elsewhere.[58] Briefly, it consists of a ring dye laser (Coherent 899-21) operated with Rhodamine 110, pumped with 6 W of the 514 nm line of an Ar^+-ion laser. The light is coupled into an external folded ring cavity (Spectra Physics) for second harmonic generation (SHG). The molecular beam is formed by expanding phenol (or the respective isotopomers) heated to 160°C and seeded in 700 mbar of argon through a 100 μm hole into the vacuum. The atomic numbering for phenol used in this publication is given in Figure 6.1. h_6-phenol (99.5%) was purchased by Riedel de Haen and used without further purification. [7–D]phenol (d_1) has been prepared by refluxing dried h_6-phenol three times with an excess of D_2O (Merck, isotopic purity > 98.8 %) and subsequent removal of water. Isotopic purity of the sample was higher than 95 %. The samples of d_6-phenol (isotopic purity 99%) and 1-^{13}C-phenol (isotopic purity > 99%) were purchased from Chemotrade and used without further purification.
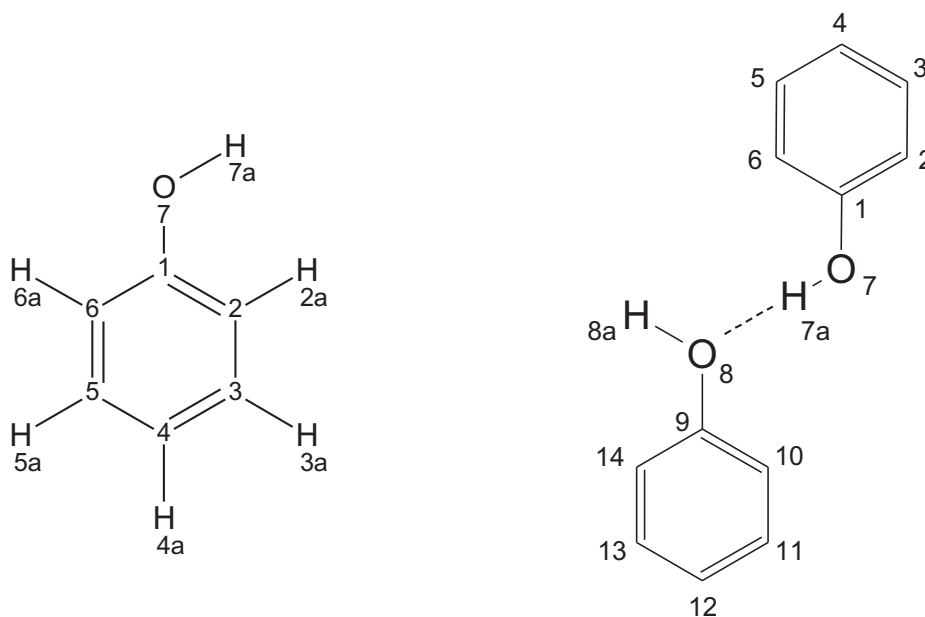
Figure 6.1: Atomic numbering of phenol and the phenol dimer used here. Both monomer moieties of the dimer are drawn planar for reasons of clarity. This does not bear any relation to the true structure.

The molecular beam machine consists of three differentially pumped vacuum chambers that are linearly connected by two skimmers (1 mm and 3 mm diameter, respectively) in order to reduce the Doppler width. The molecular beam is crossed at right angles with the laser beam in the third chamber, 360 mm downstream of the nozzle. The resulting fluorescence is collected perpendicular to the plane defined by the laser and the molecular beam by an imaging optics setup consisting of a concave mirror and two plano-convex lenses. The resulting Doppler width in this setup is 25 MHz (FWHM). The integrated molecular fluorescence is detected by a photo-multiplier tube whose output is discriminated and digitized by a photon counter and transmitted to a PC for data recording and processing. The relative frequency is determined with a quasi confocal Fabry-Perot interferometer with a free spectral range (FSR) of 149.9434(56) MHz. The absolute frequency is determined by recording the iodine absorption spectrum and comparing the transitions to tabulated lines.[108]

6.2.2   Genetic algorithms

An automated fitting procedure was used for the rovibronic spectra, based on a genetic algorithm fit which is described in detail in previous work.[17,18] The GA library PGA-Pack version 1.0 was used, which can run on parallel processors.[218] For the simulation of the rovibronic spectra a rigid asymmetric rotor Hamiltonian was employed:[219]

$$H = AP_a^2 + BP_b^2 + CP_c^2. \tag{6.1}$$

Here, the $P_g(g = a, b, c)$ are the components of the body-fixed angular momentum operator, and A, B and C are the three rotational constants. The temperature dependence of the intensity is described by a two temperature model:[119]

$$n(E, T_1, T_2, w) = e^{-E/kT_1} + we^{-E/kT_2}, \tag{6.2}$$

where E is the energy of the lower state, k is the Boltzmann constant, w is a weighting factor and T_1 and T_2 are the two temperatures. The calculations were performed on 64 processors (Intel Itanium 2, 1.3 GHz) of an SGI Altix 3700 system and on 64 processors (Intel Xeon processors, 3.4 GHz) of a Linux cluster. The genetic algorithm copies concepts from evolutionary processes like sexual reproduction, selection, and mutation. For a detailed description of the GA as fitting algorithms the reader is referred to the original literature on evolutionary or genetic algorithms.[113–115]

The cost function used to describe the quality of the fit is defined as $C_{fg} = 100(1 - F_{fg})$, with the fitness function F_{fg}:

$$F_{fg} = \frac{(\boldsymbol{f}, \boldsymbol{g})}{\|\boldsymbol{f}\| \, \|\boldsymbol{g}\|}. \tag{6.3}$$

$\boldsymbol{f}$ and $\boldsymbol{g}$ represent the experimental and calculated spectra, respectively and the inner product $(\boldsymbol{f}, \boldsymbol{g})$ is defined with the metric $\boldsymbol{W}$ which has the matrix elements $W_{ij} = w(|j - i|) = w(r)$ as:

$$(\boldsymbol{f}, \boldsymbol{g}) = \boldsymbol{f}^T \boldsymbol{W} \boldsymbol{g}, \tag{6.4}$$

and the norm of $\boldsymbol{f}$ is defined as $\|\boldsymbol{f}\| = \sqrt{(\boldsymbol{f}, \boldsymbol{f})}$ and similar for $\boldsymbol{g}$. For $w(r)$ a triangle function was used[17] with a base width Δw:

$$w(r) = \begin{cases} 1 - |r| / \left(\frac{1}{2}\Delta w\right) & \text{for } |r| \leqslant \frac{1}{2}\Delta w \\ 0 & \text{otherwise.} \end{cases} \tag{6.5}$$

In the first iterations, the value of Δw is chosen to be about five times the linewidth in the spectrum. The final fit with a strongly narrowed search space for each parameter is performed using a base width of zero.

6.3 Results and Discussion

Figure 6.2 shows the rovibronic spectrum of the electronic origin of the phenol dimer together with the best GA fit using the molecular parameters from Table 6.1. The lowest trace shows an enlarged part of the convoluted simulation along with the stick spectrum. What appear to be single lines in the spectrum are essentially clusters of up to 15 lines which contribute with similar intensities. In this example the usefulness or even the indispensability of the GA based fitting strategy in the automated assignment of such a congested spectrum is obvious. Given the enormous density of rovibronic lines, a classical assignment procedure seems to be hopeless or at least incredibly tedious.

The spectrum is fit using a rigid rotor Hamiltonian with a two temperature model. It is of mixed *abc*-type and consists of about 13000 lines in a range of 50 GHz. At a rotational temperature of about 5 K more than 100 J states are populated with an intensity of at least 0.5 % of the strongest transition in the spectrum. The rotational constants for both electronic states, the origin frequencies, the polar angles defining the orientation of the transition dipole moment in the inertial frame, and the Lorentzian contribution to a Voigt profile with 25 MHz Gaussian are given in Table 6.1.

Figure 6.3 shows the rovibronic spectrum of the doubly deuterated dimer $(d_1 - d_1)$. Deuteration positions are 7a and 8a (cf. Figure 6.1). Due to incomplete deuteration an additional weak band shows up, which can be assigned to a singly deuterated isotopomer, either in 7a (donor) or in 8a (acceptor) position. In principle, there should also be the differently monodeuterated counterpart, but despite intense scanning an additional band was not found. The second trace of Figure 6.3 shows the overall result of the GA fit, the lower two traces show the individual fits of the two isotopomers. The molecular parameters of the fit are summarized in Table 6.1.

Since the deuterations in the mono- and bideuterated isotopomer take place close to the b and c inertial axes their effect on the B and C rotational constants is small. Another isotopomer in which a much more pronounced effect on all rotational constants can be observed is the fully deuterated $d_6 - d_6$ isotopomer. The rovibronic spectrum of the electronic origin at 36217.50 cm^{-1}, along with the best fit, is shown in Figure 6.4. The lowest trace also includes the stick spectrum, which even more than in the case of the $h_6 - h_6$ isotopomer shows the indispensability of the GA for the assignment of such a complex spectrum. The resulting molecular parameters are compiled in Table 6.1. Since it was impossible to find single rovibronic lines in the experimental spectrum, which were needed for an assigned line fit to assess the standard deviation of the parameters, a different scheme for the estimation of the standard
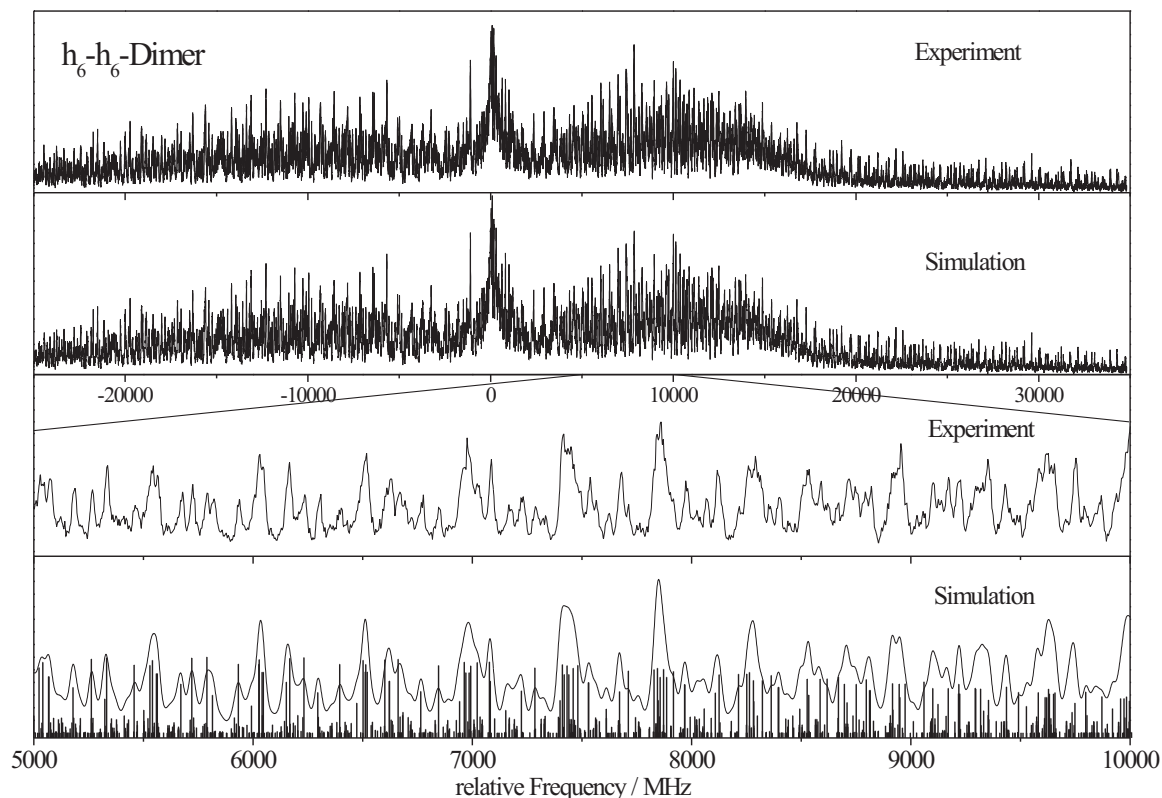
Figure 6.2: Rovibronic spectrum of the electronic origin of the $h_6 - h_6$ isotopomer of the phenol dimer at 36044.70 cm^{-1}. The following traces show the simulated spectrum using the rotational constants from Table 6.1, an enlarged portion of the experimental spectrum and the enlarged simulation together with the stick spectrum.

deviation was employed. The variances and covariances of the fitted parameters were determined from the results of several independent runs of the GA, using different initial seeds.

Figure 6.5 shows the spectrum of the phenol dimer in which the C1 and C9 carbon atoms (cf. Figure 6.1) are replaced by ^{13}C. Since the amount of substance was very small (200 mg 1-^{13}C-phenol) and evaporated quickly through the nozzle, the spectral range covered is smaller than for the other isotopomers.

Comparison of the molecular parameters of the $h_6 - h_6$ isotopomer to the values from the RCS study by Weichert *et al.*[212] shows good agreement for the rotational constants of the electronic ground state, but quite large deviations for the electronically excited state. Nevertheless, given the large uncertainties for the excited state rotational constants from Weichert *et al.*,[212] which were attributed to the fact that no excited-state C'-type transients had been assigned in the RCS spectrum, the excited state constants also agree within these limits. The only systematic difference seems to be in the ground state A rotational constants of the RCS experiment and the present study, which are significantly different outside the quoted uncertainties.

The excited state lifetime of the $h_6 - h_6$ isotopomer is determined to be 16 ± 4 ns from a Lorentzian contribution of 10 ± 3 MHz to the total linewidth. Although this value agrees with the value of Sur and Johnson of 16 ns,[181] which was obtained by
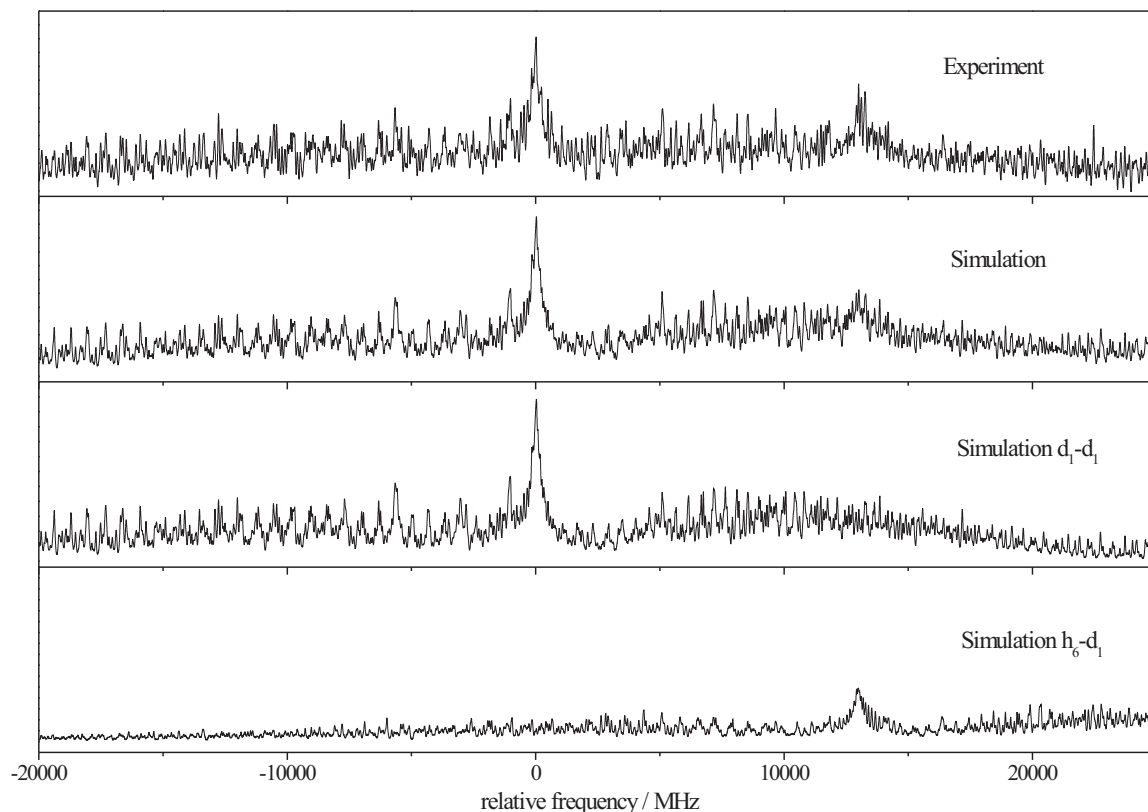
Figure 6.3: Rovibronic spectrum of the electronic origins of the $d_1 - d_1$ and $d_1 - h_6$ isotopomers of the phenol dimer at 36047.56 cm^{-1} and at 36047.98 cm^{-1}.

Table 6.1: Molecular parameters of the electronic origin band of the phenol dimer as obtained from the genetic algorithm fit. The molecular constants from an RCS study[212] are given for comparison; their uncertainties are recalculated as 1σ values for comparison with our results. Rotational constants, their differences, vibronic origins, and Lorentzian full linewidth contributions are given in MHz, angles are given in degrees.

	$h_6 - h_6$	$h_6 - h_6$ (Ref. 212)	$d_1 - d_1$	$d_1 - h_6{}^a$	$d_6 - d_6$	^{13}C-^{13}C
A''	1416.99(39)	1414.4(3)	1376.23(10)	1399.78(124)	1239.33(12)	1413.22(15)
B''	313.51(1)	313.7(4)	312.84(3)	312.72(6)	287.25(1)	311.84(2)
C''	288.11(1)	287.5(4)	286.44(2)	287.16(6)	264.63(1)	286.70(2)
ν_0	36044.70(1)	36044	36047.56(1)	36047.98(1)	36217.50(1)	36045.46(1)
ϕ	58.2(30)	66.9^b	55.2(100)	66.6(23)	58.3(20)	57.4(30)
θ	29.5(30)	37.4^b	35.7(100)	37.6(16)	40.0(35)	35.9(60)
$\Delta_{Lorentz}$	10(3)	-^{c}	10(3)	10(3)	10(3)	10(3)
ΔA	10.71(1)	11.3(12)	4.55(1)	7.81(10)	4.28(2)	10.60(1)
ΔB	$-5.31(1)$	1.6(40)	$-3.95(1)$	$-5.63(1)$	$-3.93(1)$	$-5.25(1)$
ΔC	$-5.82(1)$	$-12.2(35)$	$-4.76(1)$	$-5.99(1)$	$-4.90(1)$	$-5.76(1)$

^{a} Donor moiety deuterated
^{b} Calculated from the alignment of the TDM, given by Weichert *et al.*[212]
^{c} No value given

pump-probe photoionization, it has a much higher uncertainty, which is unusual for the GA based line fit as this fit includes all lines, even if they are overlapping. A closer look at the stick spectra in Figures 6.2 and 6.4 reveals the probable reason for this problem. Since many rovibronic transitions contribute to one line in the experimental spectrum, the slightest deviations of the rotational constants from the true values
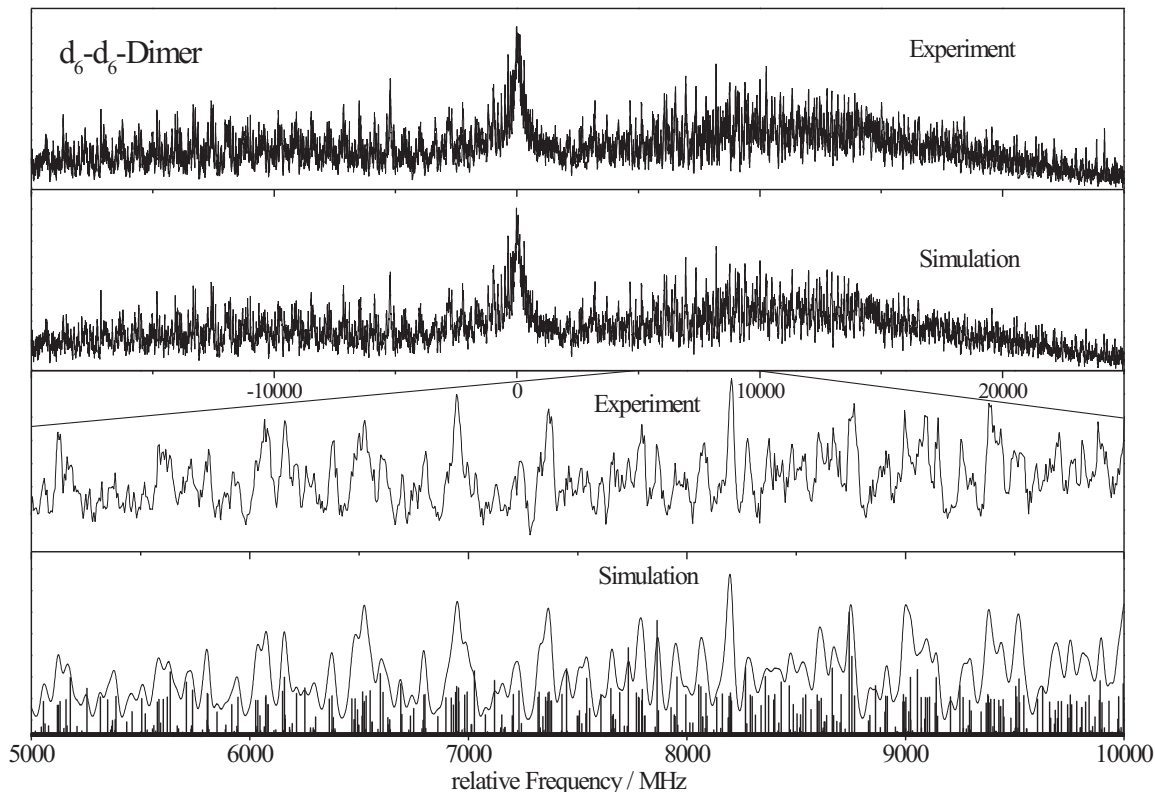
Figure 6.4: Rovibronic spectrum of the electronic origin of the $d_6 - d_6$ isotopomer of the phenol dimer cluster at 36217.50 cm^{-1}.

lead to an apparent broadening or narrowing of the observed lines. In cases where too many transitions overlap to form the observed lines, the determination of the lifetime from a deconvolution of the Voigt profile results in less reliable values for the Lorentzian contribution, thus not allowing for an exact determination of the lifetime.

6.3.1 Determination of the structure

A first approach to the change of the cluster structure upon electronic excitation can be made using the center of mass (COM) distance of the monomer moieties in the cluster as has been shown by Connell *et al.*[71] and later by Weichert *et al.*[212] The COM distance of the two monomer moieties is given by:

$$R = \sqrt{\frac{\sum_g I_g^{Dimer} - \sum_g I_g^{Donor} - \sum_g I_g^{Acceptor}}{2\mu}}, \tag{6.6}$$

where μ is the reduced mass of donor and acceptor, and the I_g are the respective moments of inertia, described by their superscripts, which are calculated from experimentally determined rotational constants. The COM distances for the $h_6 - h_6$ and $d_1 - d_1$ clusters in the ground state were calculated using the same monomer rotational constants for acceptor and donor moiety. They were obtained from a fit of microwave transitions given by Pedersen *et al.*[220] to our rotational Hamiltonian[24] for comparability with the dimer rotational constants. The ground state COM distance
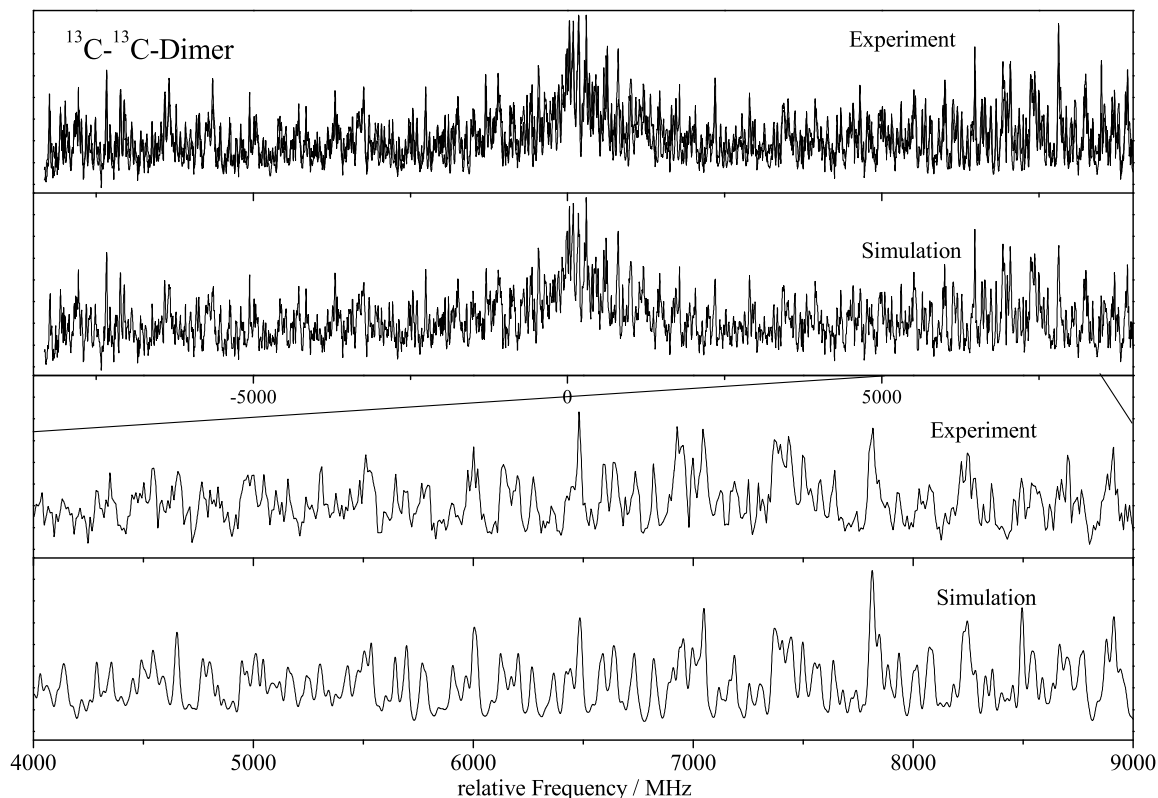
Figure 6.5: Rovibronic spectrum of the electronic origin of the ^{13}C-^{13}C iso-topomer of the phenol dimer cluster at 36045.46 cm^{-1}.

of the $d_6 - d_6$ cluster was calculated using the rotational constants from Ratzer *et al.*,[24] based on the microwave spectra of Forest and Dailey.[221] For the mixed $d_1 - h_6$ cluster the microwave spectra from Pedersen *et al.*[220] and for the ^{13}C-^{13}C dimer those from Larsen[216] were used to evaluate the inertial data. The standard deviations for the COM distances were calculated using the full covariance matrices obtained from the fits of the monomer moieties to the microwave transitions and from the fit of the dimer, described above.

Assuming local excitation in the donor moiety, the COM distance in the electronically excited state can also be calculated. For this calculation the rotational constants of the electronically excited state from high resolution UV spectroscopy of phenol[24] were used for one of the monomer moieties and the ground state rotational constants for the other one. The S$_1$ state rotational constants of the ^{13}C isotopomer have so far not been published.[222] Table 6.2 summarizes the results for the observed isotopomers.

The differences between the COM distances of the different isotopomers can be attributed to the shift of the COM in each of the monomer moieties due to isotopic substitution. In all cases an increase of the COM distance of the monomer moieties upon electronic excitation is found.

The program *pKrFit*[24] was used to determine the intermolecular structure of the phenol dimer in the S$_0$ and S$_1$ states from the rotational constants given in Table 6.1. *pKrFit* uses a gradient-based χ^2 minimizer as well as a GA based global optimizer.[121] While the speed of the gradient method is appealing, the main disadvantage is the possibility of becoming trapped in a local minimum. The GA library[218] was used in

Table 6.2: Center of mass distances (in pm) of the five observed isotopomers of the phenol dimer in the ground and electronically excited state. Standard deviations of the distance differences are typically smaller than those of the individual ones due to high correlations between S_0-state and S_1-state values. The lower three rows give the COM distances that have been calculated from the fitted $pseudo-r_s$ structures in Table 6.3, cf. text.

	$h_6 - h_6$	$d_1 - d_1$	$d_1 - h_6{}^a$	$d_6 - d_6$	^{13}C-^{13}C
S_0	525.126(1)	521.730(19)	523.645(54)	527.0091(77)	523.848(22)
S_1	530.187(5)	525.591(15)	529.000(42)	531.4022(36)	528.871(22)
Δ	5.061(3)	3.861(2)	5.455(10)	4.3931(7)	5.022(4)
$S_0{}^b$	524.99	521.80	523.44	526.91	524.02
$S_1{}^c$	531.85	528.61	530.88	534.31	530.77
$S_1{}^d$	531.64	527.72	529.90	533.27	530.57

^{a} Donor moiety deuterated

^{b} Calculated for the $S_0(r_s)$ structure given in Table 6.3

^{c} Calculated for the $S_1(r_s)$ structure of model I given in Table 6.3

^{d} Calculated for the $S_1(r_s)$ structure of model II given in Table 6.3

minimization mode and thus directly used the correspondingly defined χ^2 value as cost function.

Two different fits of the structural parameters to the rotational constants were performed.[223] The first fit neglects the vibrational contributions from the different isotopomers completely and is based on the assumption:

$$I_g^0 = I_g^e(r_0) \tag{6.7}$$

I_g^0 are the experimentally determined zero-point averaged moments of inertia with respect to the inertial axes g. The functions $I_g^e(r_0)$ are calculated from the structural parameters r_0 using rigid-molecule formulas.

The second method uses a Kraitchman ansatz for individual coordinates in order to obtain the r_s-structure of the molecule.[25,224] The approximation assumes equal vibrational contributions for all isotopomers:

$$I_g^0 = I_g^e(r_s) + \tfrac{1}{2}\epsilon_{0g}. \tag{6.8}$$

The three ϵ_{0g} contain the average vibrational contributions with respect to the inertial axes g. The original Kraitchman method is only applicable to singly or symmetrically substituted isotopomers. In our case the structure is fit to the moments of inertia, given by equation 6.8. The resulting structure is called $pseudo-r_s$-structure. As the three ϵ_{0g} have to be fit, three inertial parameters are lost for the structure determination.

Additional information from the spectra which is used in the fit of the intermolecular dimer structure is contained in the transition dipole moment (TDM) orientations of the different conformers. Since the orientation of the TDM does not change upon isotopic substitution, it is only subject to changes upon rotation of the inertial system. These rotations depend on the structure of the cluster and can be used to improve the fit of the geometry. Although the differences in the orientation angles are small, the structure fit is more stable and the correlations between the parameters are reduced

if the TDM directions of the isotopomers are included in the fit, as has been shown in a recent publication.[121]

The relative orientation of the two phenol moieties can be described by six intermolecular coordinates: One distance of two selected atoms, one from each monomer, two angles, and three dihedral angles, which describe the relative orientation of the monomer moieties. Thus, the 15 rotational constants from five isotopomers are sufficient for the determination of the intermolecular geometry under the assumption of known monomer geometries.

For the determination of the intermolecular cluster structure in the ground state the experimentally determined S_0 monomer structure of Larsen[216] was used for both donor and acceptor phenol. The assumption of unchanged monomer geometries has to be made due to the lack of sufficient data which can be used to fit also the monomer geometries. Nevertheless, in many cases the approximation of unaltered monomer geometries in the cluster has been proven to be reasonably good. The results of the fit of an r_0 and $pseudo - r_s$ structure to the rotational constants is given in Table 6.3. Both structures are very similar, which arises from the fact that the vibrational corrections ϵ_{0g} are small. Two different views of the resulting $pseudo - r_s$ structure are shown in the upper row of Figure 6.6. An additional measure for the quality of the applied model is the comparison of the COM distances that are obtained directly from the moments of inertia of the monomer moieties and the cluster, cf. equation 6.6, with the COM distance calculated for the fitted structures. The respective values are given in Table 6.2. For the electronic ground state the difference is about 0.1 pm, showing the reliabilty of the assumptions made in the course of the fit.

The determination of the S_1 state structure is much more difficult, since the geometry changes in the monomer moieties are not known. First a local fit with the intermolecular geometry of the ground state as starting parameters was performed. The geometries of the monomer moieties in the S_1 state were derived from a CIS/6-311G(d,p) optimized geometry of the cluster. In this fit (model 1 in Table 6.3), the structural parameters of the monomer moieties obtained from the *ab initio* calculations of the cluster were retained, while the six intermolecular geometry parameters were fitted. The COM distances of the different isotopomers of the monomer moieties were calculated from the fitted S_1 state structure, as for the ground state. The deviations from the directly calculated COM distances are larger (typically 2–3 pm, compared to 0.1 pm for the ground state).

An attempt was also made to fit the structure of the dimer in the excited state using the excited state structure of the phenol monomer determined by Ratzer *et al.*[24] for the donor moiety and the unaltered S_0 structure of Larsen[216] for the acceptor moiety. Two approximations were made at this level: The monomer moieties in the cluster are unaltered and the excitation takes place locally in the donor moiety. The first approximation has already been discussed for the ground state geometry. The second one seems to be much more arguable. A purely local excitation in one of the aromatic rings is quite unlikely, since already for the ground state a considerable dispersive interaction has to be considered, which will dramatically change upon electronic excitation of one of the phenol moieties. A local fit of the intermolecular parameters using the model of localized excitation in the donor moiety (model 2 in Table 6.3) leads to a strongly shortened OO hydrogen bond in comparison to the fit using model 1, cf. Table 6.3.

Table 6.3: Comparison of experimentally determined r_0 and r_s geometry parameters of the phenol dimer in the S_0 and S_1 states. All distances are given in pm, angles and dihedral angles in °, pseudo $-r_s$ parameters $\epsilon_{0a,b,c}$ in uÅ². For the fit of the intermolecular structure of the dimer in the S_1 state the monomer geometries from a CIS/6-311G(d,p) calculation of the dimer were used in model 1 and a locally excited donor moiety in model 2. For details see text.

	model 1				model 2	
	$S_0(r_0)$	$S_0(r_s)$	$S_1(r_0)$	$S_1(r_s)$	$S_1(r_0)$	$S_1(r_s)$
r(H$_{7a}$O$_8$)	235.4(49)	236.9(54)	229.3(86)	229.0(87)	174.7(16)	174.4(16)
a(O$_7$H$_{7a}$O$_8$)	150.6(18)	150.5(20)	179.9(10)	179.9(1)	179.9(1)	179.9(1)
a(C$_9$O$_8$H$_{7a}$)	138.6(15)	139.8(14)	104.0(19)	104.1(20)	135.5(8)	135.7(9)
d(O$_8$H$_{7a}$O$_7$C$_1$)	19.6(45)	9.4(47)	46.8(21)	46.9(21)	63.9(9)	63.4(9)
d(C$_9$O$_8$H$_{7a}$O$_7$)	63.5(46)	62.8(46)	−131.4(21)	−131.2(20)	−115.1(9)	−114.8(9)
d(C$_{10}$C$_9$O$_8$H$_{7a}$)	−181.0(19)	−178.2(22)	−104.0(19)	−104.1(29)	−101.6(14)	−101.5(14)
ϵ_{0a}	-	0.0(10)[a]	-	0.0[b]	-	0.0[b]
ϵ_{0b}	-	3.11(13)	-	3.11[b]	-	3.11[b]
ϵ_{0c}	-	1.9(2)	-	1.9[b]	-	1.9[b]

[a] Estimated uncertainty, since fit converged to lower parameter boundary

[b] Fixed to the ground state value
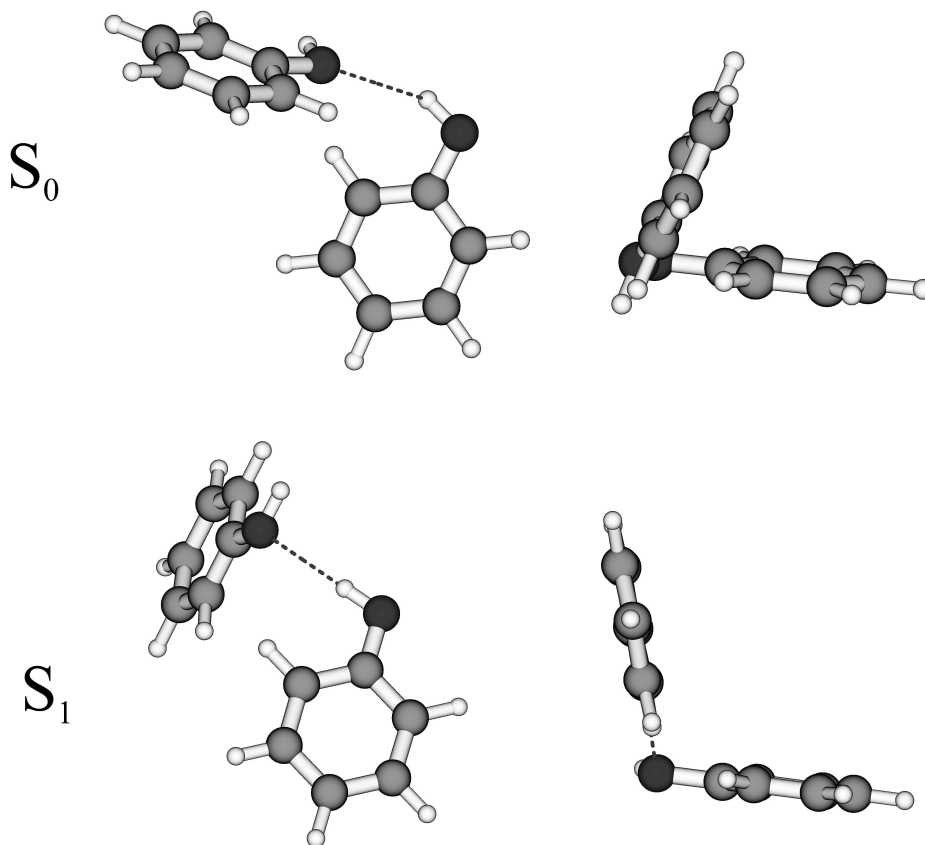
Figure 6.6: Upper row: Two different views of the S_0 (r_s) geometry of the phenol dimer from Table 6.3. Lower row: Same viewing angles for the excited state structure. The depicted geometry is the $pseudo - r_s$ structure of model 1 in Table 6.3.

In the next step a global fit of the intermolecular parameters was tried, as for the ground state. For the excited state geometry minima were found which depend extremely sensitively on the chosen geometry of the monomer moieties and therefore do not lead to stable fits. Furthermore, all geometries obtained with the global fitter show very large changes compared to the ground state. In nearly all cases even the hydrogen bond is broken in favor of a "T-shaped" structure.

6.4 Conclusions

The intermolecular structure of the phenol dimer in the electronic ground state can be described as hydrogen bonded, with one phenol moiety acting as proton donor and the other as proton acceptor. The rings are more tilted than expected for a pure trans-linear arrangement as found e.g. for the phenol-water cluster. This deviation is a consequence of the additional dispersive interactions between the two aromatic rings, as has already been pointed out by Hobza *et al.*[213] Nevertheless, there are important differences between the structure determined on the basis of five different isotopomers and the results of the MP2/6-31G(d) counterpoise-corrected calculations by Hobza *et al.*[213] In order to properly compare the two structures the intermolecular distances and angles that have been defined by Hobza *et al.*,[213] were obtained for the

experimentally determined geometry. The results are presented in Table 6.4.

Table 6.4: Comparison of experimentally determined r_s geometry parameters of the phenol dimer in the S_0 state with the values of the MP2/6-31G(d) calculation by Hobza *et al.*[213] All distances are given in pm, angles and dihedral angles in °.

	r_s	MP2/6-31G(d,p)[213]
r(O_7O_8)	321	295
a($C_1O_7O_8$)	112.7	90.0
a($O_7O_8C_9$)	117.1	134.2
a($O_7O_8H_{8a}$)	116.0	132.1
d($C_2C_1O_7O_8$)	5.7	−2.4
d($C_1O_7O_8C_9$)	63.0	−56.1
d($O_7O_8C_9C_{10}$)	12.2	−19.8

First of all, the O_7O_8 distance obtained from the present structure is larger than that from the *ab initio* calculations. All other angles and dihedral angles are quite similar, but point to a slightly more bent structure than predicted by the *ab initio* calculations. The apparently large difference in the dihedral angle d($C_1O_7O_8C_9$) only describes two different orientations of the acceptor ring relative to the donor ring. In one of the structures the acceptor is below, in the other above the donor plane. These orientations are equivalent with respect to the intermolecular interactions. Thus, to conclude the results for the electronic ground state, a weaker hydrogen bonding interaction is found than predicted by the *ab initio* calculations, but a stronger dispersive interaction between the aromatic rings. The applicability of the model employed in this study (same geometry for both acceptor and donor) can be checked using the COM distances calculated from equation 6.6. If this assumption is correct the COM distances calculated from equation 6.6 and from the best structure fit using *pKrFit* should coincide within their uncertainties. For all isotopomers, close coincidence is found between the COM distances calculated in these two manners.

Since the assumption of local excitation in just one monomer moiety seems to be incorrect, the results of the determination of the electronically excited state structure are more doubtful. Several different models were tried to describe the excitation in the dimer, but none of these models converged to a physically meaningful structure. The most logical assumption for the excited state structures of the monomer moieties seems to be a local excitation in the donor moiety, with the geometry of the donor equal to the excited state structure of the phenol monomer and the acceptor moiety equal to the ground state structure. All models based on this assumption led to dimer structures in which the hydrogen bond is broken and which could better be described as "T-shaped". Nevertheless, from low resolution LIF and hole burning experiments on the dimer it is known that the intermolecular stretching vibration has very similar frequencies in the S_0 and S_1 states.[210] A break of the hydrogen bond upon electronic excitation therefore seems to be unrealistic.

Based on the monomer geometries of a CIS/6-311G(d,p) calculation the intermolecular geometry parameters were fitted to the rotational constants of the excited state (model 1). While the intermolecular geometry of the cluster is by no means expected to be correct when using a method which completely neglects the dispersion

interaction of the aromatic rings, the monomer geometries in such a cluster generally are well described. A shorter hydrogen bond length (229.3 pm) than in the electronic ground state (235.4 pm) was found. The tilt of the aromatic rings toward each other is smaller, i.e. the dispersive interaction seems to be smaller in the excited state. This opening of the dimer upon electronic excitation is further supported by the comparison of COM distances of the monomer moieties in the S_0 and S_1 state. While the hydrogen bond distance decreases upon excitation, the COM distance increases for all isotopomers. This is only possible if the tilt angle of both rings increases, cf. Figure 6.6. A fit assuming local excitation in one of the phenol moieties (model 2) lead to a very short hydrogen bond (174.7 pm), which does not seem to be realistic. The same procedure as for the electronic ground state has been used to check the reliability of the applied models. For the excited state the COM distances calculated from the moments of inertia and those from the fitted structures differ more than for the ground state, showing that the fit still contains model errors. Both model 1 and model 2 show nearly the same deviations, making it impossible to favor one of them.

The results for the excited state structure depend strongly on the chosen model and need further refinement using the information from other isotopomers than the ones used in this study in order to also estimate the changes in the monomer moieties upon electronic excitation. Nevertheless, as a common characteristic of all S_1 state structures, a decrease in hydrogen bond length and a decrease in the tilt angle of the aromatic ring is found. Until now no reliable theoretical method is available which is able to correctly describe the sensitive equilibrium between hydrogen bonding and dispersion interaction in the electronically excited state.

A genetic algorithm based determination of the ground and excited (^1L_b) state structure and the orientation of the transition dipole moment of benzimidazole.

The structure of benzimidazole has been determined in the electronic ground and excited states using rotationally resolved electronic spectroscopy. The rovibronic spectra of four isotopomers and subsequently the structure of benzimidazole have been automatically assigned and fitted using a genetic algorithm based fitting strategy. The lifetimes of the deuterated isotopomers have been shown to depend on the position of deuteration. The angle of the transition dipole moment with the main inertial axis could be determined to be $-30°$. Structures and transition dipole moment orientation have been calculated at various levels of theory and were compared to the experimental results.

7.1   Introduction

The thorough knowledge of excited state properties like structures, excitation energies, lifetimes, and transition dipole moments of indole and indole analogues is an important prerequisite for the interpretation of chromophore fluorescence in proteins. Many of the excited state properties of these molecules have been predicted at all levels of theory ranging from configuration interaction with single excitation over time-dependent density functional theory to complete active space self consistent field methods with second order perturbation corrections. The high level of approximation in some of the theoretical methods sometimes leads to contradictory results between the applied methods. Therefore, it is desirable to compare them to experimental results. Rotationally resolved fluorescence spectroscopy in combination with a genetic algorithm (GA) based fitting procedure is an ideal tool for the determination of all excited state properties mentioned above.

The automated assignment of very complex rotationally resolved electronic spectra using GA based fitting procedures has been shown to be very successful if the cost function can be evaluated sufficiently fast.[17,18,170] The obtained molecular parameters can be used in the interpretation and evaluation of excited state molecular properties like the orientation of the transition dipole moment, the excited state lifetime and the geometry in both electronic states connected by the transition. The problem of determining molecular structures from an insufficient number of inertial parameters is well known. If not enough information from singly substituted isotopomers is available to perform a complete Kraitchman analysis, a fit to a pseudo-Kraitchman structure can be used within a model geometry with reduced numbers of parameters to be fit.[225] Because of the nonlinear relation between internal coordinates and rotational constants it is necessary to perform a nonlinear fit, which means that starting values for the geometry parameters are needed and an iterative procedure has to be applied. If the number of inertial parameters is insufficient, several assumptions on the geometry have to be made regarding relations between the parameters. The more of these artificial constraints have to be imposed on the real geometry, the less reliable the fit gets regarding its ability to find the global minimum. Therefore the application of GA based strategies, which do not depend on the initial conditions, is also advantageous for the nonlinear fit of the geometry.

Benzimidazole easily forms several deuterated isotopomers upon coexpansion with D_2O which are spectrally well separated. Recording of isotopically substituted species always allows the determination of the orientation of the transition dipole moment (TDM), while the rotationally resolved electronic spectrum of a single isotopic species generally yields only the absolute value of the TDM angle.[170] The direction of the TDM contains information about the electronic nature of the excited state, which can be compared to theoretical predictions. The use of the GA for automated fitting of the rotationally resolved spectra allows for a very accurate determination of the TDM angle, because all lines in the spectrum are considered in the calculation of the cost function.

The low resolution R2PI spectra of the four isotopomers investigated in the present study have been presented by Jacoby *et al.*[226] Furthermore, they performed *ab initio* calculations on the different tautomers of benzimidazole. The first vibronically resolved spectrum of benzimidazole in a molecular beam was published by Jalviste and Treshchalov.[227] Velino *et al.* reported the microwave spectrum of benzimidazole and the ND deuterated isotopomer.[228] They proved planarity in the electronic ground state on the basis of the rotational constants of both isotopomers. The inertial parameters in the first electronically excited state were determined from a band contour analysis of benzimidazole in the vapour phase by Cané *et al.*[229] Later Berden *et al.* performed rotationally resolved LIF spectroscopy and proved the planarity of the molecule also in the first electronically excited state.[230] Serrano-Andrés and Borin presented a theoretical study of the absorption and emission spectra of benzimidazole.[231,232] They determined the transition dipole moment orientation from a CASSCF calculation to be $+29°$ for the ^1L_b-state of benzimidazole. This value is in contradiction with an experimentally determined one from polarization measurements in a stretched polymer of $-16°$.[233] A similar disagreement between the experimentally determined TDM and the CASSCF calculated value has been found for 7-azaindole.[170]

In the present study the structural parameters of benzimidazole in its ground

and electronically excited states are determined via a genetic algorithm based fitting procedure of both the experimental spectrum and the geometry. Furthermore the absolute orientation of the TDM of the lowest excited state of benzimidazole will be determined and compared to the results of *ab initio* calculations.

## 7.2 Methods

7.2.1 Experimental Procedures

The experimental setup for the rotationally resolved LIF is described elsewhere.[58] Briefly, it consists of a ring dye laser (Coherent 899-21) operated with Rhodamine 110, pumped with 6 W of the 514 nm line of an Ar^+-ion laser. The light is coupled into an external folded ring cavity (Spectra Physics) for second harmonic generation (SHG). The molecular beam is formed by expanding benzimidazole, seeded in 600 mbar of argon, through a 70 μm hole into the vacuum. The molecular beam machine consists of three differentially pumped vacuum chambers that are linearly connected by skimmers (1 mm and 3 mm diameter, respectively) in order to reduce the Doppler width. The molecular beam is crossed at right angles with the laser beam in the third chamber, 360 mm downstream of the nozzle. The resulting fluorescence is collected perpendicular to the plane defined by the laser and the molecular beam by an imaging optics setup consisting of a concave mirror and two plano-convex lenses. The resulting Doppler width in this setup is 25 MHz (FWHM). The integrated molecular fluorescence is detected by a photo-multiplier tube whose output is discriminated and digitized by a photon counter and transmitted to a PC for data recording and processing. The relative frequency is determined with a quasi confocal Fabry-Perot interferometer with a free spectral range (FSR) of 149.9434(56) MHz. The FSR has been calibrated using the combination differences of 111 transitions of indole for which the microwave transitions are known.[234,235] The absolute frequency was determined by recording the iodine absorption spectrum and comparing the transitions to tabulated lines.[5]

7.2.2 Theoretical methods

Ab initio calculations

The structure of benzimidazole in the electronic ground state was optimized at the HF/6-31G(d,p), B3LYP/6-31G(d,p) and MP2/6-31G(d,p) levels, and at the CIS/6-31G(d,p) level for the electronically excited S_1-state with the Gaussian 98 program package (Revision a11).[236] The SCF convergence criterion used throughout the calculations was an energy change below 10^{-8} Hartree, while the convergence criteria for the gradient optimization of the molecular geometry were $\partial E/\partial r < 1.5 \cdot 10^{-5}$ Hartree/Bohr and $\partial E/\partial \varphi < 1.5 \cdot 10^{-5}$ Hartree/degrees. Additionally, a CASSCF optimization of the ground and excited state structures was performed with an active space of ten electrons in nine orbitals. The CAS orbitals are shown in Figure 7.1, with both occupied and unoccupied ones sorted by increasing energy. The CASSCF calculations were performed using the MOLCAS-5.4 program package.[237] Additionally, the geometry of the electronically excited state was optimized using time-dependent density functional theory[238,239] with the B3-LYP functional[65,240] using the TZVP ba-

sis and Dunnings basis set of triple ζ quality (cc-pVTZ).[241] These calculations were performed with the program system TURBOMOLE[59,242] and also yield the TDM directions of the electronically excited states.
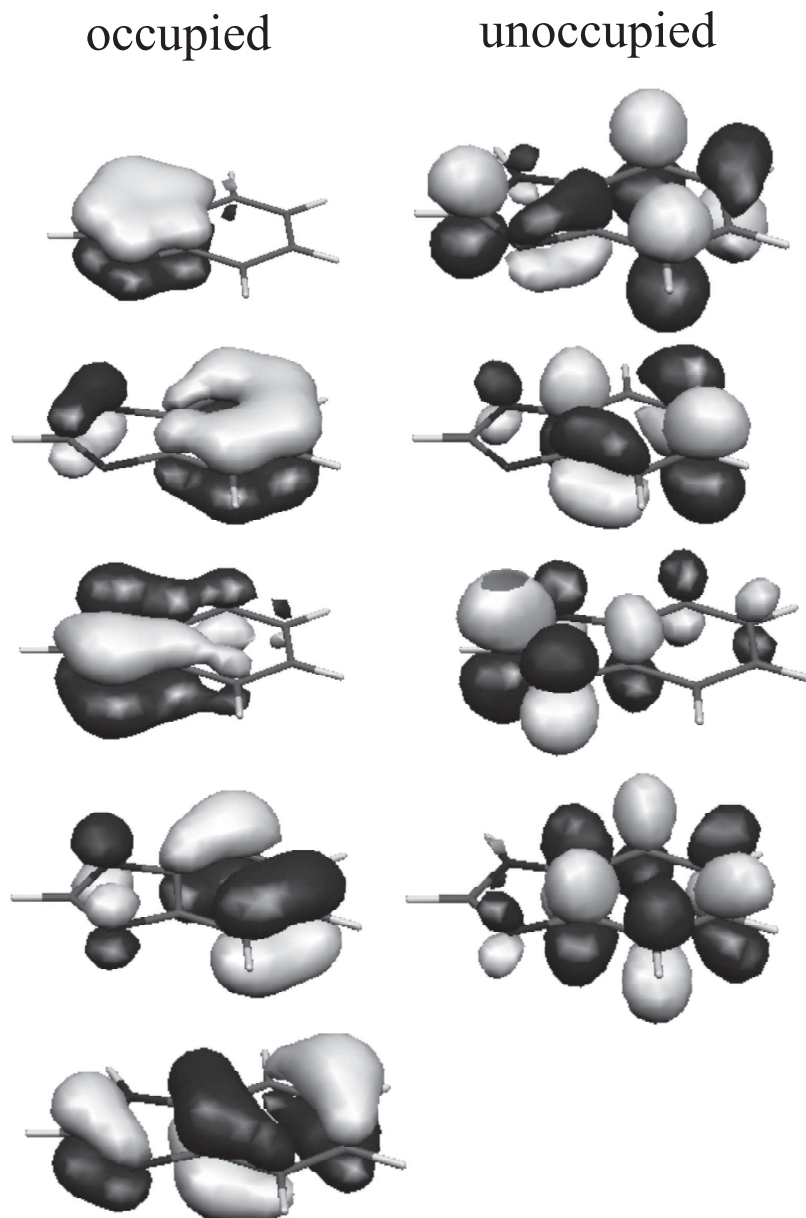
Figure 7.1: Occupied and unoccupied CASSCF orbitals sorted by increasing energy.

Genetic algorithms

The genetic algorithm is basically a global optimizer which uses concepts copied from reproduction and selection in nature. For a detailed description of the GA the reader is referred to the original literature.[113–115] The GA library PGAPack version 1.0, which can run on parallel processors, was used.[218] The elements of the GA which will be used in the analysis of spectra and structures will shortly be introduced.

- Representation of the parameters: The molecular parameters are encoded binary, each parameter representing a gene. A vector of all genes, which contains all molecular parameters, is called a chromosome. In an initial step the values for all parameters are set to random values between lower and upper limits which have to be chosen by the user.

- The solutions are evaluated by a fitness function, which is a measure for the agreement between simulation and experiment.

- One optimization cycle, including evaluation of the cost of all chromosomes, is called a generation.

- Pairs of chromosomes are selected for reproduction and their information is combined via a crossover process. Crossover combines information from the parent generations.

- The value of a small number of bits is changed randomly. This process is called mutation.

Fitting of the spectra

The cost function for evaluation of the quality of a given solution has been discussed in detail in previous work.[17,18] It is expressed as:

$$C_{fg} = 100(1 - F_{fg}) = 100(1 - \frac{(\boldsymbol{f}, \boldsymbol{g})}{\|\boldsymbol{f}\|\|\boldsymbol{g}\|}), \tag{7.1}$$

where $\boldsymbol{f}$ and $\boldsymbol{g}$ represent the experimental and calculated spectra, respectively. The inner product $(\boldsymbol{f}, \boldsymbol{g})$ is defined with the metric: $\boldsymbol{W}$

$$(\boldsymbol{f}, \boldsymbol{g}) = \boldsymbol{f}^T \boldsymbol{W} \boldsymbol{g}, \tag{7.2}$$

and the norm of $\boldsymbol{f}$ is defined as $\|\boldsymbol{f}\| = \sqrt{(\boldsymbol{f}, \boldsymbol{f})}$ (a similar definition holds for $\boldsymbol{g}$). $\boldsymbol{W}$ has the matrix elements $W_{ij} = w(|j - i|) = w(r)$. For $w(r)$ a triangle function[17] was used with a user controlled width of the base Δw:

$$w(r) = \begin{cases} 1 - |r| / \left(\frac{1}{2}\Delta w\right) & \text{for } |r| \leqslant \frac{1}{2}\Delta w \\ 0 & \text{otherwise.} \end{cases} \tag{7.3}$$

Since the GA performs a lineshape fit of the complete spectrum, much more information on the linewidth is gathered than from a lineshape fit to a few individual lines. In order to obtain the relevant parameters that determine the intensities in the spectrum a second GA fit was performed with a reduced search range for the inertial parameters and a weight function width $\Delta w = 0$. This resulted in improved values for the angle θ that is connected to the components of the transition dipole moment by:

$$\lambda_a{}^2 = (\mu_a/\mu)^2 = \cos^2\theta \tag{7.4}$$
$$\lambda_b{}^2 = (\mu_b/\mu)^2 = \sin^2\theta. \tag{7.5}$$

The determination of the Lorentzian component of the line width can be improved using a fit of all available intensities. The Gaussian width is fixed to the experimentally determined value of 25 MHz. The temperature dependence of the intensity is described by a two temperature model:[119]

$$n(T_1, T_2, w) = e^{-E/kT_1} + we^{-E/kT_2}, \tag{7.6}$$

where E is the energy of the lower state, k is the Boltzmann constant, w is a weighting factor and T_1 and T_2 are the two temperatures.

Fitting of the structure

The program *pKrFit*[24] was used to determine the structure of benzimidazole in the S_0 and S_1-states. There are several new features of the program which are described in the following.

One of the most limiting problems in the process of structure determination of larger molecules is the lack of independent data (rotational constants) compared to the number of model parameters. These parameters are the internal coordinates used to describe the geometry and a small number of parameters used to describe the vibrational contributions to the structure. Sometimes the number of model parameters to be determined can be reduced by using more symmetric models, where several parameters are interdependent by means of constraints (planarity, mirror planes, etc.), but often those symmetric models don't exist or prove to be bad approximations of the real structure. Another well-known method to increase the number of independent data is to combine data from different sources. This method has been shown to work successfully in combined fits of the intensities of vibronic spectra (Franck-Condon fit) and the changes of rotational constants upon electronic excitation (inertial parameter fit) in order to determine geometry changes upon excitation.[112] Another advantage of this method is that it minimizes the correlations among data of given measurement series. This was demonstrated by Lees, who investigated the positive effect of mixing data from different sources (infrared and microwave data), even though these had very different accuracies.[243]

To increase the number of data points in the structural determination fits the functional capability of *pKrFit* was extended to take both the moments of inertia and the angles (or the corresponding direction cosines) of the TDM of the respective isotopomer with the main inertial axes into account. Both experimental data sets are independent from each other and can be extracted from the spectral fits described in section 7.2.2. In the following it will be shown how these two data sets can be used in a combined fit to determine the best set of internal coordinates (i.e. distances, angles, and dihedral angles) describing a given molecular structure.

Using the nomenclature introduced by Ratzer *et al.*[24] the cost function to minimize in a pure rotational constants fit is given by the weighted sum of squared residuals:[244,245]

$$\chi^2 = \chi^2_{rot} = \Delta \boldsymbol{y}^T \boldsymbol{W}_{rot} \Delta \boldsymbol{y}. \tag{7.7}$$

In this equation $\boldsymbol{y}^T = (B^0_{a,1}, B^0_{b,1}, B^0_{c,1}, ..., B^0_{a,k}, B^0_{b,k}, B^0_{c,k})$ is the vector of $n = 3k$ measured and calculated rotational constants $\boldsymbol{y}_{exp}$ and $\boldsymbol{y}_{calc}$ of k isotopomers, respectively, $\Delta \boldsymbol{y} = \boldsymbol{y}_{exp} - \boldsymbol{y}_{calc}$ is their corresponding residual vector and $\boldsymbol{W}_{rot}$ denotes an

n-by-n positive-definite weight matrix obtained from the covariance matrix of the n experimental rotational constants. Via the inverse relation to the moments of inertia the rotational constants directly depend on the cartesian coordinates of the isotopomers, so that the mathematical relation between those n inertial values and the internal coordinates b_j, $j = 1..m$ of a hypothetical equilibrium structure is straightforward.

There exists no direct relation between the geometric TDM parameters, i.e. either polar angles (θ, ϕ) or squared direction cosines $(\lambda_a^2, \lambda_b^2)$, and the internal coordinates b_j of the molecule similar to that for the inertial parameters. However, an indirect relation can be deduced by recognizing that the rotation of the inertial frame of a given reference isotopomer into any other isotopomer also implies a corresponding change of the TDM vector. In other words: the former model of a molecule described by a set of internal coordinates is extended by a molecular geometry and an additional TDM vector of unit length of an arbitrary reference isotopomer. It should be emphasized that, although this ansatz adds two further fit parameters to the model, these are usually outweighed by the number of additionally available experimental TDM data. Mathematically, the TDM vector $\boldsymbol{\mu}_{ref} = (\mu_{ref,a}, \mu_{ref,b}, \mu_{ref,c})^T$ of the reference isotopomer is transformed into the TDM vector $\boldsymbol{\mu}_{other}$ of another isotopomer via:

$$\boldsymbol{\mu}_{other} = \boldsymbol{R}_{other}^T \boldsymbol{R}_{ref} \boldsymbol{\mu}_{ref}. \tag{7.8}$$

In this equation $\boldsymbol{R}_i$ denotes the 3×3 orthogonal rotation matrix which transforms the initial geometry of the ith isotopomer into its own inertial system. The fit program accepts either reduced polar angles or squared direction cosines as input parameters. The polar angles are reduced because the corresponding octant cannot be determined by the experiment and thus both angles are confined to the limited range 0–90° instead of their full range. The direction cosines are similarly constrained, because only their absolute value can be determined. Using the extended model the cost function is given by:

$$\chi^2 = \chi_{rot}^2 + \chi_{TDM}^2 = \Delta \boldsymbol{y}^T \boldsymbol{W}_{rot} \Delta \boldsymbol{y} + \Delta \boldsymbol{z}^T \boldsymbol{W}_{TDM} \Delta \boldsymbol{z}, \tag{7.9}$$

where either $\boldsymbol{z}^T = (\theta_1, \phi_1, ..., \theta_r, \phi_r)$ or $\boldsymbol{z}^T = (\lambda_{a,1}^2, \lambda_{b,1}^2, ..., \lambda_{a,r}^2, \lambda_{b,r}^2)$ in the general abc case depending on the available r transition dipole moment data. In the special case of ab hybrid spectra the vector $\boldsymbol{z}$ simplifies to $\boldsymbol{z}^T = (\theta_1, ..., \theta_r)$ or $\boldsymbol{z}^T = (\lambda_{a,1}^2, ..., \lambda_{a,r}^2)$. Similar to the weight matrix $\boldsymbol{W}_{rot}$ of the rotational constants, $\boldsymbol{W}_{TDM}$ is the weight matrix obtained from the covariance matrix of the TDM data. The standard deviations of the TDM data were determined from the standard deviations of three independent runs of the GA using different (random) starting parameters. Additionally it was assumed that no correlations exist among the different polar angles or direction cosines.

The original optimization strategy of *pKrFit* used a gradient-based χ^2 minimizer. While the speed of this approach is appealing, the main disadvantage is the possibility of becoming trapped in local minima different from the absolute one. The program's capabilities were extended by incorporating the same PGAPack global optimizer as used in the spectral fit. The GA library was used in minimization mode and thus directly used the correspondingly defined χ^2 value as cost function.

Furthermore the global minimizer has been extended to allow intermediate local minimization steps rather than simple cost function evaluations. This technique was originally introduced by Li and Scheraga as part of a simulated annealing (SA) exploration of the potential hypersurface of proteins.[246] Also termed *basin-hopping*[247] by Doyle and Wales, it was successfully combined with GA and SA to determine minimum-energy structures of fullerene and atomic clusters.[248–251]

7.3   Results and Discussion

The atomic numbering for the designation of the isotopomers and the geometry parameters for the structure fit used throughout this publication is shown in Figure 7.2.
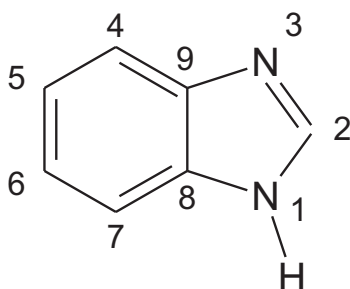
Figure 7.2: Atomic numbering used for definition of the isotopomers.

Figure 7.3 shows the rotationally resolved spectrum of the electronic origin ν_0 of 1H2H-benzimidazole at 36021.38 cm^{-1} along with a simulation using the best parameters given in Table 7.1, which were obtained by a GA fit as described in section 7.2.2. It is an *ab* hybrid type spectrum with an angle θ between the inertial *a*-axis and the transition dipole moment of 31.9(5)° (72.1 % *a*-type, 27.9 % *b*-type). The excited state lifetime of this isotopomer is determined to be 5.2(2) ns from a 30.8(10) MHz Lorentzian contribution to the Voigt profile.

Figure 7.4 shows the rovibronic spectrum of the electronic origin of 1D2D-benzimidazole; the electronic origins of the mixed isotopomers 1D2H-benzimidazole and 1H2D-benzimidazole were also measured but are not shown. The results of the GA fits of all four spectra are summarized in Table 7.1. All bands are *ab* hybrids with angles θ between the TDM and the inertial *a*-axis similar to that in the undeuterated isotopomer. Nevertheless, the small differences in the TDM angles of the different isotopomers are crucial in the determination of the absolute transition dipole moment orientation, as was shown by Schmitt *et al.*[170]

7.3.1   Orientation of the transition dipole moment and excited state lifetimes

Off-axis isotopic substitution results in a rotation of the respective inertial axis, but the orientation of the TDM remains the same. This procedure has successfully been applied to the determination of the absolute direction of the transition dipole moment in 7-azaindole.[170]
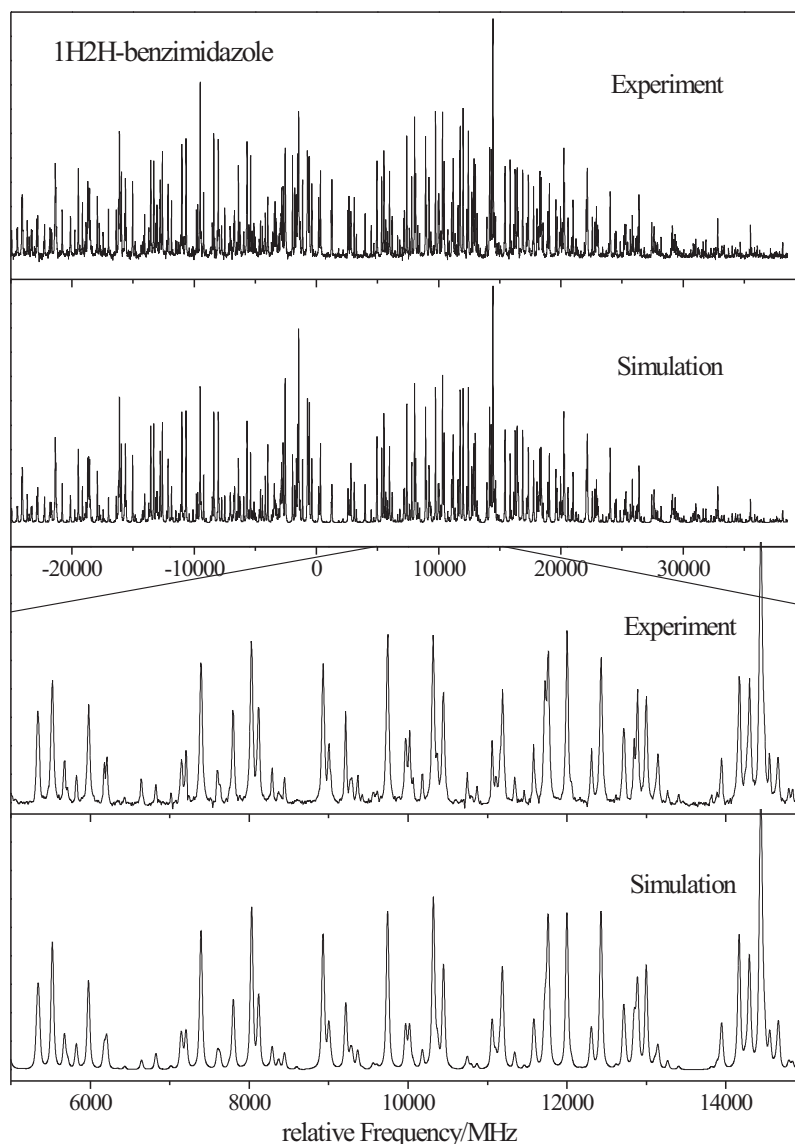
Figure 7.3: Rotationally resolved spectrum of the electronic origin ν_0 of 1H2H-benzimidazole at 36021.38 cm^{-1} along with a simulation using the best parameters given in Table 7.1.

If the sign of the angle of the TDM with the inertial a-axis is positive (orientation I in Figure 7.5), the angle should increase for 1D2H-Benzimidazole, if the sign is negative (orientation II in Figure 7.5), the angle will decrease. As both 1D2H-benzimidazole and 1D2D-benzimidazole have a smaller angle θ than the respective 1H2H-benzimidazole and 1H2D-benzimidazole the sign of the angle θ is negative. Table 7.2 compares the angles of the TDM vectors for the two lowest electroniccally excited states, ^1L_b and ^1L_a, from two different experiments with the results of electronic structure calculations at different levels of theory. The CIS/6-31(d,p) calculations give an angle θ of $-15°$, in fair agreement with the experimental result of $-32°$. The determination of the TDM angle from the CASSCF(10,9) calculations yields a value of $+36°$ for the lowest state, in contrast with experimental findings. A similar result was found for 7-azaindole, where the experimentally determined orientation of the

Table 7.1: Molecular parameters of the electronic origin band of benzimidazole (B) isotopomers as obtained from the genetic algorithm fit. The numbering of the substitution position refers to Figure 7.2.

	1H2H-B[a]	1D2H-B[a]	1H2D-B	1D2D-B
A''/MHz	3929.720(7)	3811.29(19)	3930.61(69)	3810.69(57)
B''/MHz	1679.259(3)	1658.846(2)	1618.58(29)	1599.70(25)
C''/MHz	1176.747(1)	1156.052(3)	1146.71(28)	1126.94(24)
$\Delta\nu_0$/cm^{-1}[b]	0.00	7.08(1)	24.18(1)	31.26(1)
θ/°	$-31.9(5)$	$-30.4(5)$	$-31.3(5)$	$-30.2(5)$
$\Delta_{Lorentz}$/MHz	30.8(10)	22.8(10)	30.8(10)	26.5(10)
$t_{1/2}$/ns	5.2(2)	7.0(3)	5.2(2)	6.0(3)
ΔA/MHz	$-155.72(22)$	$-149.98(11)$	$-156.27(14)$	$-150.26(13)$
ΔB/MHz	$-15.28(15)$	$-13.77(13)$	$-14.67(14)$	$-13.53(14)$
ΔC/MHz	$-21.40(11)$	$-20.47(11)$	$-20.65(13)$	$-19.85(13)$

[a] Ground state rotational constants fixed to the microwave values from Velino *et al.*[228]

[b] Relative to the electronic origin of 1H2H-benzimidazole at 36021.38(1) cm^{-1}

TDM has a sign opposite to that obtained from CASSCF calculations. Further calculations on the transition dipole moment were performed with time-dependent B3-LYP calculations using the TZVP basis set. Calculating the TDM in the TDB3-LYP optimized S_1 state geometry a positive angle of $+36°$, close to the results of the CASSCF calculations, resulted. If the geometry is kept fixed at the B3-LYP geometry obtained for the S_0 state the TDM angle changes to $+14°$. While for time-dependent density functional theory a large difference between the TDM calculated in the ground state geometry and the one calculated in the excited state geometry is found, both CAS and CIS calculations show nearly no differences with respect to the reference geometry (S_0 or S_1). The large difference found at TDDFT level between the TDM calculated in the S_0 and S_1 state geometries, respectively, can of course not be attributed to a mere rotation of the inertial axis system upon electronic excitation. The geometry changes are too small, which is immediately obvious from the Franck-Condon pattern of the vibronic spectrum which shows the vibrationless origin as the far most intense band.

Table 7.2: Experimental and calculated TDM orientations of the two lowest excited states of benzimidazole. CASSCF calculations have been performed with the (10,9) space described in the text using the 6-31G(d,p) basis set. The TDDFT calculations have been performed using the B3-LYP functional and the TZVP basis set.

	Exp.[a]	Exp.[b]	CIS[c]	CIS[d]	CAS[c]	CAS[d]	TDDFT[c]	TDDFT[d]
S_1 (^1L_b)	-32	-16	-15	-14	$+36$	$+36$	$+39$	$+14$
S_2 (^1L_a)	$-$	-80	-71	-79	-52	-53	$-$[e]	-34

[a] This work

[b] From polarized absorption in a stretched polymer[233]

[c] In the optimized geometry of the excited state

[d] In the optimized geometry of the ground state

[e] Due to state flipping the optimization did not converge for the S_2 state
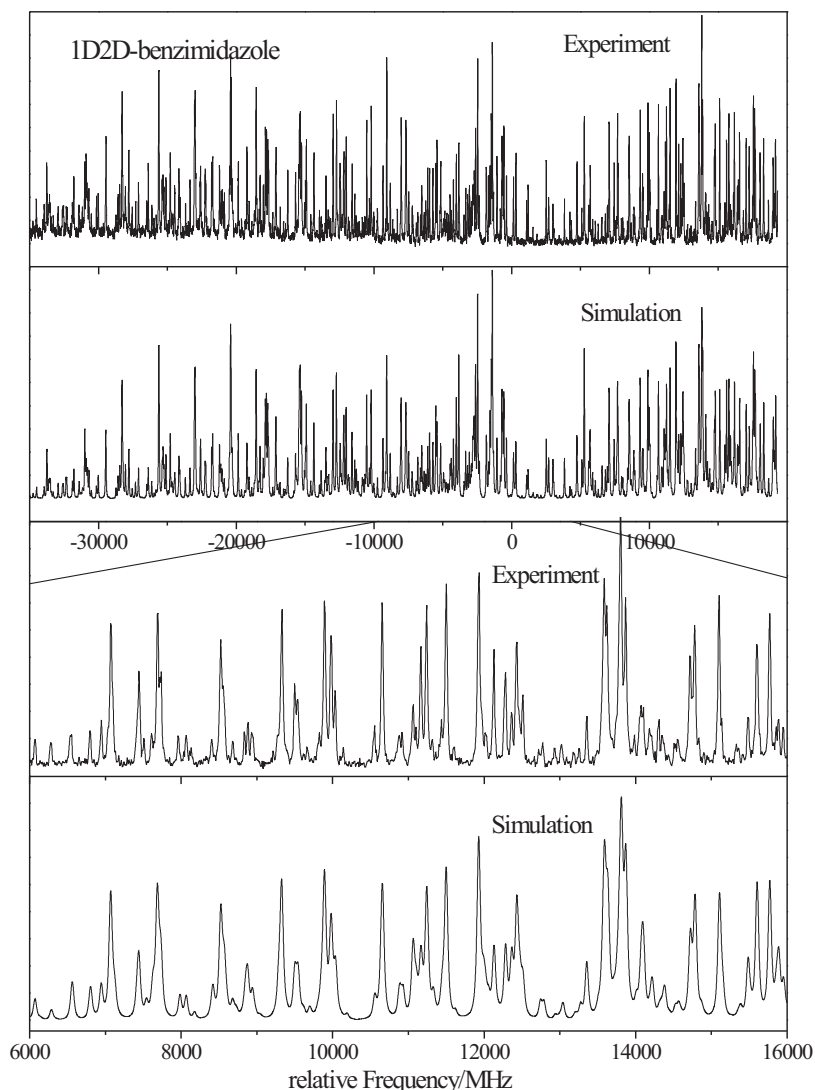
Figure 7.4: Rotationally resolved electronic spectrum of the origin ν_0 of 1D2D-benzimidazole at 36052.64 cm^{-1} along with a simulation using the best parameters given in Table 7.1.

The lifetime of the four isotopomers was determined from the Lorentzian contribution to the Voigt profile. The lineshape fit using the GA results in very accurate values for the Lorentzian contribution, since in contrast to a conventional lineshape fit all transitions which contribute to the band are taken into account, even if they partially overlap. Although the differences between the lifetimes determined from the Lorentz width are small, they are well outside the uncertainties. The two isotopomers that are deuterated at the N-H group (1D2H-benzimidazole and 1D2D-benzimidazole) have longer lifetimes (6.0 and 7.0 ns) than the ones undeuterated in this position (5.2 ns). A similar situation was found for phenol, where deuteration at the hydroxy group leads to a substantial increase of the lifetime.[24,126,181]. As Sobolewski and Domcke pointed out for the similar indole system, an increasing lifetime upon deuteration at the NH group indicates a control of the lifetime by a tunneling process along the NH coordinate.[127] This tunneling takes place between the the excited $\pi - \pi^*$ and $\pi - \sigma^*$ surfaces. The $\pi - \sigma^*$ surface has a conical intersection with the ground state surface
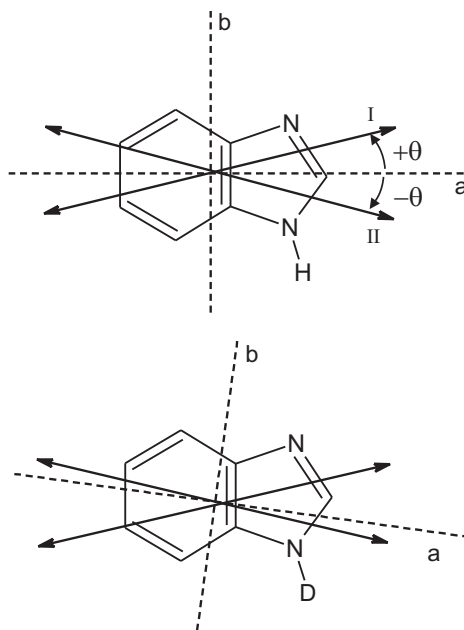
Figure 7.5: Angle θ between TDM and inertial a-axis for 1H2H-benzimidazole and 1D2H-benzimidazole. The rotation of the inertial axis system upon deuteration is not drawn to scale for reasons of clarity.

which allows a very fast evolution of the excited state population to the ground state.

7.3.2 Determination of the structure

Comparison to the *ab initio* calculations

The experimentally determined rotational constants of benzimidazole are compared to *ab initio* calculated rotational constants in Table 7.3. The MP2/6-31G(d,p) rotational constants agree within 1% with the experimental ones. Although the HF (for the ground state) and CIS calculations (for the excited state) with the same basis set show quite substantial deviations in the absolute values, the difference between both sets gives a very good approximation of the change in the rotational constants upon electronic excitation (cf. Table 7.3). The CASSCF(10/9) optimization produces acceptable absolute values, slightly worse than at the MP2 level for the ground state and also very accurate changes upon electronic excitation. Even better absolute rotational constants are obtained from density functional theory for the electronic ground state and time-dependent density functional theory for the electronically excited state. Both DFT and TDDFT have been performed using the B3-LYP functional with the TZVP basis set.

Fit of the structure

The r_0-structure of benzimidazole has been determined using the program *pKrFit*, whose new features are described in section 7.2.2. The bond lengths obtained from the fit to the rotational constants and to the changes of the TDM angle θ of four isotopomers are given in Table 7.4. The TDM direction in the undeuterated benzimidazole has been taken as a reference and the change in orientation for the three

Table 7.3: Experimental and *ab initio* inertial constants of benzimidazole. All calculations have been performed using the 6-31G(d,p) basis set. All values are given in MHz. The DFT and TDDFT calculations have been performed using the B3-LYP functional and the TZVP basis set.

	Exp.	MP2	HF	CIS	CIS-HF	CAS(10/9)	B3-LYP/TDB3-LYP
A''	3929.7	3918	4016	-	-	3971^a	3953
B''	1679.3	1681	1700	-	-	1684^a	1682
C''	1176.7	1176	1194	-	-	1183^a	1180
A'	3774.0	-	-	3876	-	3807^b	3773^b
B'	1664.0	-	-	1690	-	1657^b	1672^b
C'	1155.3	-	-	1177	-	1154^b	1160^b
ΔA	-155.7	-	-	-	-140	-164	-180
ΔB	-15.3	-	-	-	-10	-27	-10
ΔC	-21.4	-	-	-	-17	-29	-20

^{a} Geometry optimized to the S_0-state

^{b} Geometry optimized to the S_1-state

remaining isotopomers was used in the fit as an additional parameter.[a] In the Born-Oppenheimer approximation the different TDM orientations are only due to the geometry change induced rotations of the inertial axis system. The application of genetic algorithms for the variation of the geometry parameters minimized the risk of becoming trapped in a local minimum, which was found to happen easily if gradient-based downhill optimizers were used. Furthermore, the possibility of defining physically meaningful parameter limits excludes the output of molecular structures which bear no relationship to reality.

Table 7.4: Comparison of experimentally determined geometry parameters of benzimidazole in the S_0 and S_1 states. All distances are given in pm.

	S_0	S_1	Δ
d(N_1C_8)	137.0(7)	133.8(18)	-3.2
d(C_8C_9)	140.7(0)	137.3(10)	-3.4
d(C_9N_3)	137.6(6)	132.5(17)	-5.1
d(N_3C_2)	129.6(10)	129.8(12)	$+0.2$
d(C_2N_1)	144.4^a	143.3^a	-1.1
d(C_9C_4)	141.3(11)	144.5(20)	$+3.2$
d(C_4C_5)	142.3(3)	139.9(8)	-2.3
d(C_5C_6)	144.6(1)	148.0(5)	$+3.4$
d(C_6C_7)	140.7(11)	146.0(22)	$+5.3$
d(C_7C_8)	139.0^a	146.8^a	$+7.8$

^{a} This parameter is not needed in the Z-matrix definition of the structure, since it is the last bond in a cyclic system and is therefore defined by the preceding bond lengths. For this reason it is not included in the fit but calculated from the resulting structure and given here only for completeness.

---

[a]Note that the method is generally invariant under the choice of the actual reference orientation, regardless of the quality of the initial TDM parameter value

Comparison with the results of the B3-LYP/TDB3-LYP optimized geometries shows good agreement with the trends of the experimentally determined geometry changes. While a general expansion in the benzene ring is found upon excitation, the situation in the imidazole ring is different. Whereas a general decrease in bond lengths is deduced from the experiment, the difference between the B3-LYP bond lengths (for the ground state) and the time-dependent B3-LYP (for the excited state) in the imidazole ring shows alternating bond length changes.

Since the deuteration takes place only in the imidazole moiety of the molecule the geometry changes in the benzene moiety are quite inaccurate and correlated, and depend considerably on the chosen model. Therefore, the values of Table 7.4 present only a possible set of geometry changes. More isotopic substitutions are necessary for a more complete description of the geometry changes upon electronic excitation.

7.4 Conclusions

The geometry of benzimidazole has been determined experimentally in the S_0 state and the first electronically excited S_1 state. The structure in both states was fit to the rotational constants of four different isotopomers and the change of the TDM orientation between the isotopomers due to inertial axis rotation. As optimizer both a gradient-based Levenberg-Marquart variant and a genetic algorithm have been used. The first allows very fast optimizations (in less than a second on a fast desktop personal computer) while the latter has the advantage of being implicitly independent of the starting geometry. Convergence with the GA can be reached within 200 generations in about 2 minutes. The geometry changes upon electronic excitation can be divided into two major contributions: A general increase of the bond lengths in the benzene ring moiety and an overall decrease of bond lengths in the imidazole moiety. The main contributions to the $S_1(^1L_b) \leftarrow S_0$ transition in the one-electron approximation of the CIS calculations are HOMO $\rightarrow$ LUMO (0.6), HOMO-1 $\rightarrow$ LUMO+1 (0.3), and HOMO-1 $\rightarrow$ LUMO (0.1), cf Figure 7.1. The main (π) bonding contributions of HOMO and HOMO-1 are localized in the benzene ring, while the imidazole ring has non-bonding or anti-bonding characteristics. The LUMO and LUMO+1 are comprised of mainly anti-bonding interactions in the benzene ring and non-bonding and anti-bonding interactions in the imidazole ring. This fact might give a pictorial explanation for the origin of the observed geometry changes. Of course one has to keep in mind that other references than single excitations also contribute considerably to the excitation.

While the geometric structure of the electronically excited state can be calculated with sufficient accuracy even at the time-dependent density functional level of theory, the determination of the transition dipole moment orientation poses serious problems to theory. First of all, although the rotational constants of the excited state from the CIS, TDDFT, and CASSCF calculations closely match the experimental values, even the quadrant of the TDM vector differs between the various calculations. Only the CIS calculated TDM orientation points to the negative quadrant (cf. Figure 7.5) as was found experimentally. CASSCF calculations with the complete active π space result in a positive value. Obviously, for an exact calculation of the TDM orientation the excitations in the σ space give important contributions. Although the

CIS calculation includes only single excitations, the inclusion of σ excitations gives a better description of the TDM than a complete CI in a limited space (neglecting σ configurations) like in CASSCF. Nevertheless, regarding the level of theory the good agreement between experiment and CIS calculations has to be viewed as merely fortuitous. Time-dependent DFT also considers only single excitations. Although the geometry change upon electronic excitation is small, the transition dipole moment orientation depends strongly on the reference geometry (S_0 or S_1). For comparison with the vertical excitation scheme of the experiment the value calculated in the optimized ground state geometry has to be considered. This value is still positive, but much smaller than the respective CASSCF value. Future calculations, which include multiple excitations in a larger space (multi reference CI) together with time-dependent DFT should result in more accurate predictions for the transition dipole moment orientation.

Bibliography

1. F. Wöhler, Annalen der Physik und Chemie **12**, 253 (1828).
2. Worldwide Protein Data Bank, http://www.wwpdb.org/ (2008).
3. D. L. Nelson and M. M. Cox, *Lehninger - Principles of Biochemistry* (W. H. Freeman and Company, New York, 2005), 4th ed.
4. G. Myszkiewicz, Ph.D. thesis, University, Molecular and Biophysics group, Nijmegen (2005).
5. S. Gerstenkorn and P. Luc, *Atlas du spectre d'absorption de la molécule d'iode* (CNRS, Paris, 1982).
6. M. J. Duer, *Introduction to Solid-State NMR Spectroscopy* (Blackwell, 2004).
7. W. Demtröder, *Laser Spectroscopy* (Springer-Verlag, Berlin, 1981).
8. H. Abe, S. Kamei, N. Mikami, and M. Ito, Chem. Phys. Lett. **109**, 217 (1984).
9. B. C. Guo, K. P. Kerns, and J. A. W. Castleman, Science **255**, 1411 (1992).
10. E. Nir, K. Kleinermanns, and M. S. de Vries, Nature **408**, 949 (2000).
11. W. Gordy and R. L. Cook, *Microwave Molecular Spectra* (Wiley, New York, 1984), 3rd ed.
12. C. Rolland and P. B. Corkum, Opt. Commun. **59**, 64 (1986).
13. M. Drabbels, W. L. Meerts, and J. J. ter Meulen, J. Chem. Phys. **99**, 2352 (1993).
14. F. Duschinsky, Acta Physicochimica U.R.S.S. **7**, 551 (1937).
15. H. C. Longuet-Higgins, Mol. Phys. **6**, 445 (1963).
16. P. R. Bunker and P. Jensen, *Molecular Symmetry and Spectroscopy* (NRC Research Press, Ottawa, Ontario, Canada, 1998), 2nd ed.
17. J. A. Hageman, R. Wehrens, R. de Gelder, W. L. Meerts, and L. M. C. Buydens, J. Chem. Phys. **113**, 7955 (2000).
18. W. L. Meerts, M. Schmitt, and G. Groenenboom, Can. J. Chem. **82**, 804 (2004).
19. W. L. Meerts and M. Schmitt, Int. Rev. Phys. Chem. **25**, 353 (2006).
20. A. Ostenmeier, A. Gawelcyk, and N. Hansen, *Step-size Adaptation Based on Non-Local Use of Selection Information*, vol. 3 of *Parallel Problem Solving from Nature* (Springer, Berlin/Heidelberg, 1994).
21. O. M. Shir and T. Bäck, *The Second Harmonic Generation Case-Study as a Gateway for ES to Quantum Control Problems*, Proceedings of the Genetic and Evolutionary Computation Conference (ACM Press, London, UK, 2007).
22. N. Hansen and A. Ostenmeier, Evolutionary Computation **9**, 159 (2001).
23. N. Hansen and S. Kern, in *Parallel Problem Solving from Nature PPSN VIII*, edited by X. Yao (Springer, 2004), vol. 3242 of *LNCS*, pp. 282–291.

24. C. Ratzer, J. Küpper, D. Spangenberg, and M. Schmitt, Chem. Phys. **283**, 153 (2002).

25. J. Kraitchman, Am. J. Phys. **21**, 17 (1953).

26. F. Jensen, *Introduction to Computational Chemistry* (John Wiley & Sons, Chichester, 1999).

27. F. Madeja and M. Havenith, J. Chem. Phys. **117**, 7162 (2002).

28. F. Graf, T.-K. Ha, and R. R. Ernst, J. Chem. Phys. **75**, 2914 (1981).

29. S. Nagaoka, N. Hirota, T. Matsushita, and K. Nishimoto, Chem. Phys. Lett. **92**, 498 (1982).

30. Y. Maréchal, J. Chem. Phys. **87**, 6344 (1987).

31. Z. Smedarchina, A. Fernández-Ramos, and W. Siebrand, J. Chem. Phys. **122**, 134309 (2005).

32. Q. Xue, A. J. Horsewill, M. Johnson, and H. Trommsdorff, J. Chem. Phys. **120**, 11107 (2004).

33. F. Fillaux, M. H. Limage, and F. Romain, Chem. Phys. **276**, 181 (2002).

34. C. C. Costain and G. P. Srivastava, J. Chem. Phys. **41**, 1620 (1964).

35. H. Morita and S. Nagakura, Journal of Molecular Spectroscopy **42**, 536 (1972).

36. M. Ortlieb and M. Havenith, J. Phys. Chem.A **111**, 7355 (2007).

37. A. Gutberlet, G. W. Schwaab, and M. Havenith, Chem. Phys. **343**, 158 (2008).

38. A. Oppenländer, C. Rambaud, H. P. Trommsdorff, and J.-C. Vial, Phys. Rev. Lett. **63**, 1432 (1989).

39. C. Rambaud and H. P. Trommsdorff, Chem. Phys. Lett. **306**, 124 (1999).

40. K. Remmers, W. L. Meerts, and I. Ozier, J. Chem. Phys. **112**, 10890 (2000).

41. K. Sakota and H. Sekiya, J. Phys. Chem.A **109**, 2718 (2005).

42. K. Sakota and H. Sekiya, J. Phys. Chem.A **109**, 2722 (2005).

43. A. Held and D. W. Pratt, J. Chem. Phys. **96**, 4869 (1992).

44. A. Müller, F. Talbot, and S. Leutwyler, J. Chem. Phys. **116**, 2836 (2002).

45. C. A. Southern, D. H. Levy, J. A. Stearns, G. M. Florio, A. Longarte, and T. S. Zwier, J. Phys. Chem.A **108**, 4599 (2004).

46. G. Meijer, M. S. de Vries, H. E. Hunziker, and H. R. Wendt, J. Chem. Phys. **92**, 7625 (1990).

47. C. K. Nandi, M. K. Hazra, and T. Chakraborty, J. Chem. Phys. **121**, 5261 (2004).

48. D. E. Poeltl and J. K. McVey, J. Chem. Phys. **78**, 4349 (1983).

49. D. E. Poeltl and J. K. McVey, J. Chem. Phys. **80**, 1801 (1984).

50. C. A. Southern, D. H. Levy, G. M. Florio, A. Longarte, and T. S. Zwier, J. Phys. Chem.A **107**, 4032 (2003).

51. J. C. Baum and D. S. McClure, J. Am. Chem. Soc. **102**, 720 (1980).

52. Y. Tomioka, H. Abe, N. Mikami, and M. Ito, J. Phys. Chem. **88**, 2263 (1984).

53. C. K. Nandi and T. Chakraborty, J. Chem. Phys. **120**, 8521 (2004).

54. J. Antony, G. von Helden, G. Meijer, and B. Schmidt, J. Chem. Phys. **123**, 014305 (2005).

55. G. M. Florio, E. L. Sibert III, and T. S. Zwier, Faraday Discuss. **118**, 315 (2001).

56. G. M. Florio, T. S. Zwier, E. M. Myshakin, K. D. Jordan, and E. L. Sibert III, J. Chem. Phys. **118**, 1735 (2003).

57. J. M. Bakker, L. M. Aleese, G. von Helden, and G. Meijer, J. Chem. Phys. **119**, 11180 (2003).

58. M. Schmitt, J. Küpper, D. Spangenberg, and A. Westphal, Chem. Phys. **254**, 349 (2000).

59. R. Ahlrichs, M. Bär, M. Häser, H. Horn, and C. Kölmel, Chem. Phys. Lett. **162**, 165 (1989).

60. A. Schäfer, C. Huber, and R. Ahlrichs, J. Chem. Phys. **100**, 5829 (1994).

61. C. Hättig and A. Köhn, J. Chem. Phys. **113**, 6939 (2002).

62. C. Hättig, J. Chem. Phys. **117**, 7751 (2002).

63. S. Grimme and M. Waletzke, J. Chem. Phys. **111**, 5645 (1999).

64. A. D. Becke, J. Chem. Phys. **98**, 1372 (1993).

65. C. Lee, W. Yang, and R. Parr, Phys. Rev. B **37**, 785 (1988).

66. C. Peng and H. B. Schlegel, Israel J. Chem. **33**, 449 (1994).

67. M. J. Frisch, G. W. Trucks, H. B. Schlegel, G. E. Scuseria, M. A. Robb, J. R. Cheese-man, J. A. Montgomery, Jr., T. Vreven, K. N. Kudin,, *Gaussian 03, revision a.1*, Gaussian, Inc., Pittsburgh, PA (2003).

68. T. Helgaker, Chem. Phys. Lett. **182**, 503 (1991).

69. O. M. Shir, C. Siedschlag, T. Bäck, and M. J. Vrakking, Opt. Comm. **264**, 511 (2006).

70. G. Bruno and L. Randaccio, Acta Cryst. B **36**, 1711 (1980).

71. L. L. Connell, S. M. Ohline, P. W. Joireman, T. C. Corcoran, and P. M. Felker, J. Chem. Phys. **96**, 2585 (1992).

72. M. Onda, M. Asai, K. Takise, K. Kuwae, K. Hayami, A. Kuroe, M. Mori, H. Miyazaki, N. Suzuki, and I. Yamaguchi, J. Mol. Struct. **482**, 301 (1999).

73. J. Bicerano, H. F. Schaefer III, and W. H. Miller, J. Am. Chem. Soc. **105**, 2550 (1983).

74. E. A. Meyer, R. K. Castellano, and F. Diederich, Angew. Chem. Int. Ed. **42**, 1210 (2003).

75. D. J. Nesbitt, Annu. Rev. Phys. Chem. **45**, 367 (1994).

76. H. J. Neusser and K. Siglow, Chem. Rev. **100**, 3921 (2000).

77. H. Krause and H. J. Neusser, Chem. Rev. **94**, 1829 (1994).

78. E. J. Bieske and O. Dopfer, Chem. Rev. **100**, 3963 (2000).

79. M. Schmitt, C. Ratzer, and W. L. Meerts, J. Chem. Phys. **120**, 2752 (2004).

80. T. M. Korter, J. Küpper, and D. W. Pratt, J. Chem. Phys. **111**, 3946 (1999).

81. J. E. Braun, T. L. Grebner, and H. J. Neusser, J. Phys. Chem.A **102**, 3273 (1998).

82. N. Gonohe, H. Abe, N. Mikami, and M. Ito, J. Phys. Chem. **89**, 3642 (1985).

83. E. J. Bieske, M. W. Rainbird, I. M. Atkinson, and A. E. W. Knight, J. Chem. Phys. **91**, 752 (1989).

84. M. Mons, J. L. Calve, F. Piuzzi, and I. Dimicoli, J. Chem. Phys. **92**, 2155 (1990).

85. M. Schmidt, M. Mons, and J. L. Calve, Z. Phys. D **17**, 153 (1990).

86. G. V. Hartland, B. F. Henson, V. A. Venturo, and P. M. Felker, J. Phys. Chem. **96**, 1164 (1992).

87. A. Fujii, M. Miyazaki, T. Ebata, and N. Mikami, J. Chem. Phys. **110**, 11125 (1999).

88. T. Ebata, A. Iwasaki, and N. Mikami, J. Phys. Chem.A **104**, 7974 (2000).

89. J. Makarewicz, J. Chem. Phys. **111**, 084310 (1999).

90. F. Tran and T. A. Wesolowski, Int. J. Quantum Chem. **101**, 854 (2005).

91. J. Cerny, X. Tong, P. Hobza, and K. Müller-Dethlefs, J. Chem. Phys. **128**, 114319 (2008).

92. M. A. Vincent, I. H. Hillier, C. A. Morgado, N. A. Burton, and X. Shan, J. Chem. Phys. **128**, 044313 (2008).

93. M. S. Ford, S. R. Haines, I. Pugliesi, C. E. H. Dessent, and K. Müller-Dethlefs, J. Electron Spectrosc. Relat. Phenom **112**, 231 (2000).

94. X. Zhang and J. L. Knee, Faraday Discuss. **97**, 299 (1994).

95. C. E. H. Dessent, S. R. Haines, and K. Muller-Dethlefs, Chem. Phys. Lett. **315**, 103 (1999).

96. C. E. H. Dessent and K. Muller-Dethlefs, Chem. Rev. **100**, 3999 (2000).

97. S. R. Haines, C. E. H. Dessent, and K. Muller-Dethlefs, J. Electron Spectrosc. Relat. Phenom. **108**, 1 (2000).

98. A. Fujii, T. Sawamura, S. Tanabe, T. Ebata, and N. Mikami, Chem. Phys. Lett. **225**,

104 (1994).

99. N. Solca and O. Dopfer, Chem. Phys. Lett. **325**, 354 (2000).

100. N. Solca and O. Dopfer, J. Mol. Struct. **563–564**, 241 (2001).

101. N. Solca and O. Dopfer, J. Phys. Chem.A **105**, 5637 (2000).

102. N. Solca and O. Dopfer, Chem. Phys. Lett. **369**, 68 (2003).

103. O. Dopfer, Z. Phys. Chem. **219**, 125 (2005).

104. J. Cerny, X. Tong, P. Hobza, and K. Müller-Dethlefs, Phys. Chem. Chem. Phys. p. in press (2008).

105. S. Ishiuchi, M. Sakai, Y. Tsuchida, A. Takeda, Y. Kawashima, M. Fujii, O. Dopfer, and K. Müller-Dethlefs, Angew. Chem. Int. Ed. **44**, 6149 (2005).

106. S. Ishiuchi, M. Sakai, Y. Tsuchida, A. Takeda, Y. Kawashima, O. Dopfer, K. Müller-Dethlefs, and M. Fujii, J. Chem. Phys. **127**, 114307 (2007).

107. S. Ishiuchi, Y. Tsuchida, O. Dopfer, K. Müller-Dethlefs, and M. Fujii, J. Phys. Chem.A **111**, 7569 (2007).

108. S. Gerstenkorn and P. Luc, *Atlas du spectre d'absorption de la molécule d'iode 14800 - 20000 cm^{-1}* (CNRS, Paris, 1986).

109. S. R. Haines, W. D. Geppert, D. M. Chapman, M. J. Watkins, C. E. H. Dessent, M. C. R. Cockett, and K. Müller-Dethlefs, J. Chem. Phys. **109**, 9244 (1998).

110. H. Horn, H. Weiss, M. Häser, M. Ehrig, and R. Ahlrichs, J. Comput. Chem. **12**, 1058 (1991).

111. P. Deglmann, F. Furche, and R. Ahlrichs, Chem. Phys. Lett. **362**, 511 (2002).

112. D. Spangenberg, P. Imhof, and K. Kleinermanns, Phys. Chem. Chem. Phys. **5**, 2505 (2003).

113. J. H. Holland, *Adaption in Natural and Artificial Systems* (MI: The University of Michigan Press, Ann-Arbor, 1975).

114. D. E. Goldberg, *Genetic Algorithms in search, optimisation and machine learning* (Addison-Wesley, Reading Massachusetts, 1989).

115. I. Rechenberg, *Evolutionsstrategie - Optimierung technischer Systeme nach Prinzipien der biologischen Evolution* (Frommann-Holzboog, Stuttgart, 1973).

116. W. L. Meerts and M. Schmitt, Phys. Scripta **73**, C47 (2005).

117. I. Kalkman, C. Vu, M. Schmitt, and W. L. Meerts, ChemPhysChem **9**, 1788 (2008).

118. G. Lembach and B. Brutschy, J. Chem. Phys. **107**, 6156 (1997).

119. Y. R. Wu and D. H. Levy, J. Chem. Phys. **91**, 5278 (1989).

120. G. Berden, W. L. Meerts, M. Schmitt, and K. Kleinermanns, J. Chem. Phys. **104**, 972 (1996).

121. M. Schmitt, D. Krügler, M. Böhm, C. Ratzer, V. Bednarska, I. Kalkman, and W. L. Meerts, Phys. Chem. Chem. Phys. **8**, 228 (2006).

122. T. Weber and H. J. Neusser, J. Chem. Phys. **94**, 7689 (1991).

123. M. Bixon and J. Jortner, J. Chem. Phys. **48**, 715 (1968).

124. R. J. Lipert and S. D. Colson, J. Chem. Phys. **89**, 4579 (1988).

125. R. J. Lipert, G. Bermudez, and S. D. Colson, J. Phys. Chem. **92**, 3801 (1988).

126. R. J. Lipert and S. D. Colson, J. Phys. Chem. **93**, 135 (1989).

127. A. L. Sobolewski, W. Domcke, C.Dedonder-Lardeux, and C.Jouvet, Phys. Chem. Chem. Phys. **4**, 1093 (2002).

128. A. L. Sobolewski and W. Domcke, J. Phys. Chem.A **105**, 9275 (2001).

129. N. Mikami, A. Hiraya, I. Fujiwara, and M. Ito, Chem. Phys. Lett. **74**, 531 (1980).

130. W. E. Sinclair and D. W. Pratt, J. Chem. Phys. **105**, 7942 (1996).

131. N. W. Larsen, E. L. Hansen, and F. M. Nicolaisen, Chem. Phys. Lett. **43**, 584 (1976).

132. R. A. Kydd and P. J. Krueger, Chem. Phys. Lett. **49**, 539 (1977).

133. E. R. T. Kerstel, M. Becucci, G. Pietraperzia, and E. Castellucci, Chem. Phys. **199**,

263 (1995).

134. E. R. T. Kerstel, M. Becucci, G. Pietraperzia, D. Consalvo, and E. Castellucci, J. Mol. Spec. **177**, 74 (1996).

135. R. A. Kydd and P. J. Krueger, J. Chem. Phys. **72**, 280 (1980).

136. X.-Q. Tan and D. W. Pratt, J. Chem. Phys. **100**, 7061 (1994).

137. Z.-Q. Zhao, C. S. Parmenter, D. B. Moss, A. J. Bradley, A. E. W. Knight, and K. G. Owens, J. Chem. Phys. **96**, 6362 (1992).

138. M. Fujii, M. Yamauchi, K. Takazawa, and M. Ito, Spectrochim. Acta A **50**, 1421 (1994).

139. K. Okuyama, N. Mikami, and M. Ito, Laser Chem. **7**, 197 (1987).

140. H. Ikoma, K. Takazawa, Y. Emura, S. Ikeda, H. Abe, H. Hayashi, and M. asaaki Fujii, J. Chem. Phys. **105**, 10201 (1996).

141. J. L. Lin, K. C. Lin, and W. B. Tzeng, J. Phys. Chem.A **106**, 6462 (2002).

142. H. Nakai and M. Kawai, J. Chem. Phys. **113**, 2168 (2000).

143. K. T. Lu, F. Weinhold, and J. C. Weisshaar, J. Chem. Phys. **102**, 6787 (1995).

144. D. E. Powers, J. B. Hopkins, and R. E. Smalley, J. Chem. Phys. **72**, 5721 (1980).

145. R. Tembreull, T. M. Dunn, and D. M. Lubman, Spectrochim. Acta A **42**, 899 (1986).

146. W. B. Tzeng and K. Narayanan, J. Mol. Struct. **446**, 93 (1998).

147. S. Yan and L. H. Spangler, J. Chem. Phys. **96**, 4106 (1992).

148. L. Santos, E. Martínez, B. Ballesteros, and J. Sanchez, Spectrochim. Acta A **56**, 1905 (2000).

149. R. Disselkamp, H. S. Im, and E. R. Bernstein, J. Chem. Phys. **97**, 7889 (1992).

150. W. B. Tzeng, K. Narayanan, J. L. Lin, and C. C. Tung, Spectrochim. Acta Part A **55**, 153 (1999).

151. B. Ballesteros and L. Santos, Spectrochim. Acta A **58**, 1069 (2002).

152. P. M. Brodersen and R. D. Gordon, J. Mol. Struct. **522**, 279 (2000).

153. C. Jacoby, M. Bhm, C. Vu, C. Ratzer, and M. Schmitt, ChemPhysChem **7**, 448 (2006).

154. D. F. Plusquellic and D. W. Pratt, J. Chem. Phys. **97**, 8970 (1992).

155. K. Remmers, E. Jalviste, I. Mistrk, G. Berden, and W. L. Meerts, J. Chem. Phys. **108**, 8436 (1998).

156. G. Myszkiewicz, W. L. Meerts, C. Ratzer, and M. Schmitt, Phys. Chem. Chem. Phys. **7**, 2142 (2005).

157. T. M. Korter, D. R. Borst, C. J. Butler, and D. W. Pratt, J. Am. Chem. Soc. **123**, 96 (2001).

158. D. R. Borst and D. W. Pratt, J. Chem. Phys. **113**, 3658 (2000).

159. M. Böhm, C. Ratzer, and M. Schmitt, J. Mol. Struc. **800**, 55 (2005).

160. M. Schmitt, C. Ratzer, C. Jacoby, and W. L. Meerts, J. Mol. Struc. **742**, 123 (2005).

161. J. W. Ribblett, D. R. Borst, and D. W. Pratt, J. Chem. Phys. **111**, 8454 (1999).

162. Y. Svartsov and M. Schmitt, J. Chem. Phys. **128**, 214310 (2008).

163. K. Fuke, H. Yoshiuchi, K. Kaya, Y. Achiba, K. Sato, and K. Kimura, J. Phys. Chem. **88**, 5840 (1984).

164. S. K. Kim and E. R. Bernstein, J. Phys. Chem **94**, 3531 (1990).

165. A. Nakajima, M. Hirano, R. Hasumi, K. Kaya, H. Watanabe, C. C. Carter, J. Williamson, and T. A. Miller, J. Phys. Chem.A **101**, 392 (1999).

166. D. E. Folmer, E. S. Wisniewski, J. R. Stairs, and J. A. W. Castleman, J. Phys. Chem.A **104**, 10545 (2000).

167. H. Yokoyama, H. Watanbe, T. Omi, S. Ishiuchi, and M. Fujii, J. Phys. Chem.A **105**, 9366 (2001).

168. R. Brause, D. Krügler, M. Schmitt, K. Kleinermanns, A. Nakajima, and T. A. Miller, J. Chem. Phys. **123**, 224311 (2005).

169. A. Hara, K. Sakota, M. Nakagaki, and H. Sekiya, Chem. Phys. Lett. **407**, 30 (2005).

170. M. Schmitt, C. Ratzer, K. Kleinermanns, and W. L. Meerts, Mol. Phys. **102**, 1605 (2004).

171. C. Kang, J. T. Yi, and D. W. Pratt, J. Chem. Phys. **123**, 094306 (2005).

172. R. Brause, M. Schmitt, D. Spangenberg, and K. Kleinermanns, Mol. Phys. **102**, 1615 (2004).

173. C. Kang, J. T. Yi, and D. W. Pratt, Chem. Phys. Lett. **423**, 7 (2006).

174. J. Catalán and J. L. G. de Paz, J. Chem. Phys. **122**, 244320 (2005).

175. J. Catalán, P. Pérez, J. C. del Valle, J. L. G. de Paz, and M. Kasha, Proc. Natl. Acad. Sci. USA **99**, 5799 (2002).

176. Y. Huang, S. Arnold, and M. Sulkes, J. Phys. Chem. **100**, 4734 (1996).

177. J. D. Lewis, T. B. Malloy, Jr., T. H. Chao, and J. Laane, J. Mol. Struct. **12**, 427 (1972).

178. C. Jacoby and M. Schmitt, Chem. Phys. Chem. **5**, 1686 (2004).

179. G. Granucci, J. Hynes, P. Millié, and T.-H. Tran-Thi, J. Am. Chem. Soc. **122**, 12243 (2000).

180. H. Abe, N. Mikami, and M. Ito, J. Phys. Chem. **86**, 1768 (1982).

181. A. Sur and P. M. Johnson, J. Chem. Phys. **84**, 1206 (1986).

182. R. J. Stanley and A. W. Castleman, Jr., J. Chem. Phys. **94**, 7744 (1991).

183. M. Schütz, T. Bürgi, S. Leutwyler, and T. Fischer, J. Chem. Phys. **98**, 3763 (1993).

184. M. Gerhards, M. Schmitt, K. Kleinermanns, and W. Stahl, J. Chem. Phys. **104**, 967 (1996).

185. M. Schmitt, C. Jacoby, and K. Kleinermanns, J. Chem. Phys. **108**, 4486 (1998).

186. R. M. Helm, H. P. Vogel, and H. J. Neusser, J. Chem. Phys. **108**, 4496 (1998).

187. T. Ebata, M. Furukawa, T. Suzuki, and M. Ito, J. Opt. Soc. Am. B **7**, 1890 (1990).

188. O. Dopfer, G. Reiser, K. Müller-Dethlefs, E. W. Schlag, and S. D. Colson, J. Chem. Phys. **101**, 974 (1994).

189. T. Watanabe, T. Ebata, S. Tanabe, and N. Mikami, J. Chem. Phys. **105**, 408 (1996).

190. S. Tanabe, T. Ebata, M. Fujii, and N. Mikami, Chem. Phys. Lett. **215**, 347 (1993).

191. A. Courty, M. Mons, B. Dimicoli, F. Piuzzi, V. Brenner, and P. Millié, J. Phys. Chem.A **102**, 4890 (1998).

192. A. Westphal, C. Jacoby, C. Ratzer, A. Reichelt, and M. Schmitt, Phys. Chem. Chem. Phys. **5**, 4114 (2003).

193. D. M. Chapman, K. Müller-Dethlefs, and J. B. Peel, J. Chem. Phys. **111**, 1955 (1999).

194. J. A. Syage and J. Steadman, J. Chem. Phys. **95**, 2497 (1991).

195. M. F. Hineman, D. F. Kelley, and E. R. Bernstein, J. Chem. Phys. **99**, 4533 (1993).

196. G. A. Pino, G. Grégoire, C. Dedonder-Lardeux, C. Jouvet, S. Martrenchard, and D. Solgadi, Phys. Chem. Chem. Phys. **2**, 893 (2000).

197. G. Grégoire, C. Dedonder-Lardeux, C. Jouvet, S. Martrenchard, A. Peremans, and D. Solgadi, J. Phys. Chem.A **104**, 9087 (2000).

198. G. Grégoire, C. Dedonder-Lardeux, C. Jouvet, S. Martrenchard, and D. Solgadi, J. Phys. Chem.A **105**, 5971 (2001).

199. M. Schmitt, C. Jacoby, M. Gerhards, C. Unterberg, W. Roth, and K. Kleinermanns, J. Chem. Phys. **113**, 2995 (2000).

200. H. T. Kim, R. J. Green, J. Qian, and S. L. Anderson, J. Chem. Phys. **112**, 5717 (2000).

201. S. Ishiuchi, M. Saeki, M. Sakai, and M. Fujii, Chem. Phys. Lett. **322**, 27 (2000).

202. S. Ishiuchi, K. Daigoku, M. Saeki, M. Sakai, K. Hashimoto, and M. Fujii, J. Chem. Phys. **117**, 7077 (2002).

203. S. Ishiuchi, K. Daigoku, M. Saeki, M. Sakai, K. Hashimoto, and M. Fujii, J. Chem. Phys. **117**, 7083 (2002).

204. S. R. Haines, C. E. H. Dessent, and K. Müller-Dethlefs, J. Chem. Phys. **111**, 1947 (1999).

205. S. Ullrich, G. Tarczay, and K. Müller-Dethlefs, J. Phys. Chem.A **106**, 1496 (2002).

206. B. B. Champagne, J. F. Pfanstiel, D. W. Pratt, and R. C. Ulsh, J. Chem. Phys. **102**, 6432 (1991).

207. K. Fuke and K. Kaya, Chem. Phys. Lett. **91**, 311 (1982).

208. K. Fuke and K. Kaya, Chem. Phys. Lett. **94**, 97 (1983).

209. O. Dopfer, G. Lembach, T. G. Wright, and K. Müller-Dethlefs, J. Chem. Phys. **98**, 1933 (1993).

210. M. Schmitt, U. Henrichs, H. Müller, and K. Kleinermanns, J. Chem. Phys. **103**, 9918 (1995).

211. P. M. Felker, J. Phys. Chem. **96**, 7844 (1992).

212. A. Weichert, C. Riehn, and B. Brutschy, J. Phys. Chem.A **105**, 5679 (2001).

213. P. Hobza, C. Riehn, A. Weichert, and B. Brutschy, Chem. Phys. **283**, 331 (2002).

214. T. Ebata, T. Watanabe, and N. Mikami, J. Phys. Chem. **99**, 5761 (1995).

215. T. Ebata, M. Kayano, S. Sato, and N. Mikami, J. Phys. Chem.A **105**, 8623 (2001).

216. N. W. Larsen, J. Mol. Struct. **51**, 175 (1979).

217. J. Christoffersen, J. M. Hollas, and G. H. Kirby, Proc. Roy. Soc. A. **307**, 97 (1968).

218. D. Levine, *PGAPack V1.0, PgaPack can be obtained via anonymous ftp from: ftp://ftp.mcs.anl.gov/pub/pgapack/pgapack.tar.z* (1996).

219. H. C. Allen and P. C. Cross, *Molecular Vib-Rotors* (Wiley, New York, 1963).

220. T. Pedersen, N. W. Larsen, and L. Nygaard, J. Mol. Struct. **4**, 59 (1969).

221. H. Forest and B. P. Dailey, J. Chem. Phys. **45**, 1736 (1966).

222. D. Krügler and M. Schmitt, unpublished results.

223. J. K. G. Watson, A. Roytburg, and W. Ulrich, J. Mol. Spec. **196**, 102 (1999).

224. C. Costain, J. Chem. Phys. **29**, 864 (1958).

225. H. D. Rudolph, Struc. Chem. **2**, 581 (1991).

226. C. Jacoby, W. Roth, and M. Schmitt, Appl. Phys. B **71**, 643 (2000).

227. E. Jalviste and A. Treshchalov, Chem. Phys. **172**, 325 (1993).

228. B. Velino, A. Trombetti, and E. Cané, J. Mol. Spec. **152**, 434 (1992).

229. E. Cané, A. Trombetti, B. Velino, and W. Caminati, J. Mol. Spec. **150**, 222 (1991).

230. G. Berden, W. L. Meerts, and E. Jalviste, J. Chem. Phys. **103**, 9596 (1995).

231. A. C. Borin and L. Serrano-Andrés, Chem. Phys. **262**, 253 (2000).

232. L. Serrano-Andrés and A. C. Borin, Chem. Phys. **262**, 267 (2000).

233. I. Maki, K. Nishimoto, M.-A. Sugiyama, H. Hiratsuka, and Y.Tanizaki, Bull. Chem. Soc. Jpn **54**, 8 (1981).

234. R. D. Suenram, F. J. Lovas, and G. T. Fraser, J. Mol. Spec. **127**, 472 (1988).

235. W. Caminati and S. di Bernardo, J. Mol. Struct. **240**, 253 (1990).

236. M. J. Frisch, G. W. Trucks, H. B. Schlegel, G. E. Scuseria, M. A. Robb, J. R. Cheeseman, V. G. Zakrzewski, J. A. Montgomery, Jr., R. E. Stratmann,, *Gaussian 98, revision a.11*, Gaussian, Inc., Pittsburgh, PA (2001).

237. K. Andersson, M. Barysz, A. Bernhardsson, M. R. A. Blomberg, D. L. Cooper, M. P. Fülscher, C. de Graaf, B. A. Hess, G. Karlström, R. Lindh,, *Molcas Version 5.4*, Lund University, Sweden (2002).

238. R. Bauernschmitt and R. Ahlrichs, Chem. Phys. Lett. **256**, 454 (1996).

239. R. Bauernschmitt, M. Häser, O. Treutler, and R. Ahlrichs, Chem. Phys. Lett. **264**, 573 (1997).

240. A. D. Becke, J. Chem. Phys. **98**, 5648 (1993).

241. J. T. H. Dunning, J. Chem. Phys. **90**, 1007 (1989).

242. R. Ahlrichs, M. Bär, and H.-P. Baron, *Turbomole (version 5.7)*, Universität Karlsruhe,

Germany (2002).

243. R. M. Lees, J. Mol. Spec. **33**, 124 (1970).

244. W. C. Hamilton, *Statistics in Physical Science* (Ronald Press, New York, 1964).

245. S. Brandt, *Data Analysis* (Springer Verlag, Berlin, 1998), 3rd ed., ISBN 0387984984.

246. Z. Q. Li and H. A. Scheraga, Proc. National Academy of Science **84**, 6611 (1987).

247. D. J. Wales and J. P. K. Doye, J. Phys. Chem.A **101**, 5111 (1997).

248. D. M. Deaven and K. M. Ho, Phys. Rev. Lett. **75**, 288 (1995).

249. S. K. Gregurick, M. H. Alexander, and B. Hartke, J. Chem. Phys. **104**, 2684 (1996).

250. J. A. Niesse and H. R. Mayne, J. Chem. Phys. **105**, 4700 (1996).

251. D. M. Deaven, N. Tit, J. R. Morris, and K. M. Ho, Chem. Phys. Lett. **256**, 155 (1996).

Summary

Despite the fact that the field of molecular spectroscopy is mature, it is still very much alive. Advances in equipment and techniques allow ever more precise measurements of molecular parameters to be made, and an increasing amount of systems that were previously out of reach can now be investigated. Simultaneously, improvements in theoretical models and increases in computational power permit ever more elaborate calculations to be performed. It is in the interplay between theory and experiment, where the results of the one are compared with the other, that molecular spectroscopy finds its application. In this thesis, high-resolution UV spectroscopy is used to determine the rotational constants of smaller biomolecular systems (between 15 and 30 atoms in size) in both their ground (S_0) and first electronically excited (S_1) states. These rotational constants define a system's rotational speed around each of its main inertial axes and therefore depend on the molecular geometry. Although a complete structure determination is highly impractical, if not impossible, for all but the smallest systems, detailed information can generally be derived on the interactions that define a system's geometry. Apart from this, dynamical processes such as internal rotation and proton tunneling may give rise to measurable splittings, which can therefore also be investigated.

The research described in this thesis is fundamental in nature. Its main goal is to better understand the interactions which determine the structure and functionality in large biological systems such as proteins and DNA. All of the systems that are described here are therefore models of some specific type of interaction or functional group relevant to these larger systems.

Chapter 2 describes the benzoic acid dimer, where both monomer units are connected by two hydrogen bonds. Multiple hydrogen bonds occur in both proteins, where they are responsible for the formation of structural elements such as α-helices and β-sheets, and in DNA, where they tie together the two strands it consists of. Despite this, a quantitative description of bond strengths and dynamics in multiply hydrogen-bonded systems still poses a real challenge to theory, and relatively little experimental information is available. Benzoic acid easily forms dimers, which possess a high fluorescence quantum yield and adopt a highly symmetric ground state structure. These properties make it ideally suited for high-resolution UV spectroscopic investigation. It is found that a concerted tunneling motion is possible, where both

123

hydrogen atoms involved in hydrogen bonding are simultaneously exchanged between both moieties. On electronic excitation this motion is suppressed, and the corresponding barrier height is found to increase by approximately 7.2 % in the S_1 state. The excitation itself is shown to reside on one half of the complex, and within the resolution of the experiment excitation transfer to the other half is not found to occur. This localization of electronic excitation introduces an asymmetry in the hydrogen bonding network, which results in a lowering of the C_{2h} ground state symmetry to C_s. Simultaneously, the hydrogen bonds are weakened in the S_1 state.

The competition between two different types of intermolecular force is investigated in chapter 3. Part of the biological selectivity which is important for the proper functioning of many biomolecular systems is achieved by the prevalence of a certain bond type over another. It is therefore interesting to investigate the preferential binding motifs in a system where two different types of interaction are possible which are comparable in magnitude. One such system is the complex of phenol with argon atoms, where the latter can bind to the phenol molecule through either hydrogen bonding or van der Waals bonding. Apart from being one of the easiest systems to offer this choice, phenol is also a fragment of several important biomolecules such as the amino acid tyrosine. It turns out that in complexes with one or two argon atoms van der Waals bonding is preferred, with the two argon complex adopting a symmetric structure where one argon atom is located on each side of the phenol ring. Furthermore, it is found that the distance between the ring and each argon atom is slightly larger in the two argon cluster due to a smaller inductive force and that the excited state lifetime decreases on cluster building.

Steric hindrance between different sidegroups in an amino acid chain is a very important factor for protein folding. Since dynamical processes in sidegroups are very sensitive to the local electronic environment, investigation of molecules which contain several flexible groups in neighbouring positions can provide detailed information on the (electronic) structure in sterically hindered systems. *O*-toluidine (also known as *o*-methylaniline), which is discussed in chapter 4, is such a molecule. It consists of a benzene ring with an amino group (which can perform an inversion motion) and a methyl group (which can rotate around its C_3 symmetry axis) as substituents. The barrier to internal rotation of the methyl group is found to be much lower in the S_1 state than in the ground state and to be mainly electronic in nature. Simultaneously, the benzene ring geometry becomes distorted on electronic excitation, which dramatically increases the steric hindrance between both substituents and leads to a precessional motion of the whole methyl group. The equilibrium orientation of the methyl group is also rotated with respect to the ground state, and the angle of the amino group with the benzene plane becomes smaller.

Tautomeric processes in DNA base pairs, which interconvert two closely connected chemical structures, are often modeled by the 7-azaindole dimer. In order to gain more insight into its hydrogen bonding characteristics, chapter 5 discusses the complexes of 7-azaindole with one and two water molecules. In these complexes the water molecules bridge the two hydrogen bonding sites of 7-azaindole, forming cyclic structures. Whereas the one water complex is planar, both water oxygen atoms as well as two of their hydrogen atoms are located outside the monomer plane in the two water complex. The out-of-plane hydrogen atoms have the possibility of tunneling through the 7-azaindole plane simultaneously, changing from an equilibrium up-down geom-

etry to down-up and vice versa. Furthermore, the energy level ordering of the first two electronically excited states is reversed with respect to the monomer on cluster building while the S_1 state lifetime is increased by a factor of four.

Chapter 6 returns to the phenol molecule, this time to investigate the sensitive equilibrium between dispersion and attraction due to hydrogen bonding in its dimer. The structures of larger biomolecules often depend very sensitively on such a balance of forces, and the phenol dimer provides an excellent way to determine their relative strengths. The reason for this is that the planes of both moieties are at an angle with respect to each other, and the size of this angle is indicative of the strength of the dispersion interaction. The angle is found to be smaller in the ground state than in the electronically excited state, from which a decrease in dispersion interaction on electronic excitation can be deduced. Simultaneously, the hydrogen bond connecting both moieties is shortened, indicating an increase in bond strength.

The last chapter describes measurements on the indole analogue benzimidazole. Since indole is the chromophore of the amino acid tryptophan and accounts for most of the fluorescence in proteins, a knowledge of its excited state properties and those of its analogues is important for the interpretation of protein fluorescence data. It is shown that electronic excitation leads to an increase in bond lengths in one half of the molecule whereas an overall decrease in bond lengths is found for the other half. Furthermore, the direction in which electron density is shifted on excitation is quantified and compared with the results of various computational methods. The degree of correspondence is poor, and the data in this chapter are therefore an important addition to the understanding of electronic excitation in this system.

Summarizing the research in this thesis it is clear that quantum chemical calculations are ever more capable of correctly predicting structures of small biomolecular systems. Although at this point in time experimental data are still more accurate than the most elaborate calculations that are possible today, that situation may well change in the coming years. The real challenge, therefore, is in the prediction of other properties, such as transition dipole moment direction and dynamics. Especially the prediction of dynamics in weakly bound clusters, as investigated in many of the systems described here, is computationally tough. Enabled by technological advances it is this topic that will most likely be of greatest interest for future experiments.

Samenvatting

Ondanks het feit dat moleculaire spectroscopie een gerijpt vakgebied is, is het nog altijd zeer levendig. Ontwikkelingen aan apparatuur en technieken maken het mogelijk om moleculaire parameters steeds preciezer te bepalen, en een groeiend aantal systemen dat voorheen buiten bereik was kan nu onderzocht worden. Tegelijkertijd stellen verbetering van theoretische modellen en toename van rekenkracht ons in staat om steeds uitgebreidere berekeningen uit te voeren. In de interactie tussen theorie en experiment, waar de resultaten van de een vergeleken worden met de ander, vindt de moleculaire spectroscopie zijn toepassing. In dit proefschrift wordt hoge resolutie UV spectroscopie gebruikt om de rotatieconstanten van kleinere biomoleculaire systemen (typisch 15 tot 30 atomen groot) in hun grondtoestand (S_0) en eerste elektronisch aangeslagen toestand (S_1) te bepalen. Deze rotatieconstanten beschrijven de rotatiesnelheid van een systeem rond elk van zijn hoofd inertiaalassen en hangen daarom af van de moleculaire geometrie. Alhoewel een volledige bepaling van de structuur zeer onpraktisch zo niet onmogelijk is voor alle behalve de allerkleinste systemen, kan in het algemeen gedetailleerde informatie verkregen worden over de interacties die de geometrie van een systeem bepalen. Verder kunnen dynamische processen zoals interne rotatie en proton tunneling resulteren in meetbare spectrale opslitsingen, die daarom ook onderzocht kunnen worden.

Het onderzoek dat beschreven is in dit proefschrift is fundamenteel van aard. Hoofddoel is een beter begrip van de interacties die de structuur en functionaliteit bepalen in grote biologische systemen zoals eiwitten en DNA. Alle systemen die beschreven zijn in dit proefschrift zijn daarom modelsystemen voor een specifieke interactie of functionele groep die relevant is voor deze grotere systemen.

Hoofdstuk 2 beschrijft het benzoëzuur dimeer, waar beide monomerische helften met elkaar verbonden zijn door middel van twee waterstofbruggen. Meervoudige waterstofbruggen komen voor in zowel eiwitten, waar ze verantwoordelijk zijn voor de vorming van structuurelementen zoals α-helices en β-sheets, als in DNA, waar ze de beide strengen waaruit het is opgebouwd met elkaar verbinden. Desondanks vormt de beschrijving van bindingssterktes en dynamica in meervoudig waterstofgebonden systemen een grote uitdaging voor theoretische modellen, en is relatief weinig experimentele informatie beschikbaar. Benzoëzuur vormt gemakkelijk dimeren, die een hoge fluorescentie-opbrengst hebben en in de grondtoestand een hoogsymmetrische struc-

tuur aannemen. Deze eigenschapppen maken het bij uitstek geschikt voor onderzoek met behulp van hoge resolutie UV spectroscopie. Het blijkt dat een gecoördineerde tunnelingsbeweging mogelijk is waarbij beide waterstofatomen die betrokken zijn bij waterstofbinding gelijktijdig uitgewisseld worden tussen beide moieteiten. Bij elektronische excitatie wordt deze beweging onderdrukt en neemt de hoogte van de corresponderende potentiaalbarrière toe met ongeveer 7.2 % in de S_1 toestand. Aangetoond wordt dat de excitatie zelf gelocaliseerd is op een helft van het complex, en dat binnen de resolutie van het experiment overdracht van deze excitatie op de andere helft niet plaatsvindt. Deze localisatie van elektronische excitatie introduceert een asymmetrie in het netwerk van waterstofbruggen, wat resulteert in een verlaging van de C_{2h} symmetrie van de grondtoestand tot C_s. Tegelijkertijd worden de waterstofbruggen verzwakt in de S_1 toestand.

De competitie tussen twee verschillende types van intermoleculaire krachten is onderzocht in hoofdstuk 3. Een deel van de biologische selectiviteit die belangrijk is voor het goed functioneren van veel biomoleculaire systemen wordt bereikt doordat een bepaald bindingstype gemakkelijker gevormd wordt dan andere. Om die reden is het interessant om het geprefereerde bindingstype te onderzoeken in een systeem waarin twee soorten interacties van vergelijkbare sterkte mogelijk zijn. Een voorbeeld van zo'n systeem is het complex van fenol met argon atomen, waar laatstgenoemden zich aan het fenolmolecuul kunnen binden door middel van een waterstofbrug of een van der Waals binding. Buiten het feit dat fenol één van de eenvoudigste systemen is dat deze keuze biedt is het ook een fragment van een aantal belangrijke biomoleculen, zoals het aminozuur tyrosine. In complexen met één of twee argonatomen heeft van der Waals binding de voorkeur, waarbij het twee argon complex een symmetrische structuur aanneemt met één argonatoom aan elk van beide kanten van de fenolring. Verder wordt bepaald dat de afstand tussen de ring en elk van de argonatomen vanwege een kleinere inductieve kracht groter is in de twee argon cluster en dat de levensduur van de elektronisch aangeslagen toestand daalt bij clusterformatie.

Sterische hindering tussen de verschillende zijgroepen in een keten van aminozuren is een zeer belangrijke factor voor de manier waarop eiwitten zich vouwen. Aangezien dynamische processen in zijgroepen erg gevoelig zijn voor de lokale elektronische omgeving kan onderzoek aan moleculen die meerdere flexibele groepen in naburige posities bevatten gedetailleerde informatie opleveren over de (elektronische) structuur in sterisch gehinderde systemen. *O*-toluidine (ook bekend onder de naam *o*-methylaniline), dat bediscussieerd wordt in hoofdstuk 4, is zo'n molecuul. Het bestaat uit een benzeenring met een aminogroep (die een inversiebeweging kan uitvoeren) en een methylgroep (die kan roteren om zijn C_3 symmetrieas) als substituties. De barrière voor interne rotatie van de methylgroep blijkt in de S_1 toestand veel lager dan in de grondtoestand en voornamelijk elektronisch van aard te zijn. Tegelijkertijd raakt de geometrie van de benzeenring vervormd bij elektronische excitatie, wat de sterische hindering tussen beide gesubstitueerde groepen dramatisch verhoogt en leidt tot een precessiebeweging van de hele methylgroep. De evenwichtsoriëntatie van de methylgroep is ook geroteerd ten opzichte van de grondtoestand, en de hoek die de aminogroep maakt met het vlak van de benzeenring is kleiner.

Tautomerische processen in DNA baseparen, die twee nauw verwante chemische structuren in elkaar over doen gaan, worden vaak gemodelleerd door het 7-azaindool dimeer. Om meer inzicht te krijgen in de karakteristieken van de waterstofbruggen

in dit systeem bespreekt hoofdstuk 5 de complexen van 7-azaindool met één en twee watermoleculen. In deze complexen verbinden de watermoleculen de twee posities met elkaar waar 7-azaindool waterstofbruggen kan vormen, waarbij cyclische structuren ontstaan. Waar het één water complex vlak is liggen in het twee water complex zowel beide zuurstofatomen als twee van de waterstofatomen van de watermoleculen buiten het monomeervlak. De waterstofatomen die buiten dit vlak liggen kunnen er gelijktijdig doorheen tunnelen, zodat de geometrie van een boven-beneden in een beneden-boven structuur overgaat, en vice versa. Verder wordt bij clusterformatie de ligging van de eerste twee elektronisch aangeslagen toestanden omgedraaid ten opzichte van het monomeer, terwijl de levensduur van de S_1 toestand met een factor vier toeneemt.

In hoofdstuk 6 wordt teruggekomen op het fenol molecuul, deze keer om in het dimeer het gevoelige evenwicht tussen dispersie en aantrekking ten gevolge van waterstofbinding te onderzoeken. Net als in dit geval hangen de structuren van grotere biomoleculen vaak af van een precieze balans van krachten, en het fenol dimeer is een uitstekende manier om de relatieve sterktes van deze krachten te bepalen. De reden hiervoor is dat de vlakken van beide moieteiten ten opzichte van elkaar een hoek maken, waarvan de grootte een indicatie is voor de sterkte van de dispersie-interactie. De hoek blijkt in de grondtoestand kleiner te zijn dan in de elektronisch aangeslagen toestand, waaruit een vermindering van de dispersie-interactie bij elektronische excitatie afgeleid kan worden. Tegelijkertijd wordt de waterstofbinding tussen beide moieteiten korter, wat duidt op een toename in de sterkte van deze binding.

Het laatste hoofdstuk beschrijft metingen aan de indool analoog benzimidazole. Omdat indool het chromofoor is van het aminozuur tryptofaan en als zodanig verantwoordelijk is voor het grootste deel van de fluorescentie in eiwitten, is kennis van de eigenschappen van zijn aangeslagen toestand en die van zijn analogen belangrijk voor de interpretatie van fluorescentiemetingen aan eiwitten. Aangetoond wordt dat elektronische excitatie leidt tot een toename van bindingslengtes in een helft van het molecuul terwijl een globale afname gevonden wordt voor de andere helft. Ook wordt de richting bepaald waarin elektronendichtheid binnen het molecuul verschuift als gevolg van excitatie en wordt deze vergeleken met de resultaten van meerdere computationele methodes. De overeenkomst is mager, en de gegevens in dit hoofdstuk vormen daarom een belangrijke toevoeging aan het begrip van elektronische excitatie in dit systeem.

Wanneer het onderzoek in dit proefschrift opgesomd wordt is het duidelijk dat kwantum chemische berekeningen steeds beter in staat zijn om de structuren van kleine biomoleculaire systemen te voorspellen. Alhoewel experimentele data op dit moment nog nauwkeuriger zijn dan de meest uigebreide berekeningen die vandaag de dag mogelijk zijn, is het zeer goed mogelijk dat dit in de komende jaren verandert. De echte uitdaging ligt daarom in het voorspellen van andere eigenschappen, zoals de oriëntatie van het transitie dipool moment en dynamica. Met name het voorspellen van dynamica in zwak gebonden clusters, zoals onderzocht voor veel van de hier beschreven systemen, is computationeel moeilijk. Omdat technologische vooruitgang het mogelijk heeft gemaakt dit onderwerp te onderzoeken is het zeer waarschijnlijk dat dit gebied het meest interessant is voor toekomstige experimenten.

Curriculum Vitae

Name: Ivo Michel Kalkman
Born: September 3rd, 1979, Tiel, the Netherlands
Nationality: Dutch

2004-2008   PhD student at the Department of Molecular and Biophysics, Radboud University Nijmegen.
Project title: *Structure and dynamics in small biomolecular systems*, supervised by prof. dr. W. L. Meerts and prof. dr. W. J. van der Zande
Included a 1 year 8 month stay in Düsseldorf, Germany, under the supervision of Dr. M. Schmitt

1997-2002   Master in Theoretical Physics, Radboud University Nijmegen
Diploma work at the Department of Astrophysics, titled: *The Role of Chaotic Free Electron Laser Action in the Generation of Radio Pulsar Radiation*, supervised by prof. dr. J. Kuijpers

1991-1997   VWO (secondary education), Collegium Marianum Venlo
Graduation courses: Biology, Chemistry, Dutch, English, Latin, Macro-Economics, Mathematics (A and B) and Physics

Publications

M. Schmitt, M. Böhm, C. Ratzer, C. Vu, I. Kalkman and W. L. Meerts
Structural selection by microsolvation: conformational locking of tryptamine
Journal of the American Chemical Society, 127 (29), 10356 (2005)

M. Schmitt, M. Böhm, C. Ratzer, D. Krügler, K. Kleinermanns, I. Kalkman, G. Berden and W. L. Meerts
Electronic excitation in the phenol dimer: The intermolecular structure in the S_0 and S_1 state determined by rotationally resolved electronic spectroscopy
ChemPhysChem, 7 (6), 1241 (2006)

M. Schmitt, D. Krügler, M. Böhm, C. Ratzer, V. Bednarska, I. Kalkman and W. L. Meerts
A genetic algorithm based determination of the ground and excited ^1L_b state structure and the orientation of the transition dipole moment of benzimidazole
PCCP, 8 (2), 228 (2006)

C. Vu, I. Kalkman, W. L. Meerts, Y. N. Svartsov, C. Jacoby and M. Schmitt
Rotationally resolved electronic spectroscopy of water clusters of 7-azaindole
Journal of Chemical Physics, 128 (21), 214311 (2008)

I. Kalkman, C. Vu, M. Schmitt and W. L. Meerts
Tunneling splittings in the S_0 and S_1 states of the benzoic acid dimer determined by high-resolution UV spectroscopy
ChemPhysChem, 9 (12), 1788 (2008)

I. Kalkman, C. Vu, M. Schmitt and W. L. Meerts
Structure and internal rotation in the S_0 and S_1 states of o-toluidine studied by high resolution UV spectroscopy
(Submitted for publication in PCCP)

C. Vu, I. Kalkman, W. L. Meerts, C. Brand, Y. N. Svartsov, S. Wiedemann, R. Weinkauf and M. Schmitt
The conformational landscape of 5-methoxytryptamine studied by rotationally resolved fluorescence spectroscopy and resonant ionization spectroscopy
(Submitted for publication in PCCP)

I. Kalkman, C. Brand, C. Vu, W. L. Meerts, Y. N. Svartsov, O. Dopfer, K. Müller-Dethlefs, S. Grimme and M. Schmitt
The structure of phenol-Ar_n ($n = 1, 2$) clusters in their S_0 and S_1 states
(In preparation, chapter 3)

C. Vu, I. Kalkman, M. Schmitt and W. L. Meerts
Structure of the cyanophenols determined by high resolution UV spectroscopy
(In preparation)

Dankwoord

Na vier jaar lang zwoegen en de nodige tegenslag ligt hier dan toch echt mijn proefschrift. Uiteraard is dat niet alleen mijn verdienste en ben ik vele mensen in mijn omgeving hiervoor dank verschuldigd.

Allereerst wil ik hier mijn promotor, Leo Meerts, bedanken voor de moed om mij als theoretisch natuurkundige het vertrouwen te geven en in een laserlab los te laten. Met je kenmerkende geduld heb je mij door de jaren heen om weten te scholen tot experimentalist, en heb je mij de fijne kneepjes van het vak bijgebracht. Je hartelijkheid leidde bovendien tot een uitermate aangename sfeer, wat ervoor gezorgd heeft dat ik met plezier terug kan kijken op mijn promotietijd. Mijn tweede promotor, Wim van der Zande, wil ik graag bedanken voor zijn eerlijkheid en directheid. Door dingen bij de naam te noemen, ook als de boodschap minder positief was, heb jij me aangespoord om het beste in mezelf naar boven te halen. Gecombineerd met je besmettelijke liefde voor het vak en je aanhoudende interesse en betrokkenheid heb je van mij niet alleen een betere natuurkundige maar ook een evenwichtiger persoon gemaakt.

Geen van de experimenten die ik voor dit proefschrift gedaan heb zou mogelijk zijn geweest zonder uitgebreide ondersteuning. André, Cor, Danny en Leander, dankzij jullie technische expertise is mijn praktische kennis van vacuümapparatuur en mechanica enorm gegroeid en zijn vele problemen opgelost. Peter, ook jouw kennis van electronica heeft mij meer dan eens uit de brand geholpen. Voor het brengen van orde in de chaos die promotie heet kon ik verder altijd terugvallen op onze secretaresses: Erna, Ine en Magda.

De overige collega's op de afdeling wil ik graag bedanken voor de collegialiteit en vriendelijkheid. Afric, jij bent tijdens mijn hele promotie de enige andere promovendus geweest binnen onze groep, en als zodanig de eerste persoon bij wie ik mijn frustratie kwam uiten als er weer eens iets kapot was. Met jouw relativeringsvermogen en kalmte wist je me er echter altijd snel van te overtuigen dat het allemaal zo erg niet was, en heb je me zodoende menige slapeloze nacht bespaard. Dennis, naast een gezellige collega was jij ook kritisch: je stond altijd open voor discussies en had altijd goede ideeën. Die eigenschappen zullen ongetwijfeld van pas komen in je promotie, waar ik je veel succes mee wens. Ook alle andere collegas binnen de groep hebben ieder hun eigen steentje bijgedragen aan een mooie tijd. Daarvoor wil ik Aleksandra, Angelica, Anthony, Arjan, Bas, Chung Hsin, Dave, Dmitri, Dragana, Elena, Frans, Gautam, Gowri, Hans, Heqing, Iulia, Ivan, James, Jeroen, Kasper, Konstantin, Lionel,

Malcom, Marcela, Marco, Marius, Masha, Mehrnoosh, Mira, Nico, Reyer, Rienk, Robert, Sacco, Simona, Stefan, Thijs, Yongwei, Zahid en Zhichao en alle studenten en gasten hartelijk bedanken.

Auch den Mitarbeitern in Düsseldorf möchte ich an dieser Stelle herzlich danken. Zuerst Michael Schmitt, meinem Kodoktorvater, für die freundliche Betreuung während meines Aufenthaltes in Düsseldorf. Dein Enthusiasmus und Eifer waren inspirierend und du hattest immer ein offenes Ohr für meine ab und zu ungewöhnliche Ideen. Ohne deine Hilfe wäre das Schreiben dieser Doktorarbeit sicherlich unmöglich gewesen. Karl Kleinermanns möchte ich herzlich für seine Gastfreundschaft danken. Chau, Christian, Marcel und Yuriy: Nicht nur war unsere Zusammenarbeit im Labor sehr erfolgreich, auch habt ihr mit euren verständlichen Erklärungen meine Kenntnis in der Chemie wesentlich verbessert. Außerdem waren die Tassen Tee und die sozialen Tätigkeiten sehr erfrischend. Ich freue mich euch als Kollegen gehabt zu haben. Arno, dein Sachverstand und deine Fähigkeiten mit den verschiedenen Apparaturen waren unglaublich hilfreich, und auch das Bier und das Schlittschuhfahren werde ich nie vergessen. Die Assistenz, die von Dieter, Klaus, Frau Jauch, Frau Köhler, Frau Müller und Frau Schiedel geboten wurde, war ebenfalls unentbehrlich. Zu guter letzt war die Atmosphäre in die Arbeitsgruppe stets gemütlich. Andreas, Daniel, Dennis, Gernot, Kai, Katharina, Ke Feng, Kristina, Lars, Matthias, Michael, Peter, Robert, Swen, Thomas und Thorsten: danke dafür.

Uiteraard mag ik niet vergeten de vrienden te bedanken waarop ik altijd terug kan vallen. Albert en Femke voor jullie vriendschap en de klimtrips (waarvan de fotos nog altijd in jullie huis staan) en die altijd een welkome afwisseling waren in een leven vol wetenschap en wetenschappers. Aleid, Anne, Annika, Berber, Erik, Gijs, Hilde, Inge, Ingrid, Laurens, Linda, Maayke, Marieke, Renate, Suzanne, Taco en Wieteke voor alle mooie momenten als ik na een dag noeste arbeid weer terugkwam op de gang. Anna, thank you for your energetic and unrestrained approach to life, which made you a fantastic friend and a real pleasure to be with. Bart, Chris, George, Matthé en Kjeld bedankt voor de altijd gezellige (en lange) Irish coffee avonden. Mijn vrienden van de middelbare school met wie ik altijd contact ben blijven houden, Daan, Loek, Michael, Steven en Thomas, voor jullie vertrouwen. Hilje, Jisk, Manda, Margriet, Rob, Talita, Tim en Wieneke voor de talloze avonden in de stad en Joris voor de mooie klimvakanties. Janneke voor je hulp bij mijn pogingen om mijn dromen waar te maken. Mark voor je raad bij al mijn LATEX problemen en voor je heerlijk nuchtere levenshouding. Patty voor het feit dat je altijd tijd voor me maakt, ook als het je eigenlijk niet uitkomt. Ramona, danke für deine Gesellschaft während meiner Zeit in Düsseldorf, den Deutschunterricht und dein nie nachlassendes Interesse. Roel, bedankt voor de de tijd die we samen in de lucht doorgebracht hebben en Ton voor je eeuwige pogingen om mij over iets anders te laten praten dan natuurkunde. Yamuna tenslotte voor je mentale steun in moeilijker tijden. Ook alle mensen in de twee organisaties waar ik jarenlang nauw bij betrokken ben geweest, de NijSAC en Probe, wil ik bij deze bedanken voor hun gezelschap.

Als laatste wil ik hier graag mijn familie bedanken. Mijn broer Robert, voor het feit dat je altijd voor me klaarstaat en niets teveel gevraagd is. Karen, voor je positieve instelling en behulpzaamheid. Tenslotte mijn ouders, omdat ze altijd in mij zijn blijven geloven en mij in alles bij hebben gestaan. Jullie steun en zorg was onmisbaar.